7911143

CHANG, LIHSIUNG ARON

A TWO-DIMENSIONAL NUMERICAL SIMULATION OF THE DRY LINE ENVIRONMENT AND ITS ROLE IN THE DEVELOPMENT OF MESOSCALE CONVECTIVE SYSTEMS.

THE UNIVERSITY OF OKLAHOMA, PH.D., 1979

University Microfilms International 300 N. ZEEB ROAD, ANN ARBOR, MI 48106

THE UNIVERSITY OF OKLAHOMA

GRADUATE COLLEGE

A TWO-DIMENSIONAL NUMERICAL SIMULATION OF THE DRY LINE ENVIRONMENT AND ITS ROLE IN THE DEVELOPMENT OF MESOSCALE CONVECTIVE SYSTEMS

A DISSERTATION

SUBMITTED TO THE GRADUATE FACULTY

in partial fulfillment of the requirements for the

degree of

DOCTOR OF PHILOSOPHY

By

LIHSIUNG ARON CHANG

Norman, Oklahoma

1978

A TWO-DIMENSIONAL NUMERICAL SIMULATION OF THE DRY LINE ENVIRONMENT AND ITS ROLE IN THE DEVELOPMENT OF MESOSCALE CONVECTIVE SYSTEMS

APPROVED BY

M. Rasmussen

Edward G. Bledi

DISSERTATION COMMITTEE

ABSTRACT

A diagnostic study is carried out through a two-dimensional numerical simulation of diurnal evolution of the dry line environment. The mesoscale boundary-layer model is constructed using a stretched horizontal grid system and a terrain-following vertical coordinate. An existing up-to-date flux-gradient parameterization scheme with an inversion-rise formalism is employed to formulate the vertical eddy-mixing processes in the atmospheric boundary layer. The horizontal mixing process is also suitably parameterized to be function of the vorticity gradient.

Several proposed physical processes relevant to the diurnal movement of dry line are tested. Different forcing conditions are also diagnosed. While vertical turbulent mixing is shown to be responsible for the daytime eastward motion of the dry line in confirmation with Schaefer's (1974) study, horizontal advection and horizontal mixing account for the nocturnal return of the surface dry line. Kinematic and thermodynamic fields in the simulated dry line environment are also examined. The divergence field and vertical motion are distributed such that there exists a favorable condition for the release of potential instability and hence the possible onset of moist convection in close proximity to the dry line. Limitations of this numerical model are discussed and several suggestions for future research of dry line-affected mesoscale convective systems are also given.

ACKNOWLEDGEMENT

I am deeply indebted to Dr. Rex L. Inman for his guidance, encouragement and constant support throughout the entire period of this study. I am also very grateful to Dr. J. F. Kimpel, Dr. J. S. Fein, Dr. M. L. Rasmussen, Dr. E. F. Blick, and Dr. A. Sundararajan for their helpful criticism and suggestions. Discussions with many other faculty members and fellow graduate students were also valuable. Thanks are also due to Dr. Walter L. Chang for the use of his well-coded subroutine for the surface layer computations. I also thank Jo Ann Oberst for her expert typing of the manuscript.

Support for the first two years of this doctoral program was provided by the National Science Council, Republic of China.

Completion of this study is also due to my wife, Nancy, who made sacrifices and provided incentive; without her moral support success would not have been possible.

TABLE OF CONTENTS

LIST OF FIGURES

Figure Page

Figure		Page

Figure | Page

LIST OF SYMBOLS

c	phase speed of waves
c_x	east-west component of phase speed
c_z	vertical component of phase speed
c_p	specific heat of air at constant pressure
d	grid interval
e_s	saturated vapor pressure of water
f	Coriolis parameter $= 2\,\Omega \sin \varphi$
$\hat{f}$	$= 2\,\Omega \cos \varphi$
g	magnitude of gravitational acceleration
H	height of the physical model; heat
k	von Karman constant; vertical wave number
K_H	horizontal exchange coefficient
K_z	vertical exchange coefficient
$K_z^{(m)}$	vertical exchange coefficient for momentum
$K_z^{(\theta)}$	vertical exchange coefficient for sensible heat
$K_z^{(q)}$	vertical exchange coefficient for specific humidity
L	Monin-Obukhov length; horizontal extent of the model
L_v	latent heat of condensation for water vapor
m	slope of terrain
N	Brunt Väisälä frequency

p	pressure
p_o	reference pressure
q	specific humidity
q_s	surface specific humidity
q_*	characteristic specific humidity
R	gas constant of moist air
R_d	gas constant of dry air
R_i	gradient Richardson number
R_{i_B}	bulk Richardson number
R_v	gas constant for water vapor
S	static stability parameter; filtering parameter
T	temperature in Kelvin scale
T_c	temperature at lifting condensation level
T_d	dew-point temperature
t	time; temperature in centigrade
u	east-west component of wind
u'	perturbation east-west component of wind
u_g	east-west component of geostrophic wind
u_*	surface friction velocity
U_w	relative humidity
v	north-south component of wind
w	vertical component of wind
$\hat{w}$	vertical motion in the new coordinate
w_*	characteristic convective velocity
$\hat{z}_c$	lifting condensation level

$\hat{z}_h$ height of surface layer

$\hat{z}_i$ height of atmospheric boundary layer

z_o roughness parameter

Ω angular velocity of earth's rotation

φ latitude; dependent variable

$\varphi_{(H)}$ nondimensional profile function for potential temperature

$\varphi_{(m)}$ nondimensional profile function for velocity

π $= c_p(P/P_o)^{R/c_p}$ Exner function

θ potential temperature

θ_s surface potential temperature

θ_* characteristic potential temperature

$\hat{\zeta}$ $= \hat{z}/L$ nondimensional stability parameter

β buoyancy parameter

ω mixing ratio

ω_s saturated mixing ratio

μ horizontal wave number

ν frequency of waves

γ_d adiabatic lapse rate

γ_m pseudo-adiabatic lapse rate

λ $= d_i/d_{i-1}$ stretching parameter

A TWO-DIMENSIONAL NUMERICAL SIMULATION OF THE DRY LINE ENVIRONMENT AND ITS ROLE IN THE DEVELOPMENT OF MESOSCALE CONVECTIVE SYSTEMS

CHAPTER I

INTRODUCTION

The frequent occurrence of thunderstorms, squall lines, and tornadoes in the U.S. Central Great Plains during the spring and early summer is well known. Two of the most important mesoscale meteorological features associated with severe weather events in this area may be the low-level jet (LLJ) and the dry line. Both occur because of boundary-layer processes in this geographical region on the eastern slope of the Rockies.

The southerly low-level jet advects warm moist air from the Gulf of Mexico (maritime tropical air, mT) into the Great Plains where it meets dry hot air originating from the southwestern U.S. and Mexico (continental tropical air, cT). The cT/mT boundary is roughly in a north-south direction and approximately parallel to the terrain contours; herein it is called the dry line.* It is characterized by a sharp gradient

---

*The dry line may be referred to as the dry front, dewpoint front, or Marfa front.

in moisture (specific humidity and dew-point temperature) and some contrast in potential temperature.

To the east of the dry line, southerly winds usually prevail, while a southwesterly or westerly wind is observed to the west (Fig. 1.1). Thus, a wind-shift zone with horizontal velocity convergence is usually observed in the vicinity of the dry line. The environment is usually unstable, especially within the moist air region where considerable potential instability may exist.

Triggering of severe storms may be related to many different causes; some of the important factors are synoptic disturbances (e.g., a cyclone, front or upper trough), regional orographic features, moisture supply, and diurnal surface heating. In the south central United States, outbreaks of nocturnal thunderstorms quite often occur in association with the low-level convergence resulting from the diurnal variation of the LLJ (Means, 1952, Pitchford and London, 1962 and Wallace 1975). While the role of the LLJ in the occurrence of nocturnal severe storms has been recognized and many investigations have been conducted, relatively little emphasis has been placed on the examination of the dry line environment. Neither are the previous dry line-related studies well-documented in the literature. The frequent occurrence of thunderstorms in association with dry lines has been pointed out by Rhea (1966). Other observational dry line studies (Fujita, 1957, McGuire, 1962 and Matteson, 1969) have revealed some of the characteristic features. Schaefer (1973) conducted a detailed study and a climatological survey regarding the genesis and the motion of the dry line. Although the dry line is a synoptic-scale feature, lengthwise, the moisture gradient across the dry line may be as strong as several g kg^{-1} (in specific humidity) within a mile; and the height of the moisture step profile may be only 3000 ~ 4000 ft (McGuire, 1962). Thus, in this aspect, any dry line development could be considered as a fine-scale phenomena in the atmospheric boundary layer (ABL). Weston's study of the Indian dry line (1972), suggested a dynamic model which depicts the formation of a step profile in moisture and the transverse-circulation produced convergence near the ground and near the edge of the moist air. Because his model appeared not to be consistent with U.S. dry lines, Weston speculated that ignoring the topography caused the discrepancy.

In spite of the previous investigations of the dry line, we do not have a complete understanding of the mechanisms involved in its development and its role in the development of convective storms. Considering its close association with severe weather events, the difficulty in locating the dry line by routine observations, its fine scale, and the possibility of its association with gravity waves, further investigation is very desirable. Toward this end, in this study we propose a numerical model of the mesoscale boundary layer to study the moisture fields, wind fields, and related thermodynamic fields in the evolving dry line environment.

Although a simulative model of dry line motion was developed by Schaefer (1974), it was too crude to include a detailed, physically sound description of ABL processes relevant in the development and motion of the dry line. Several improvements and further applicable implications can be achieved in this study:

(1) The capability of the numerical model to depict boundary layer processes in the dry line environment will depend on the choice of a grid system. Schaefer's model used a coarse grid (Δx = 100 km) in the horizontal; thus, important features could be missed and the development of the dry line may have been distorted. For a better description and for economy in core storage, a stretching type coordinate system with topography will be used, such that in the dry line vicinity finer scales will be resolved and in the outer regions a coarser grid interval will be utilized. The grid system is designed so that it is suitable to predict dry line movement.

(2) The formulation of the boundary-layer processes in the dry line environment will be important. The simulation faithfully should represent physical processes. An up-to-date

flux-gradient parameterization procedure will be used to model the vertical eddy-mixing processes within the atmospheric boundary layer. Other major adjustments are noted below:

(i) It is not appropriate to consider that the mixed ABL has a constant depth. The height of the mixed layer should be allowed to vary, responding to all relevant physical processes. Thus, an inversion-rise formalism is used to predict the inhomogeneous ABL height in the dry line environment.

(ii) The evolution of the dry line may be dictated by several major physical processes. In this numerical study, horizontal advection, terrain-induced effects, horizontal mixing processes, and vertical turbulent mixing processes all will be included and tested so that their respective importance in the evolution of the dry line can be evaluated.

A detailed description of the scheme of the numerical model with suitable parameterizations for the relevant physical processes is given in Chapter II. Necessary numerical treatments in this specific mesoscale model are also given and discussed in this chapter. In Chapter III, applications of the numerical model to the study of the diurnal movement of the dry line are discussed. A further examination of the kinematic fields and thermodynamic fields in the simulated dry line environment is accomplished in Chapter IV. Concluding remarks together with some suggestions for future research regarding dry line-affected meteorological events are given in Chapter V.

CHAPTER II

MESOSCALE NUMERICAL MODEL

This study provides a two-dimensional numerical boundary layer model. Although the dry line is not necessarily a straight line feature and may appear in a wavy form in which certain parts may favor convection, one can model it in a x-z plane and ignore variations in the y-direction. Pielke's (1974b) 2-D and 3-D numerical simulations of the sea breeze show that a two-dimensional mesoscale model can be used to investigate atmospheric circulations, though neglecting the spatial variations in the third direction. Thus, by proper increase of the horizontal exchange coefficients in the 2-D model, one can produce results comparable with that of a 3-D model with two-dimensional forcing. This adjustment also takes into account horizontal fluxes which the 2-D model cannot properly handle, but which appear in the 3-D case through the vortex stretching mechanism and the consequent energy cascade into the finer scale eddies (Leith, 1968, 1969). Ultimately, a full three-dimensional dry line model will be needed to obtain realistic solutions. Nevertheless, aside from its simplicity and ease in application, the 2-D model provides a valuable intermediate tool to examine the theoretical properties of dry line development. An example further supporting this slab-symmetric formalism can be seen in the mean dew-point temperature field for spring in the central Great Plains (Fig. 2.1), as well as in the smoothed topography (Fig. 2.2).

Coordinate System and Grid Resolution

The dry line may extend in a long distance lengthwise (north-south direction) but otherwise is a mesoscale feature. The grid resolution in the numerical model must fit the dry line characteristics. In order to better describe the smaller-scale features near the dry line and also to minimize computer storage, a stretching type coordinate is designed for the east-west (x) direction. The stretching is to be symmetric about the center grid point. For 25 total horizontal grid points, two kinds of stretched grid systems have been used in this study. The grid points are located at a distance x from the center grid-point i = 13, in the two systems shown in Table 2.1. The total horizontal span for grid system A is approximately 1500 km while that of system B is approximately 1200 km. Two different grid systems are adopted for different purposes. The coarser grid system A is used where larger displacements of the dry line are expected, while the finer grid system B is used for the study of finer changes in the dry line environment. Computer

Table 2.1. Horizontal distances (km) to each grid point. The origin is set at the middle grid point i = 13.

Grid System A: $d_1 = 10$ km, $d_i = 1.3\ d_{i-1}$

grid point i	13	14 12	15 11	16 10	17 9	18 8	19 7
distance x	0	±10	±23	±39.9	±61.87	±90.431	±127.56
grid point i	20 6	21 5	22 4	23 3	24 2	25 1	
distance x	±175.828	±238.577	±320.15	±426.195	±564.054	±743.269	

Grid System B: $d_1 = 5$ km, $d_i = d_{i-1}\ (1 + 0.025\ d_{i-1})$

grid point i	13	14 12	15 11	16 10	17 9	18 8	19 7
distance x	0	±5	±10.625	±17.041	±24.486	±33.317	±44.098
grid point i	20 6	21 5	22 4	23 3	24 2	25 1	
distance x	±57.784	±76.153	±102.957	±147.722	±242.585	±562.423	

programs are coded in a way that makes it easy to change grid systems without major modifications. It should be noted that use of overly stretched grid systems should be avoided. The reason for this will be addressed later in the numerical noise section of this chapter.

A simple terrain-following coordinate is used to replace the regular z-coordinate. Thus,

$$\hat{z} = z - z_G(x) \ , \tag{2.1}$$

where $z_G(x)$ is the ground elevation. The vertical grid interval $\Delta\hat{z}$ is set equal to 200 m except for the first grid interval where 25 m is nominally assigned for the height of the surface layer. With suitable ABL parameterization, the use of a coarser vertical grid system will not seriously affect the solutions as is noted in the study of Pielke (1975b).

It is also noted that the vertical extent of this numerical model (4.625 km for 25 total grid points) is not high enough to study deep convective systems, nor will the boundary layer to the west of the dry line be kept within the domain of this model. It is felt by the author, however, that it is adequate for this study of dry line evolution, since the height of the moist mixing layer seldom exceeds 3 km and the model emphasizes only the pre-storm analysis.

Boundary Layer Processes

One of the focal points in this study is in the evaluation of various boundary layer processes relevant to the dry line evolution. The following is a list of several important processes to be included and tested in the model.

Vertical mixing

When the lower part of the atmosphere is characterized by negative gradient Richardson numbers, i.e., low static stability and strong vertical wind shear, the vertical mixing process will be activated by different sizes of turbulent eddies. Through vertical fluxes of momentum, heat and moisture, the ABL will not only become well mixed but also the depth of the mixing layer will continue to grow in response to the thermal forcing at the earth's surface. The moisture content and its distribution in the heated ABL is also dictated by this mixing process. This explains the usual mid-afternoon minimum showing in the diurnal march of specific humidity in the lower ABL when the mixing process is most active (e.g. Schaefer, 1976).

Horizontal mixing

As the dry line is signified by a strong horizontal specific humidity gradient, it is necessary to examine the relative importance that the horizontal mixing process has in regard to the dry line movement. In order to incorporate the effects of the horizontal subgrid-scale fluxes of momentum, heat and moisture in the numerical model, the corresponding covariance terms (e.g., $\overline{u'u'}$, $\overline{u'v'}$, $\overline{u'\theta'}$ and $\overline{u'q'}$) are parameterized through the use of horizontal exchange coefficients. Many of the previous mesoscale models use the conventional approach to formulate the horizontal eddy coefficients by relating them to the deformation in the wind field (e.g., Deardorff's (1972) 3-D model).

It is known that two-dimensional turbulence has different properties than that of the 3-D case; the vorticity of fluid parcels is conserved as long as friction plays no role. Unlike the energy cascade mechanism in 3-D turbulence, the two-dimensional case is governed by the enstrophy (or one-half of the mean-square vorticity) cascade theory (Leith, 1968). The vorticity fluctuations in the 2-D case will move toward smaller scales and the vorticity gradient will generally increase until molecular diffusion takes over. Therefore, it is suggested (Leith, 1969) that the 2-D eddy viscosity must be a function of the gradient of vorticity. One form of the 2-D eddy exchange coefficient based on this theory (Pielke, 1974b) is

$$K_H = \alpha_{2D}(\Delta x)^3 \left|\frac{\partial \zeta}{\partial x}\right| , \tag{2.2}$$

where $\zeta = \frac{\partial w}{\partial x} - \frac{\partial u}{\partial z}$ is the vorticity in the x-z plane, α_{2D} is a constant coefficient that is to be optimized in the numerical experiment. A similar form modified to accommodate the current terrain coordinate is used in this study;

$$K_H = \alpha'_{2D}(\Delta x)^3 \left| \left[\frac{\partial \hat{w}}{\partial x} + z'_G \left(\frac{\partial u}{\partial x} - \frac{\partial \hat{w}}{\partial \hat{z}} \right) - z_G'^2 \frac{\partial u}{\partial \hat{z}} - \frac{\partial u}{\partial \hat{z}} \right] \right| , \qquad (2.3)$$

where the coefficient α'_{2D} will be properly weighted according to the grid spacing to give the best results.

Advection

Advection by the wind field accounts for much of the change in many atmospheric phenomena. The prevailing wind field could have a profound influence on the diurnal variation of dry line movement, and differential advection with height will also affect its vertical structure. Mahrt (1976) noted that the frequent occurrence of significant decrease of moisture with height in the mixed layer over the U.S. High Plains could be related in part to the growth of the mixing layer into dry air aloft and also to the variation with height of horizontal moisture advection. It was also found that vertical velocity induced by variations in the horizontal velocity could play an important role in controlling the expansion of the mixed layer.

Terrain effects

Some important terrain effects influencing the boundary layer processes are terrain-induced advection, mechanical orographic uplifting producing vertical motion and mixing, topographical forcing as wave sources, and differential heating over sloping terrain. An exhaustive investigation of terrain effects on the boundary layer processes is beyond the scope of this dry line study; however, a simple inclusion of the sloping terrain effect is incorporated in the model through the use of $\hat{z}$-coordinate transformation. Its effect is examined by comparison with the flat terrain case.

Mean Velocity Field Modelling

Vertical transfer of momentum, heat, and moisture in the turbulent ABL have been treated in many different ways. One simple approach is to utilize the conventional eddy viscosity hypothesis, or the so-called K-theory. This type of closure modelling is sometimes referred to as the mean velocity field (MVF) model (c.f. Mellor, 1973). The strategy has proved to be useful in many numerical models (e.g., Estogue, 1963; Krishna, 1968; Sasamori, 1970); it requires less computing power. Despite the non-rigorous nature of the flux-gradient relationship, and the expressions for the eddy exchange coefficients are somewhat arbitrary, it can realistically simulate the diurnally varying ABL in the two-dimensional numerical models. Although higher-order closure models overcome the above mentioned shortcomings and are superior to the K-theories on physical grounds, their extensive computations and their still-evolving closure complexities make their use unrealistic at this stage. Thus, the MVF approach is adopted in this numerical study.

The computations in the ABL conveniently divide into two parts - the surface layer and the turning layer (Ekman layer).

The turbulent structure in the surface layer (constant-flux layer or contact layer) and the needed computational procedures are well established now. The Monin-Obukhov similarity theory is especially powerful in this regard. Vertical eddy coefficients are computed through the normalized profile functions of wind, potential temperature, and specific humidity. Up-to-date formulations for the surface layer are outlined in Appendix A which is centered around the uses of Businger's (1973) empirical profile functions.

Computations of eddy coefficients in the turning layer can also be related to other parameters in different ways; for instance, one can formulate these coefficients by relating them to the:

(i) height of the ABL,

(ii) average vertical wind shear,

(iii) local lapse rate of potential temperature,

(iv) surface heat and momentum fluxes,

(v) local gradient of buoyancy or local turbulent kinetic energy (TKE).

The first formalism is widely used in many current investigations because of its simplicity and its broad applicability to various atmospheric conditions (barotropic, baroclinic, stable, neutral and unstable stratifications).

Many profile functions for these K's have been employed. Examples are Estoque's (1963) linear distribution and McPherson's (1968) exponential profile. One commonly used scheme (O'Brien, 1970) is outlined in Appendix A. This Hermite polynomial profile is favorably used because of its physically realistic distribution.

The Growth of the Mixing Layer, the Inversion Rise Formalism

As the ground is heated by solar radiation, convection and vertical mixing processes take place in the atmospheric boundary layer. Consequently, the temperature profile within the convective ABL is very close to dry adiabatic provided that no other diabatic heating occurs. Next to the ground, it is marked by a super-adiabatic layer as a result of successive heating of the surface. Directly above the mixed ABL it is often capped by a stably stratified inversion layer. The foregoing structure is well illustrated in the x-z cross-sectional θ-field (Fig. 4.17) and in the vertical θ-profile at a fixed grid point (Fig. 4.20a).

It is this capped inversion layer which acts as a lid to prevent the escaping of pollutants and water vapor from the mixing layer below. As a result, it is usually observed that the specific humidity decreases sharply above the mixing boundary layer (e.g. Fig. 4.21). The concentration of isohumes above the ABL is also present in Shaefer's (1974) dry line analysis. In this study cross-sections of specific humidity related field variables (relative humidity, dew-point temperature and wet-bulb potential temperature) also distinguish the mixed ABL from its overlying layer (Figs. 4.22, 4.23, and 4.27). The concentration of isopleths at the top of the ABL and the diurnal growth of the mixed layer are also well depicted in these cross-sections.

As the depth of the ABL is subject to change during the course of the day, it is desirable to formulate a prognostic equation to predict the rate of rise of the inversion. Generally, deepening of the mixed layer is dictated by the rate of entrainment of the warmer overlying air flow into the ABL, the lapse rate of potential temperature in the capping layer, and large scale subsidence along with advection at the base of inversion. As a rule, simplified theoretical modeling of this kind may be based on thermodynamic considerations and/or on energetics theory. Conservation principles allow us to relate the unsteady potential temperature to the kinematic heat flux in the mixed layer (e.g., Ball, 1960). An enthalpy equation will relate the heating rate within the ABL to the heat-flux divergence, which in turn will be related to the downward heat flux from above, the upward surface heat flux, and the height of inversion base ($\hat{z}_i$), under the assumption of a self-preserving potential temperature profile in the well-mixed underlying layer. The entrainment velocity is related then to the turbulent heat flux at the inversion base by some type of entrainment assumption. In order to close the problem, one should determine the heat flux at the inversion base as a function of the surface heat flux. Usually this is done through the parameterization of the turbulent kinetic energy equation using some scaling velocities; normally these are taken from free-convection similarity theory (Tennekes, 1973; Zilitinkevich, 1975; Mahrt and Lenschow, 1976). The proportionality constant is determined from experimental data (Deardorff et al., 1969).

In obtaining the entrainment velocity, it is also natural to introduce a parameter related to the inversion strength. By simple consideration of the balance between the entraining downward heat flux and the rate of enthalpy loss, the simple model yields the entrainment rate (Lilly, 1968):

$$\frac{d\hat{z}_i}{dt} = - \frac{(\overline{\theta' w'})_i}{\Delta\theta} . \tag{2.4}$$

The potential-temperature jump ($\Delta\theta$), however, is usually unknown and is a prognostic variable itself. Thus, further closure procedures are needed to put (2.4) into practice (e.g., Tennekes, 1973). Jump models used in previous studies (Lilly, 1968; Carson, 1973; Tennekes, 1973; Mahrt and Lenschow, 1976; Zeman and Tennekes, 1977) and the other type of prediction model based on the TKE theory (Stull, 1976) are likely to be ideal for the one-dimensional theoretical investigation.

For numerical 2-D or 3-D modelling, it is necessary to use a simple-to-apply yet realistic prognostic equation for the prediction of the inversion height. One such equation which includes all the aforementioned relevant processes and empirical constants determined from laboratory simulations and observations (e.g., Wangara data) is due to Deardorff (1974):

$$\frac{\partial \hat{z}_i}{\partial t} = -u\,\frac{\partial \hat{z}_i}{\partial x} + w_i + 1.8\,(\overline{w'\theta'})_s/[\hat{z}_i\,(\frac{\partial \theta}{\partial \hat{z}})^{+} + \frac{9w_*^2}{\beta \hat{z}_i}] \quad . \qquad (2.5)$$

The first term on the right-hand side is the advection of inversion height as a result of non-uniform boundary-layer depth. The second term is the large-scale subsidence velocity and is usually unknown. It can be obtained from the averaged observations. The third term accounts for convective boundary-layer activities, i.e., the deepening of $\hat{z}_i$ due to heat fluxes and the lapse rate directly above the inversion $(\frac{\partial \theta}{\partial \hat{z}})^{+}$. The second term in parenthesis is entered to compensate the singularity when $(\frac{\partial \theta}{\partial \hat{z}})^{+}$ approaches zero. $w_* = [\beta(\overline{w'\theta'})_s\ \hat{z}_i]^{1/3}$ is the vertical scale velocity in the convective ABL. It is derived from free-convection similarity theories and has a maximum magnitude of $2 \sim 3$ m s^{-1}, occurring in this dry line simulation during the mid-afternoon hours when the convection is most intense. The third term also dominates the advective term by an order of magnitude (e.g., 10^{-2} ms^{-1} versus 10^{-3} ms^{-1} during the convective period). As will be seen in the results shown in later chapters, (2.5) successfully predicts the daytime convective boundary layer in the dry line environment, for both the moist mixing-layer height and the drier ABL in the western domain. Other examples of success in using this type of prognostic equation are also seen in the 3-D ABL simulation of Deardorff (1974) and in the 2-D sea-breeze simulation of Pielke and Mahrer (1975).

The ABL height for the neutral case is conventionally assigned to be 0.35 u_*/f, a result based on dimensional arguments.

Much remains unknown regarding stable atmospheric boundary layers when a cool underlying surface exists (e.g., nocturnal ABL). Their depths are generally small compared to that of a neutral case and are not much affected by advection and vertical velocity. Thus, a practical prognostic equation for the depth is difficult to determine. One diagnostic derivation based on dimensional analysis is due to Zilitinkevich (1972), where the normalized ABL height is inversely proportional to the square root of the stability parameter; i.e.,

$$\frac{z_i f}{u_*} = c\left(\frac{u_*}{fL}\right)^{\frac{1}{2}} , \tag{2.6}$$

where the constant coefficient c has to be determined. A power law similar to (2.6) based on K-theory was derived by Businger and Arya (1974). An empirical interpolation diagnostic formula due to Deardorff (1972) will be employed here:

$$\hat{z}_i = \left(\frac{1}{aL} + \frac{f}{bu_*} + \frac{1}{H_{trop}}\right)^{-1}, \tag{2.7}$$

where L is the Monin-Obukhov length and H_{trop} denotes the height of the tropopause; a and b are constants. This formula can be used for the neutral case also, since in that case L approaches infinity and the first term in parenthesis goes to zero. The last term is entered to ensure that the ABL height will not exceed H_{trop} near the equator where f becomes small. In the extremely stable case where $\hat{z}$ is unimportant (z - less stratification), the first term in parenthesis dominates others. In this study, the constants a and b are numerically adjusted according to the characteristic magnitudes of f, L and u_* determined in the surface layer computations. The last term can be dropped since we are only concerned with mid-latitude phenomena.

Model Equations

The governing equations written in terrain coordinates will consist of the following:

Momentum equation

$$\begin{aligned}\frac{\partial u}{\partial t} + u\frac{\partial u}{\partial x} + \hat{w}\frac{\partial u}{\partial \hat{z}} &= f v - \hat{f}(\hat{w} + uz'_G) - \theta\frac{\partial \pi}{\partial x} - g z'_G \\ &+ \frac{\partial}{\partial x}\left(K_H \frac{\partial u}{\partial x}\right) + \frac{\partial}{\partial \hat{z}}\left[K_z^{(m)} \frac{\partial u}{\partial \hat{z}}\right] + z_G'^2 \frac{\partial}{\partial \hat{z}}\left(K_H \frac{\partial u}{\partial \hat{z}}\right) \\ &- z'_G\left[\frac{\partial}{\partial x}\left(K_H \frac{\partial u}{\partial \hat{z}}\right) + \frac{\partial}{\partial \hat{z}}\left(K_H \frac{\partial u}{\partial x}\right)\right]\end{aligned} \tag{2.8}$$

$$\frac{\partial v}{\partial t} + u\,\frac{\partial v}{\partial x} + \hat{w}\,\frac{\partial v}{\partial \hat{z}} = -\,f\,u + f\,u_g + \frac{\partial}{\partial x}(K_H\,\frac{\partial v}{\partial x})$$

$$+ \frac{\partial}{\partial \hat{z}}[K_z^{(m)}\,\frac{\partial v}{\partial \hat{z}}] + z_G'^2\,\frac{\partial}{\partial \hat{z}}(K_H\,\frac{\partial v}{\partial \hat{z}})$$

$$-\,z_G'[\frac{\partial}{\partial x}(K_H\,\frac{\partial v}{\partial \hat{z}}) + \frac{\partial}{\partial \hat{z}}(K_H\,\frac{\partial v}{\partial x})] \qquad (2.9)$$

<u>Thermodynamic equation</u>

$$\frac{\partial \theta}{\partial t} + u\,\frac{\partial \theta}{\partial x} + \hat{w}\,\frac{\partial \theta}{\partial \hat{z}} = \frac{\partial}{\partial x}(K_H\,\frac{\partial \theta}{\partial x}) + \frac{\partial}{\partial \hat{z}}[K_z^{(H)}\,\frac{\partial \theta}{\partial \hat{z}}] + z_G'^2\,\frac{\partial}{\partial \hat{z}}(K_H\,\frac{\partial \theta}{\partial \hat{z}})$$

$$-\,z_G'[\frac{\partial}{\partial x}(K_H\,\frac{\partial \theta}{\partial \hat{z}}) + \frac{\partial}{\partial \hat{z}}(K_H\,\frac{\partial \theta}{\partial x})] \qquad (2.10)$$

<u>Specific humidity budget equation</u>

$$\frac{\partial q}{\partial t} + u\,\frac{\partial q}{\partial x} + \hat{w}\,\frac{\partial q}{\partial \hat{z}} = \frac{\partial}{\partial x}(K_H\,\frac{\partial q}{\partial x}) + \frac{\partial}{\partial \hat{z}}[K_z^{(H)}\,\frac{\partial q}{\partial \hat{z}}] + z_G'^2\,\frac{\partial}{\partial \hat{z}}(K_H\,\frac{\partial q}{\partial \hat{z}})$$

$$-\,z_G'[\frac{\partial}{\partial x}(K_H\,\frac{\partial q}{\partial \hat{z}}) + \frac{\partial}{\partial \hat{z}}(K_H\,\frac{\partial q}{\partial \hat{x}})] \qquad (2.11)$$

<u>Equation of continuity</u>

$$\frac{\partial u}{\partial x} + \frac{\partial \hat{w}}{\partial \hat{z}} = 0 \qquad (2.12)$$

<u>Hydrostatic equation</u>

$$\frac{\partial \pi}{\partial \hat{z}} = -\,\frac{g}{\theta} \qquad (2.13)$$

where $\hat{w} = \frac{d\hat{z}}{dt} = w - u\,z_G'$ and $z_G' = \frac{dz_G}{dx}$ is the slope of the terrain. In the U.S. Central Great Plains a constant terrain slope is a fair approximation. The map factor is neglected in this system since it is not important in this diagnostic study. $f = 2\Omega \sin\varphi$ and $\hat{f} = 2\Omega \cos\varphi$ are taken to be constants corresponding to a latitude $\varphi = 35^\circ$N. A constant pressure gradient along the y-direction is imposed, i.e.,

$$u_g = -\frac{\theta}{f}\frac{\partial\pi}{\partial y} = \text{constant.}$$

The Exner function π, as defined in the list, replaces p. In the prognostic equations (2.8) to (2.11), terms describing fluxes of momentum, heat, and moisture have been parameterized according to K-theory as noted earlier. The thermodynamic equation is written using potential temperature instead of temperature itself because of the parameterization of the diabatic heating term $(\frac{\theta\dot{Q}}{c_p T})$. $\dot{Q} = \frac{dQ}{dt}$ stands for the diabatic heating rate due to various sources; e.g., horizontal and vertical turbulent heat fluxes, radiation, or realization of latent heat. A simplified form of radiative cooling was tested in an earlier run of the model and it was found that it played no crucial role. Thus, the radiative term will be neglected here. Cumulus parameterization will also not be included at this stage as this is a relatively shallow model. Therefore, only sources representing horizontal and vertical eddy fluxes have been considered on the right-hand side of the energy equation.

The specific humidity equation, similar to the energy equation, also assumes no other sources or sinks, except that described in the last section of Chapter III, where north-south moisture advection is tested.

This is not a simulation of violent convection; thus, the smallness of the vertical motion and the shallowness of the model also validates our hydrostatic and quasi-incompressible approximations.

In the case of a general terrain with curvature, the corresponding curvature terms (e.g., $z''_G K_H \frac{\partial u}{\partial \hat{z}}$ in the u-equation and similar terms for other equations) may be included. Mesoscale models with hilly/wavy terrain are usually numerically difficult to deal with unless special procedures are incorporated (e.g., gradual growth of mountain in the course of the integration, or other transformations such as that of Taylor, 1977).

Finite Difference Analogue

The numerical procedure used in this integration is the usual centered-time (leap-frog) and the centered-space differencing scheme of second-order accuracy. For the initial step forward-time differences are utilized. In order to avoid computational instability (Haltiner, 1971), all the diffusive terms have been computed by lagging one time step. Unlike the multiple-step schemes or the implicit/semi-implicit methods, this scheme has the advantage of simplicity in application, yet meets the required accuracy. There is no built-in damping effects (e.g., as in the forward-time and upstream scheme).

Owing to the uneven grid mesh used in the x-direction, horizontal space-derivatives of dependent variables (say, φ) are approximated by direct interpolation of derivatives half-way through the grid interval (Fig. 2.3), i.e.,

$$\varphi'(x_i) \sim \hat{\delta}_x \varphi_i = \frac{d_{i-1}}{d_i + d_{i-1}} \delta_x \varphi_{i+\frac{1}{2}} + \frac{d_i}{d_i + d_{i-1}} \delta_x \varphi_{i-\frac{1}{2}} \tag{2.14}$$

where

$$\begin{aligned} \delta_x \varphi_{i+\frac{1}{2}} &= \frac{\varphi_{i+1} - \varphi_i}{d_i} , \\ \delta_x \varphi_{i-\frac{1}{2}} &= \frac{\varphi_i - \varphi_{i-1}}{d_{i-1}} . \end{aligned} \tag{2.15}$$

Thus, through the operator δ_x in (2.15), we have defined a new operator $\hat{\delta}_x$ in (2.14) to approximate derivatives in this grid system. The regular difference operator δ will also apply to the time derivative and the z-derivative, i.e.,

$$\begin{aligned} \delta_t \varphi^n &= \frac{\varphi^{n+1} - \varphi^{n-1}}{2\Delta t} , \\ \delta_z \varphi_j &= \frac{\varphi_{j+1} - \varphi_{j-1}}{2\Delta \hat{z}} . \end{aligned} \tag{2.16}$$

The left-hand side of the prognostic equations are first rewritten in flux/momentum form through the use of continuity equation (2.12). The finite difference equations for (2.8) to (2.13) may be written as

$$\begin{aligned} \delta_t u + \hat{\delta}_x (u\,u) + \delta_z (u\,\hat{w}) &= f\,v - \hat{f}(\hat{w} + u\,z'_G) - \theta\,\hat{\delta}_x \pi \\ &- g\,z'_G + \hat{\delta}_x (K_H \hat{\delta}_x u) + \delta_z [K_z^{(m)} \delta_z u] + z'^2_G \delta_z (K_H \delta_z u) \\ &- z'_G [\hat{\delta}_x (K_H \delta_z u) + \delta_z (K_H \hat{\delta}_x u)] , \end{aligned} \tag{2.17}$$

$$\delta_t v + \hat{\delta}_x (u v) + \delta_z (v \hat{w}) = - f u + f u_g + \hat{\delta}_x (K_H \hat{\delta}_x v) + \delta_z [K_z^{(m)} \delta_z v]$$

$$+ z_G'^2 \delta_z (K_H \delta_z v) - z_G' [\hat{\delta}_x (K_H \delta_z v) + \delta_z (K_H \hat{\delta}_x v)] , \qquad (2.18)$$

$$\delta_t \theta + \hat{\delta}_x (u \theta) + \delta_z (\theta \hat{w}) = \hat{\delta}_x (K_H \hat{\delta}_x \theta) + \delta_z (K_z^{(H)} \delta_z \theta]$$

$$+ z_G'^2 \delta_z (K_H \delta_z \theta) - z_G' [\hat{\delta}_x (K_H \delta_z \theta) + \delta_z (K_H \hat{\delta}_x \theta)] , \qquad (2.19)$$

$$\delta_t q + \hat{\delta}_x (u q) + \delta_z (q \hat{w}) = \hat{\delta}_x (K_H \hat{\delta}_x q) + \delta_z [K_z^{(H)} \delta_z q]$$

$$+ z'^2_G \delta_z (K_H \delta_z q) - z_G' [\hat{\delta}_x (K_H \delta_z q) + \delta_z (K_H \hat{\delta}_x q)] , \qquad (2.20)$$

$$\hat{\delta}_x u + \delta_z \hat{w} = 0 , \qquad (2.21)$$

$$\delta_z \pi + \frac{g}{\theta} = 0 . \qquad (2.22)$$

Initial Fields

The initial specific humidity field for the numerical simulation is prescribed in a manner to simulate the prevailing dry line environment. A shallow moist mixing layer is located in the eastern part of the domain and a relatively sharp moisture gradient is specified around the middle grid point (i = 13). Also a larger hydrolapse (lapse rate in specific humidity) is imposed above the moist layer.

The potential temperature field is in hydrostatic balance with the Exner function (π) field; the initial north-south wind field is also set in geostropic balance with the π-field above the ABL, while an Ekman frictional balance status is prescribed within the boundary layer. The procedures to obtain the initial wind, potential temperature, and Exner function fields in these balanced states are somewhat arbitrary. The following steps are used for this model.

(i) The initial ABL height $\hat{z}_i$ is higher in the western domain and lower to the east.

(ii) The θ-field is prescribed with an adiabatic profile in the ABL and a constant increase (inversion) of θ above. Temperatures are warm in the west and cooler to the east.

(iii) v is specified at top of the model and π is determined geostrophically by

$$v = \frac{1}{f}[\theta\, \hat{\delta}_x \pi + g\, z'_G] \; . \qquad (2.23)$$

(iv) The π-field is calculated by downward integration of the hydrostatic equation

$$\delta_z \pi = -\frac{g}{\theta} \; . \qquad (2.24)$$

(v) The v-field below the top is computed geostrophically through (2.23).

(vi) The v-field is smoothed.

(vii) A new θ-field is determined by integration of the thermal wind equation:

$$\frac{\partial\theta}{\partial x} = \frac{f\theta}{g}\frac{\partial v_g}{\partial \hat{z}} - \left(\frac{f}{g}\, v_g - z'_G\right)\frac{\partial\theta}{\partial \hat{z}} \; . \qquad (2.25)$$

The boundary condition needed for the integration can be taken from the profile described in (ii).

(viii) The new π-field is computed hydrostatically using the new θ-field.

(ix) u_g is constant throughout the domain.

(x) The wind fields within the ABL are adjusted by numerically solving the Ekman equations:

$$\begin{aligned} \delta_z(K_z\,\delta_z u) + f\,v - \hat{f}\,u\,z'_G - \theta\,\hat{\delta}_x \pi - g\,z'_G &= 0 \\ \delta_z(K_z\,\delta_z v) - f\,u + f\,u_g &= 0\,. \end{aligned} \qquad (2.26)$$

The resulting initial fields are shown in Figs. 2.4 to 2.8 for the different experiments.

Boundary Conditions

Lateral boundaries

Due to the dispersive characteristic of the waves allowed in this hydrostatic-model (c.f. Appendix B), any specified conditions at the boundaries will in general produce numerically ill-posed problems. A set of boundary conditions may be correct for some modes but may be incorrect for others. In this numerical study, the choice of boundary conditions should be based on their ability to control the growth of inertial-gravity waves. Thus, a radiation condition is applied along the lateral boundaries so that wave disturbances generated in the interior domain are allowed to pass out of the boundaries and computational false reflections are minimal.

Two types of treatment of the lateral boundary conditions as described in Appendix C have been tested in this study - one based on the scheme proposed by Orlanski (1976); the other scheme was suggested by Klemp and Lilly (1978) and Klemp and Wilhelmson (1978). Both treatments of the boundaries are modifications of the Somerfeld radiation condition to accommodate mesoscale numerical models. Test runs show that both of these formulations are stable for this numerical model and no significant reflections occur during the entire integration period. It is also found that simple continuity extrapolation for the boundary conditions up to the second-order like those of Nitta (1962) and Matsuno (1966) will not provide stability since strong reflections occur. This is not only due to the dispersive characteristics of the waves allowed by the model but also due to the fact that our expanding grid system (especially near the boundary) will cause more reflections since shorter waves generated in the interior region cannot be adequately resolved in the coarser grid near the boundaries. It is known from this study that erroneous boundary conditions exert an influence in the interior domain faster in an expanding grid system than in a regular grid system.

Upper boundary

The upper boundary condition for the integration of the hydrostatic equation (2.22) is chosen so that faster moving surface gravity waves are not allowed in the model, and only internal waves will be present. Hence, π is fixed timewise at the top of the model to eliminate the external modes.

Because the inertial-gravity waves present in the model can propagate both horizontally and vertically, the upper boundary conditions for the prognostic variables also are necessary to be treated with a radiation type condition to insure stability, especially during the later integration periods. For equal vertical grid intervals, a simple formulation was found to be adequate. Thus, a prognostic variable φ at the top is specified by

$$\varphi_J^{t+1} = 2\,\varphi_{J-1}^{t} - \varphi_{J-2}^{t-1} \; . \tag{2.27}$$

This formulation is equivalent to an outflow condition using time-extrapolation and the assumption that characteristics of vertically propagating waves have a slope equal to $\Delta\hat{z}/\Delta t$.

<u>Lower boundary</u>

At the model bottom, a no-slip condition is assigned, i.e., $u = 0$ and $v = 0$. For the integration of the continuity equation, no mass flux across the surface is allowed and $\hat{w} = 0$ is imposed. An artificial diurnal harmonic forcing is specified for the surface potential temperature, i.e.,

$$\theta(x,t) = \bar{\theta}(x) + A_1(x)\sin[\tfrac{\pi}{18}(1.5t - 14)] + A_2(x)\sin[\tfrac{\pi}{18}(3t + 0.5)] \; , \tag{2.28}$$

where $\bar{\theta}(x)$ is the basic surface potential temperature $A_1(x)$ and

$A_2(x)$, in general vary in the x-direction and time t is measured in hours (local standard time). Since observations of surface temperature are not perfectly sinusoidal, higher harmonics may be needed to describe a closer fitting of the diurnal waves.

Two methods are adopted to specify the specific humidity at the lower boundary. One is to set the surface moisture forcing to be in-phase timewise with the surface thermal forcing; thus,

$$q(x,t) = \bar{q}(x) + B_1(x)\sin[\tfrac{\pi}{18}(1.5t - 14)] + B_2(x)\sin[\tfrac{\pi}{18}(3t + 0.5)] \quad . \tag{2.29}$$

The other technique is to impose a zero vertical q-gradient within the surface layer. This latter strategy is used to specify no moisture flux from the surface so that the influence from the surface forcing will be shadowed and the resulting field is compared to the former case. The forcing functions for θ and q at the center grid point as described by (2.28) and (2.29) are shown in Fig. 2.9 and Fig. 2.10.

Numerical Noises and Filtering

Numerical noise due to time-differencing scheme; time filter

It is a simple matter to demonstrate that the use of a higher-order time-differencing scheme to solve the advection-equation will introduce unwanted computational modes. The three-time-level leap frog scheme used in this study does introduce spurious computational modes (e.g., Haltiner, 1971) which change phase every time step and travel in the opposite direction. Thus, with no smoothing short waves develop and cause the separation of solutions at alternate time steps (Lilly, 1965). In order to avoid this kind of decoupling of the solutions some sort of noise-suppressing procedure must be utilized to prevent the breakdown of the integration. An intermittent use of the first-order difference scheme (e.g., Euler forward-time differencing) is feasible. In this simulation, an efficient way to prevent this time-splitting tendency is to use a time filter such as that of Robert (1966). The algorithm used can be represented by:

$$\begin{aligned} \varphi^{t+1} &= \bar{\varphi}^{t-1} + 2\Delta t\, F^{t} \, , \\ \bar{\varphi}^{t} &= \varphi^{t} + \frac{1}{4}(\varphi^{t+1} - 2\varphi^{t} + \bar{\varphi}^{t-1}) \, , \end{aligned} \qquad (2.30)$$

where φ represents the prognostic variable; the superscript denotes the time level. $\bar{\varphi}$ is the filtered value according to the second step and the first step describes the leap-frog scheme for the equation $\frac{\partial\varphi}{\partial t} = F$. The filter does not require extra core storage and only a little extra CPU computer time is required.

Other source of numerical noises

Similar to the high-frequency time noise, the use of centered-space differences also can produce short-wavelength noise. The two-grid-interval noise (or 2-D wave) can be suppressed by a number of methods. Use of the built-in dissipative scheme (e.g., forward-time upstream scheme) that has selective damping effects for shorter waves, use of linear and non-linear artificial viscosity terms, intermittent use of uncentered space differencing, and use of explicit space smoothing procedures, will damp the spurious short-waves. The source of numerical noise comes from the aliasing errors due to the non-linear interaction of different modes through the advection terms (Phillips, 1956). As noted earlier, in a numerical mesoscale model of this kind, quite frequently numerical noise is also due to the improper specification of the boundary conditions (false reflections may occur). Furthermore, another source of noise is the special arrangement of the grid system. When utilizing the stretched grid mesh, numerical errors such as disturbances of upstream propagating blocks and downstream traveling jumps may occur when disturbances originating in the finer grid region cannot be adequately resolved in the coarser grid.

The explicit smoothing operator, as designed in Appendix E for this special grid system, is effective in damping the short waves described above. It should be noted that only intermittent application of this filter is needed; it is important not to excessively smooth the fields.

CHAPTER III

APPLICATIONS OF THE NUMERICAL MODEL TO THE STUDY OF THE DRY LINE MOVEMENT

Numerical Aspects and Specifications

All numerical simulations will be initiated at the time corresponding to 6 local standard time (LST) and integrated up to one or two diurnal cycles. The time increment Δt is chosen to fulfill both the Courant-Fredrich-Lewy advective and diffusive stability requirements. Thus, the criteria

$$\Delta t \leq \frac{\Delta x}{C_x} \quad , \quad \Delta t \leq \frac{\Delta \hat{z}}{C_z} \; ,$$
$$\Delta t \leq \frac{\Delta x^2}{2K_H} \quad , \quad \Delta t \leq \frac{\Delta \hat{z}^2}{2K_z} \; , \tag{3.1}$$

must be satisfied during the course of the integration. A choice of $\Delta t = 60$ sec will satisfy these criteria when grid system A is utilized

An upper limit of $K_z = 120\ m^2 s^{-1}$ is imposed for the vertical eddy viscosity and $K_z = 0.001\ m^2 s^{-1}$ is assigned above the ABL. A roughness length of $z_o = 0.1$ m and the height of the surface layer $z_h = 25$ m are specified.

As a part of horizontal diffusion, the horizontal smoothing operator (E.1) is applied to the prognostic variables every two hours. Although this is not a minimum requirement for numerical stability, it provides the required smooth solutions without the contamination of 2-D irregularities. Similarly, a symmetric elementary filter which has a response function equivalent to (E.7) is also applied vertically with less frequency. Vertical smoothing is only required 14 hours after initiation and is applied every two or four hours depending on the type of simulation.

In order to examine the importance of different ABL processes relevant to the diurnal motion of the dry line, a series of simulations with different moisture-budget equations are carried out. Simulations with simplified equations representing different processes and with different forcing conditions are conducted and comparisons are made. For ease of description, the various simulations are classified as shown below.

Tests of ABL Processes Relevant to Movement of Dry Line

Control case A

The experiment is designed to include all of the proposed relevant processes and the complete set of equations (2.8)-(2.13) are used. The initial fields are those described in Fig. 2.4 - Fig. 2.8. The surface forcing functions for θ and q are described by (2.28) and (2.29) with constant amplitudes: $A_1 = 6^\circ K$, $A_2 = 1.5^\circ K$, $B_1 = 1\ g\ kg^{-1}$ and $B_2 = 0.25\ g\ kg^{-1}$. Other assigned constants are $u_g = 1\ m\ s^{-1}$ and $z'_G = -1/600$. This case will be referred to as Case A_1. As mentioned earlier in the previous chapter, another strategy for specifying the lower boundary condition for q is to adopt a zero vertical gradient in the surface layer. This will be Case A_2. A numerical integration for one diurnal cycle is performed. Only examinations regarding the dry line movement will be presented in this chapter. Further discussion of related fields will be given in the following chapter.

The best way to show the diurnal tendency in the displacement of the dry line is by the use of horizontal time sections (i.e., x-t cross-section). By convention, it is usual to locate the dry line position by the distribution of specific humidity or dew-point temperature. Rhea (1966) used the surface wind convergence zone to define the dry line location. It is found in this study that there is no qualitative difference in describing the movement of the dry line by the use of the specific humidity field or by the use of dew-point temperature. It is not appropriate to use the wind convergence zone for the study of dry line motion, since the convergence zone is more or less related to the development of the LLJ, which usually exhibits only a little diurnal displacement.

The resulting time sections for the specific humidity as well as the dew-point temperature at the top of surface layer (the second vertical grid-point) are shown in Figs. 3.1-3.4 for Case A_1 and Case A_2. It is apparent from these sections that the isopleths exhibit systematic diurnal displacement in these simulations. The dew-point temperature shows the same tendency as the specific humidity for both cases. For convenience, one can consider the dry line location as the position of the 10 $g\,kg^{-1}$ (or 8 $g\,kg^{-1}$) isoline in the q-section and 288°K (or 284°K) in the θ-section. These isopleths are located initially at the middle grid point (or one grid point further west).

There are large differences in the dry line displacement for Case A_1 and Case A_2, indicating that the surface moisture-fluxes have profound influences on the evolution of the moist boundary layer. Only little eastward displacement of the surface dry line during the convective period and little westward return during the nighttime occurred in Case A_1; while in Case A_2, the dry line moves out of the eastern domain at about 16-19 LST. The diurnal movement of the dry line is especially obvious for Case A_2 - it shows a little westward displacement in the early morning and a rapid eastward movement during the surface-heating period and exhibits a nocturnal return after sunset. The nocturnal return of the surface dry line is not seen in Shaefer's (1974) model-simulation but does appear in his observational analysis. The discrepancy is probably due to the improper assignment of the depth of the ABL which not only will affect the moisture field but also can result in a different wind and thermal structure within the boundary layer. Another factor could be partly due to the neglect of the horizontal mixing process as will be indicated in the later experiments. Quantitatively, the eastward movement of the dry line during the heating period could be very fast according to the Case A_2 simulation, averaging up to ~70 km hr^{-1} during the mid-afternoon hours. It remains relatively stationary after midnight. Only a few kilometers of westward return occurs during the early morning hours, while most of the nocturnal return occurs after sunset and before midnight.

In order to examine the influence of the surface moisture-flux at levels farther from the surface layer, a similar time section (Fig. 3.5) is produced for Case A_1 at the 4th vertical grid-point (425 m above the surface). From the tendency of the 10 g kg^{-1} isopleth, a greater displacement of the dry line is experienced at this level and there is almost no nocturnal return. Thus, a change of the initial vertical step profile to a tilt profile is expected as time elapses (as can be seen from the moisture field-section in Fig. 5.1). This can be explained by the effect of differential advection with height as is seen in the development of vertical wind shear in the u-component wind field (Fig. 4.1c).

It is also noted that, because of the diffusive character inherent in the horizontal mixing terms in the governing equations, the diffuseness of the isopleths in these time sections during the later period is expected.* Naturally, a gradual decrease of the initial sharp gradient in the vicinity of the dry line and an eventual loss of dry line identity will be experienced as time elapses, unless other physical processes counteract this diffusive process. Since at this time we are mostly interested in movement of the dry line, we will only be concerned with the tendency in the displacement of the isopleths.

In Case A_1, we believe that we impose too much moisture-forcing at the lower boundary. The smaller displacement resulting in this case can be attributed to the boundary condition where we have imposed a fixed spatial distribution of the basic moisture content. Therefore, for further tests of individual processes affecting the dry line movement the results will be compared with Case A_2.

Test of vertical mixing process (Case B)

In order to examine the importance of the vertical turbulent mixing process in the evolution of the dry line, the moisture budget equation (2.11) is simplified to a vertical diffusion equation; otherwise, Case B is identical to the control Case A_2. The resulting time section (Fig. 3.6) is compared to that of Case A_2 (Fig. 3.3). Immediately, from

---

*These prognostic equations are similar to Burger's equation provided that the Coriolis term, the pressure-gradient term and one of the space independent-variable are neglected.

the similarity of the two time-sections, one can see that vertical mixing is the main ABL process responsible for the eastward movement of the dry line during the convective period (1000-2000 LST). The absence of the nocturnal return in Case B also enables us to attribute the cause of the nighttime movement of the dry line to other processes (horizontal mixing and advection), since during the nighttime and early morning hours the vertical turbulent mixing process is inactive. These two processes counteracting the vertical-mixing effect cause a slightly reduced speed of movement of the daytime dry line in Case A_2 as compared to that of Case B. It is noted that the vertical step profile is maintained fairly well throughout the diurnal cycle when the vertical mixing is acting alone (Fig. 3.14).

Test of horizontal mixing process (Case C)

A test of the horizontal mixing process is done by allowing only horizontal mixing terms in Eq. (2.11). Fig. 3.7 shows the time-section for a one day integration; uneven spreading of the isopleths is noted. This result is somewhat different from that obtained if we adopt a simple horizontal diffusion equation with constant exchange coefficients. Since we use a kinematic-field-dependent formulation for the horizontal exchange coefficient (cf. Chapter II), uneven spreading of the moisture isopleths results in response to the vorticity gradient. At any rate, it is noted from Fig. 3.7

that the horizontal mixing process could account for a significant amount of the westward displacement of the nocturnal dry line.

Test of the effect of horizontal advection in the dry line environment (Case D)

Following the simulations of Case C, it is also necessary to investigate the effect of horizontal advection on the evolution of the moisture field. When (2.11) is simplified to a horizontal advection equation and the simulation is carried out, redistribution of the moisture field solely due to advection can be studied. As shown in Fig. 3.8, the initial isoline of 10 g kg^{-1} can be traced through the whole diurnal cycle and a general westward displacement is noted. This tendency is not surprising if one notes the diurnal development of the easterly winds in the lower part of the ABL (Fig. 4.1a-4.1c). Fig. 3.8 also indicates that the advection process is capable of sharpening the moisture gradient; note the packing of the isopleths in the western portion of the domain.

Other Factors Affecting the Evolution of the Dry Line

Effect of sloping terrain (Case E)

In an attempt to study the effect of sloping terrain, a zero-slope version of the model equations is used and the results are compared to those obtained for Case A_2. The initial fields are specified as in the control case but with $z_G' = 0$. Further discussion of the terrain effect on the wind field and the evolution of the boundary layer will be given in the next chapter. Here, only the time-section of specific humidity (Fig. 3.9) is considered. By comparing this figure with Fig. 3.3 for Case A_2, it can be seen that the nocturnal return of the dry line is almost absent in the flat-terrain case due to the weaker development of the ABL wind field (Fig. 4.8). Fig. 3.9 is similar to the result for Case B (Fig. 3.6), indicating that horizontal advection and mixing are not as important as in the case of sloping terrain.

Effect of different depth of moist mixing-layer (Case F)

It has been observed (Schaefer, 1973) that quite often the depth of the moist layer increases toward the east. One experiment, similar to Case A_2, but with a deeper initial moist layer as shown in Fig. 3.15, is conducted. The consequence, as seen from Fig. 3.10, is a significant reduction of the eastward displacement of the dry line when compared to the simulation with a shallower moist layer (Fig. 3.3). Thus, we conclude that the depth of the moist layer exerts a major influence on the movement of the dry line, especially during the heating period when the elimination of the surface dry line is mainly due to eddy mixing processes.

Effect of a constant north-south pressure-gradient force - the east-west geostrophic wind (Case G)

Specification of a constant geostrophic wind, u_g, imposes a constant forcing on the wind fields. In this experiment, an easterly geostrophic wind ($u_g = -1 \text{ m s}^{-1}$) is specified instead of a westerly wind as in Case A_2. By comparing Fig. 3.11 to Fig. 3.3 it can be seen that there is a larger westward-displacement during the nighttime and early morning hours. This confirms that the influence of this easterly geostrophic wind comes into play only when the convective eddy-mixing process is absent.

<u>Effect due to differential thermal and moisture forcing at the lower boundary (Case H)</u>

A test of horizontal differential heating and uneven surface-moisture forcing is done by varying the amplitudes of the forcing functions given by (2.28) and (2.29). For a simple test, linear functions are specified for A_1 and B_1, i.e.,

$$A_1(x) = 10 - 6x/L \quad (^{\circ}K) ,$$

$$B_1(x) = 0.5 + 3x/L \quad (g\ kg^{-1}) ,$$

where L is the horizontal dimension of the domain. Other parameters are the same as in Case A_1. This produces a weaker thermal forcing and a stronger moisture forcing in the eastern domain and reverse conditions to the west. Aside from the changes in the wind field and the thermal field which will be discussed in the following chapter, a smaller daytime eastward displacement occurs in this simulation (Fig. 3.12) compared to Case A_1 (~50 km less). Larger differences would occur if a larger horizontal gradient of the amplitudes A_1 and B_1 is specified. The result also supports the previous finding that thermally forced eddy-mixing is the physical process primarily responsible for the daytime movement of the dry line. Stronger moisture forcing at the earth's surface will also cause a reduction in the dry line motion.

Effect of thermal and moisture advection in the north-south direction (Case I)

Although the movement of the dry line may be quite sporadic and can be complicated by three-dimensional effects which cannot be described in this two-dimensional model, a cursory examination of the third-direction effects can be conducted through the inclusion of an approximate north-south advection term in the energy equation as well as in the moisture budget equation. This is necessary because of the strong southerly LLJ which not only transports a significant amount of heat energy northward but also advects abundant moisture into the Central Great Plains (e.g. Means, 1952). The frequently observed moisture tongue in this region is closely related to the LLJ. Therefore, in this simulation, an advection term in the y-direction is added to the energy equation (2.10) and the moisture equation (2.11). Thus, for (2.10) $v \frac{\partial \theta}{\partial y} \sim v \times (-1^{\circ}K/100\ km)$ is added, and for (2.11) $v \frac{\partial q}{\partial y} \sim v \times (-2\ g\ kg^{-1}/1000\ km)$ is incorporated. These are conservative estimates of the north-south gradients of potential temperature and specific humidity. In the vicinity of the dry line, these gradients can be larger than the above values.

One should expect some changes in the diurnal variation of the wind field as well as the thermal field because of these advection terms; these will be analyzed later. Here, only the tendency of dry line movement is discussed. It is observed that (Fig. 3.13 vs. Fig. 3.1) the y-advective effect tends to reduce the eastward displacement during the first 13 hours of integration (~50 km difference for the 10 g kg^{-1} isopleth) and to increase the westward return at night when the LLJ is at its maximum strength. These can be well explained by the enhancement of the northward moisture-advection through the nocturnal development of the southerly LLJ in the eastern half of the domain (Fig. 4.7). The differential movement of the dry line between these two cases would be larger if a greater moisture gradient in the y-direction were specified.

CHAPTER IV

KINEMATIC AND THERMODYNAMIC FIELD VARIABLES IN ASSOCIATION WITH DRY LINE SIMULATIONS

Kinematic Fields; Diurnal Variation

Wind fields

The wind fields are initiated at 0600 LST with a weak jet-like structure similar to that observed. It is known that the formation of the nocturnal low-level jet is related to the inertial modulation of the boundary layer wind in response to the diurnal surface heating. Many previous investigations regarding the LLJ have been conducted (e.g., Blackadar, 1957; Wexler, 1961; Holton, 1967; and Chang, 1976). A detailed discussion of its development is not necessary here. Instead, only dry line-related features will be examined. In these numerical simulations, the formation of the nocturnal LLJ is also well portrayed in the output x-z cross-sections of the component wind fields (Figs. 4.2a-4.2b) and in the diurnal variation of vertical profiles (e.g., Figs. 4.4a-4.4b). Some of the representative wind fields resulting from different simulations will be shown in this chapter. Several significant features in the development of the wind field are noted below.

(i) In response to the heating and cooling at the lower boundary and the turbulent mixing process within the ABL, wind fields exhibit distinct diurnal variations. The easterly (upslope) wind in the lower part of ABL is a result of frictional-stress increases during the convective period; they reach maximum strength around midnight (e.g., Figs. 4.1a-4.1c and Figs. 4.3a-4.3b). This explains part of the nocturnal westward movement of the surface dry line through horizontal advection as described in the previous chapter. Strong vertical shear in the u-component wind developed after sunset and reached its maximum at midnight (Fig. 4.1c); this accounts for the tilt in the vertical profile of the dry line during the nighttime.

(ii) The v-component wind tends to decrease the shear above the jet and to decrease the maximum wind speed during the convective period when vertical mixing is acting (Fig. 4.4a). It forms a distinct LLJ during the nocturnal hours (Fig. 4.4b). A maximum wind speed (~11.5 m s^{-1} for Case A_1) in the jet-core is achieved super-geostrophically around 400 m at 0200 LST. This configuration is significant in the northward transport of heat and moisture (Case I).

(iii) The position of the jet-core also exhibits some diurnal tendency - a little eastward displacement during the daytime and a westward shift of position with a broadening of the core area in the horizontal extent during the nighttime.

As mentioned earlier this movement tendency is not as prominent as that of the dry line.

(iv) Inhomogeneous distribution of thermal forcing at the surface (Case H) causes a westward shift of the jet and also an increase of the maximum wind speed (e.g., Fig. 4.6 vs. Fig. 4.2b). The development of a stronger easterly wind (e.g., Fig. 4.5 vs. Fig. 4.1c) explains the differential nocturnal displacement of the dry line between these two cases (Chapter III).

(v) Inclusion of northward temperature advection (Case I) tends to cause an eastward shift of the LLJ. Displacement of the jet core (shift of over 100 km as can be seen in Fig. 4.7 and Fig. 4.2b) also causes changes in the divergence field as will be seen later. The maximum wind speed in the LLJ is also increased in this case.

(vi) With the same initial wind, the ABL wind-field development in the case of level terrain (Figs. 4.8-4.9) is much weaker compared to that with sloping terrain (this is consistent with Chang's study, 1976). The weaker nocturnal boundary layer wind (Fig. 4.8) results in a negligible nocturnal movement of the dry line as is seen in Case E.

(vii) Expectedly, the effect of an easterly geostrophic wind as specified in Case G tends to force the jet to shift to the west (~40 km, Fig. 4.11). Also stronger low-level easterly winds develop (Fig. 4.10) and hence a greater nocturnal return of the dry line results.

<u>Divergence field and vertical motion</u>

It is known that a zone of horizontal velocity convergence is often associated with the dry line environment as was noted by Rhea (1966). A line of streamline confluence is usually found to the west of the surface dry line (e.g., Matteson, 1969). Since this surface convergence and the consequent vertical motion can provide the lifting necessary for the release of pre-existing potential instability, it provides an important signature for locale favorable for the development of mesoscale convective systems. In this 2-D model, kinematically computed horizontal divergence $\frac{\partial u}{\partial x}$ and vertical motion w will be used in the diagnosis of the pre-storm environment.

The development of boundary-layer wind divergence and vertical motion in conjunction with LLJ phenomena over a heated sloping terrain has been discussed by Chang (1976) through buoyant Ekman-layer theory. Here, selected x-z cross-sectional fields of divergence and vertical motion relating to this dryline experiment are presented.

While only weak upward motion is present in association with the low-level convergence during the daytime period, a gradual intensification of the convergence field and vertical motion occurs after 2000 LST (Figs. 4.12-4.13); this is closely related to the strengthening of the ABL winds. A nocturnal upward-downward vertical motion doublet is developed at a height of 0.5 km up to 2 km after 2000 LST and it continues to intensify throughout the night. The maxima of upward motion and downward motion are separated by approximately 60 km (Fig. 4.13a). A similar upper-air updraft-downdraft doublet is also noted in Sanders and Paine's (1975) analysis of a convective mesostorm in Oklahoma. With surface differential heating (Case H) or with thermal advection in the y-direction (Case I), the vertical circulation pattern is similar but it is more intense (e.g., Figs. 4.14-4.16). It is of some interest to note that in Case I, the vertical motion doublet tends to be decoupled after midnight with stronger ascending motion near the center of the domain (Fig. 4.16a), indicating favorable conditions for convective activity in proximity to the dry line. In the flat terrain simulation (Case E), the intensity of the vertical circulation is greatly reduced.

Although this is a shallow numerical model, the configuration of the field of vertical motion and the associated divergence field suggests that this could contribute to the development of mesoscale convective systems.

Thermodynamic Field Variables in the Simulative Dry Line Environment

Potential temperature

Figs. 4.17 and 4.18 show typical potential temperature fields at two different times. The diurnal evolution of the thermal boundary layer is best shown by the profiles of potential temperature (Fig. 4.20). The thermally mixed ABL is marked by a nearly adiabatic lapse rate below the inversion. Its continuous growth in response to surface heating is shown in Fig. 4.20a. During the surface cooling period, while the potential temperature in the lower ABL decreases and forms a stable layer, temperature in the upper ABL increases slightly. Thus, the nocturnal boundary layer is stabilized (Fig. 4.20b). It is also noted that in Case H (Fig. 4.19) variations in the height of the mixing layer develops across the horizontal domain in response to differential surface heating. This inhomogeneity in the height of the ABL is also reflected in fields of moisture variables.

Moisture variables

All of the moisture-related thermodynamic computations can be found in Appendix D. Examples of the computed values of specific humidity, dew-point temperature, and relative humidity are shown in Figs. 4.21-4.23. The top of the moist mixing layer is well defined in these cross sections. It is marked by a sharp gradient in these moisture variables as is indicated by the concentration of isopleths. The specific humidity fields are comparable to observed moisture fields such as presented by Ogura and Chen (1976) in their mesoscale analysis of data from the NSSL mesonetwork.

The evolution of the moist boundary layer can be compared to that of the thermal ABL by analysis of the time variation of vertical profiles of meteorological variables. Figs. 4.25 and 4.26 provide such a comparison at the grid point i = 20 in the eastern moist region. While the height of the thermal boundary layer is defined by the height of the inversion, the top of the moist mixing layer is usually defined as that level where a sharp decrease in the specific humidity occurs. As expected from the similarity in our formulation of the thermal and moist mixing processes, we note from the profiles that the depth of the moist mixing layer increases at about the same rate as the thermal ABL during the convective period. This differs from the results obtained by Burk (1977) with a one-dimensional higher-order model, where the thermal ABL grows somewhat higher than the moist mixing layer.

In an attempt to study the diurnal changes of potential instability due to the redistribution of thermodynamic quantities, cross-sections of wet-bulb potential temperature were constructed. Examination of these fields reveals several interesting features.

(i) Generally, in the dry line environment a potentially unstable layer exists in the moist ABL located in the eastern domain while a stable layer is present to the west and above the moist ABL. A transitional region exists in the vicinity of surface dry line (Fig. 4.27).

(ii) These regions also exhibit a diurnal movement similar to the dry line. The nocturnal return of the surface dry line usually destabilizes the boundary layer so that it becomes neutral or potentially unstable as can be seen in Fig. 4.28.

(iii) The zero moisture-flux boundary condition (Case A_2) tends to stabilize the potential instability in the ABL, since there is no source of moisture in the lower layer.

(iv) Differential advection of moisture in the nocturnal dry line environment (easterly in low levels and westerly above) enhances the potential instability and hence increases the possibility of intense moist convection.

Moisture-convergence fields

It is worthwhile to examine the moisture-divergence fields in the dry line environment. The expression for moisture divergence may be expressed as two terms - the velocity-divergence term and the moisture-advection term; i.e.,

$$\nabla \cdot q\vec{V} = q\nabla \cdot \vec{V} + \vec{V} \cdot \nabla q \ .$$

The first term is larger when moisture gradients are relatively weak; in that case the moisture-divergence field will resemble the velocity divergence field.

Hylton and Sasaki (1973) found that in many cases radar echoes develop in regions characterized by surface moisture convergence. They found that strong moisture convergence [$2 - 8 \times 10^{-4}$ g kg^{-1} sec^{-1}] existed prior to the occurrence of strong convection. The computed moisture-divergence fields in this numerical simulation are comparable to those they obtained in their analyses, both in horizontal extent and in magnitude (Figs. 4.29 and 4.30 vs. Fig. 4.31). Since the moisture field usually becomes diffuse during the night, the moisture-divergence pattern is similar to the wind-divergence field during the nocturnal period. Moisture convergence, like surface wind velocity convergence, provides conditions favorable to the onset of moist convection.

The Evolving Mixing Layer Versus the Lifting Condensation Level (LCL)

Eq. (2.5), which describes the growth of the convective boundary layer depth in response to surface heat-flux and other processes mentioned in Chapter II, yields reasonable results as is seen in the evolution of the potential temperature and specific-humidity profiles (Figs. 4.25 and 4.26). In addition to an examination of changes of potential instability in the dry line environment, it is also interesting to compare the evolving ABL height with the lifting condensation level of the near-surface air. Formation of cumulus clouds is possible whenever the depth of the mixing layer exceeds the height of the LCL. Typical diurnal variations of the ABL depth and the LCL in the numerical simulations are shown in Figs. 4.32a-4.32c for three different grid points ($i = 6$, 13, and 20) representing locations with different moisture conditions. It is immediately apparent that in the western dry region (i = 6) the LCL is always above the mixing layer, except in Case H (not shown here) where the ABL height reaches the LCL (~3 km above ground) shortly after 1700 LST. Thus, formation of cumulus clouds by the eddy-mixing process within the ABL is not possible unless other mechanical lifting exists. While condensation could occur shortly after 1200 LST at the middle grid point, the ABL will exceed the height of the LCL as early as 0900 LST in the eastern moist region (i = 20). A similar situation exists in Case A_2 but the LCL is higher when there is no vertical moisture flux at the lower boundary.

A 48 Hour Integration

In order to further examine the evolution of various fields, the model is integrated through the second diurnal cycle for the control Case A_1. Due to mixing processes and the outflow boundary conditions the moisture content is greatly reduced in the domain at the end of the first diurnal cycle. Since the specific humidity is not coupled with other prognostic variables in this model, the specific humidity field is reinitiated (Fig. 3.15) at the beginning of the second day of the integration. None of the remaining fields are altered. Generally speaking, most of the fields show the same diurnal tendency as in the first day of the simulation. Some minor differences will be discussed.

(i) The diurnal movement of the dry line is similar to that determined for the first day. As in Case F, specification of a deeper moist layer greatly reduces the movement of the dry line.

(ii) Because of the processes occurring in the thermally well-mixed ABL during the first day, the potential temperature field for the second day is marked by a secondary inversion; thus, two mixing layers exist as can be seen in Fig. 4.33.

(iii) The development of the ABL wind field (LLJ and easterly wind) during the second diurnal cycle is similar to that of the first day. While the divergence and vertical motion patterns resemble those of the first day, they are more intense and exist through a deeper layer (e.g., Fig. 4.34 vs. Fig. 4.13).

(iv) As a result of a smaller super-adiabatic lapse rate in the surface layer and the consequent smaller surface heat-flux (Fig. 4.35), the depth of the ABL is less than that of the first day during the heating period.

Maintenance of the Sharp Moisture Gradient

It is necessary, at this point, to focus our investigation on the maintenance of the sharpness of the moisture gradient in the dry line environment. We have ignored this aspect in the analyses described in Chapter III where the horizontal mixing process usually leads to a spreading of the isopleths of specific humidity. In examining the surface wind field in the dry line environment as described in the introduction (Fig. 1.1), we have noticed the convergence zone associated with the confluent flow near the dry line. Sharpening of the moisture gradient brought about by the horizontal advection process is demonstrated in Case D. This enables us to relate the observed sharp moisture gradient in the dry line environment to the kinematic deformation in the horizontal wind fields; i.e., the confluence of the westerly/ southwesterly flow and the southerly LLJ. In an attempt to better portray the observed wind fields and the maintenance of the sharp moisture gradient during the course of the dry line movement, two simulations are carried out.

(i) Case J_1. Realizing that the configuration of the wind field (Fig. 1.1) is also controlled by the large-scale (synoptic) pressure field, it is logical to impose a north-south pressure gradient so that the westerly flow can be maintained west of the dry line during its eastward movement. Therefore, a stronger westerly geostrophic wind $u_g = 5\ m\ s^{-1}$ is used in this experiment. A LLJ with stronger winds is also specified, while the initial moisture field is the same as shown in Fig. 3.15. The evolution of the dry line is described in the time-section shown in Fig. 4.36. Note that the initial moisture gradient is maintained fairly well as the dry line moves to the east. The wind fields are similar to those in Fig. 1.1 as can be seen by superimposing the u-component wind fields (Fig. 4.37a) and the v-component wind fields (Fig. 4.37b). A greater influence of the geostrophic wind on the dry line motion is also noted by comparing Fig. 4.36 with Fig. 3.10 (weaker geostrophic forcing).

(ii) Case J_2. As indicated in Case I, northward fluxes of moisture and temperature exert profound influence on the evolution of the dry line environment. One would expect that the north-south moisture advection brought about by the LLJ should share a significant role in the maintenance of the moisture gradient in the vicinity of the dry line. To support our assertion, north-south advective terms similar to those of Case I are incorporated in addition to the initial conditions specified in Case J_1 (except here a stronger moisture gradient $\frac{\partial q}{\partial y} = -1$ g kg^{-1}/100 km is used). Fig. 4.38 shows the moisture time-section for this experiment. It is apparent that considerable sharpening of the moisture gradient results because of inclusion of strong moisture advection in the y direction. The position of the maximum in the specific humidity field is well correlated with the position of the LLJ; also, the region of maximum horizontal convergence coincides with the region of sharp moisture gradient.

Although a precise simulation of the horizontal wind deformation and the y-direction advection would require utilization of a three-dimensional dry-line model, these simplified experiments do provide a sound qualitative description of the mechanisms responsible for the maintenance of the sharp moisture gradient in the dry line environment.

CHAPTER V

CONCLUSIONS AND SUGGESTIONS FOR FUTURE RESEARCH

Concluding Remarks

The 2-D mesoscale boundary layer model designed with a stretched horizontal coordinate system and with an improved ABL parameterization including a suitable inversion-rise formalism is used to study the evolution of the dry line environment. Several relevant physical processes are included and tested in the numerical simulations; major findings are discussed below.

The observed diurnal motion of a typical dry line, i.e., eastward movement during the daytime and westward displacement during the nighttime, is well simulated by the numerical model. With an initial wind field similar to that observed, i.e., a weak LLJ and a constant westerly geostrophic wind (e.g., control Case I), we are able to simulate the dry line movement. The dominant process responsible for daytime displacement is found to be the vertical mixing activated when the height of the ABL (height of the inversion) grows above the top of the dry line as is shown in Fig. 5.1. Other processes such as horizontal mixing and advection are only of secondary importance in describing the motion of the dry line during the convective period. During the nocturnal period when the mixing process is inactive, westward displacement of the surface dry line (in our simulation) is due to advection as up-slope easterly winds develop in the lower ABL and horizontal mixing which leads to westward spreading of isopleths of specific humidity (e.g., Case C). Shaefer (1974) arrived at the same conclusion that vertical mixing is primarily responsible for the eastward movement of the dry line during the daytime. However, the nocturnal return of the surface dry line does not occur in his model simulations. This may happen because of the different ABL parameterization and the improper assignment of a fixed ABL height which may not allow a faithful depiction of the structure of the thermal field and the wind field within the ABL. Another possibility is excessive westerly geostrophic forcing which may prevent westward displacement during the nighttime.

The speed and extent of the dry line displacement is found to be dictated by a number of other factors. As discussed in Chapter III, the depth of the dry line, the strength of the surface moisture flux, the inhomogeneities in the surface thermal and moist forcing, the effect of north-south advection by the LLJ, and large scale synoptic conditions (e.g., Case J_1) all impose constraints on the movement of the dry line. Although an exact quantitative evaluation of these effects would require detailed modeling of these mechanisms, a reasonable qualitative diagnosis of these effects has been achieved on the basis of the simulations completed in this study.

Although it has been noted that the dry line may become diffuse as it moves eastward, the simulations also indicate that within the ABL the horizontal advection process alone is sufficient to build up a sharp moisture gradient in the region west of the nocturnal low-level jet (e.g., Case D). Northward moisture advection (e.g., Case J_2) also is responsible for the maintenance of a sharp moisture gradient since the LLJ can advect abundant moisture within the ABL. The horizontal wind field shown in Fig. 1.1 also indicates the important role that horizontal advection can have in the maintenance of the moisture gradient. While the westerly/southwesterly winds west of the dry line advect dry air toward the dry line, the southerly winds east of the dry line bring in warm moist air; thus, the moisture contrast is maintained and perhaps enhanced by the confluent flow.

As shown in these simulations, characteristics of the wind field and thermodynamic variables in the dry line environment exhibit diurnal variations. The formation of the nocturnal southerly LLJ and the easterly wind within the ABL play a significant role in the nocturnal evolution of the dry line through the advective process. Low-level wind velocity convergence which develops in close proximity to the dry line in the late afternoon strengthens throughout the nighttime. The divergence fields are distributed such that a mesoscale vertical motion doublet is formed. In some experiments carried out with favorable conditions (i.e., differential heating and thermal advection) the upward vertical motion exhibits significant intensification through midnight. This suggests the possibility of triggering of pre-existing potential instability and further development of a mesoscale convective system. These kinematic fields together with the corresponding moisture-divergence field in the simulated dry line environment resembles the results obtained from an objective analysis of a pre-storm environment in the NSSL mesonetwork (e.g., Hilton and Sasaki, 1973; Ogura and Chen, 1977). Thus, our simulations suggest that the dry line environment does provide favorable conditions for the development of mesoscale convective systems.

Future Research

Even though this two-dimensional model cannot depict effects of inhomogeneities in the y-direction (e.g., bulges of the dry line), it does reveal some of the important features imbedded in a dry line environment and some of the basic physical processes responsible for the diurnal variation. For a continuing effort toward the investigation of dry line related initiation of moist convection, one can go well beyond this relatively simple model. The vertical domain can be extended higher to include deep convection. One also needs to include other relevant physical processes such as cumulus convection and micro-physical processes where phase changes of water substance are allowed and where thermal and moisture fields are coupled. Physically sound parameterization schemes for these processes can be incorporated in the meso-boundary layer model to study the interaction between the ABL and the free atmosphere so that the role of the dry line environment in the initiation of moist convection can be further examined.

Other problems which need to be investigated are listed below.

(1) As indicated in this study, the depth of the moist layer in the eastern portion of the domain exerts a constraint on the movement of the dry line and also affects the subsequent configuration of thermodynamic fields. Thus, monitoring the height of the moist mixing layer is as important as observing the height of the heated boundary layer to the west of the dry line. The uneven development of the ABL height in the vicinity of the dry line should be realistically modeled in order to understand the dynamics of the observed thermal and momentum fields in the dry line environment.

(2) Prediction of dry line movement requires realistic formulations of various influential conditions in the boundary layer such as those revealed in this study. Horizontal

inhomogeneities in the surface moisture flux, differential heating at the lower boundary, north-south advection of moisture and heat, three-dimensional subgrid scale fluxes, deformation in the horizontal wind field, and the large-scale synoptic conditions all are significant in the diurnal evolution of the dry line. Furthermore, since the height of the convective ABL to the west of the dry line can grow to high levels, downward transport of westerly momentum is possible through the vertical mixing process; this may contribute to intensification of low-level convergence. Therefore, faithful three-dimensional representation of these processes is necessary in order to develop a full understanding of the dry line and associated phenomena.

REFERENCES

Ball, F. K., 1960: Control of inversion height by surface heating. Quart. J. Roy. Soc., 86, 983-994.

Barr, S., and C. W. Kreitzberg, 1975: Horizontal variability and boundary-layer modelling. Boundary-layer Meteor., 8, 163-172.

Blackadar, A. K., 1957: Boundary layer wind maxima and their significance for the growth of nocturnal inversions. Bul. Amer. Meteor. Soc., 38, 283-290.

Burk, S. D., 1977: The moist boundary layer with a higher order turbulence closure model. J. Atmos. Sci., 34, 629-638.

Businger, J. A., 1973: Turbulent transfer in the atmospheric surface layer. Workshop in Micrometeor., Amer. Meteor. Soc., Boston, Chap. 2.

______, and S. P. S. Arya, 1974: Height of mixed layer in the stably stratified planetary boundary layer. Advances in Geophys., Vol. 18A, 73-92.

Carson, D. J., 1973: The development of a dry inversion-capped convectively unstable boundary layer. Quart. J. Roy. Meteor. Soc., 99, 450-467.

Chang, L. W., 1976: A numerical study of the diurnal variation of the low-level jet. Ph.D. Thesis, University of Oklahoma, Norman, Oklahoma, 110 pp.

Deardorff, J. W., 1972: Numerical investigation of neutral and unstable planetary boundary layers. J. Atmos. Sci., 29, 91-115.

______, 1974: Three-dimensional numerical study of the height and mean structure of a heated planetary boundary layer. Boundary-layer Meteor., 7, 81-106.

Estoque, M.A., 1963: A numerical model of the atmospheric boundary layer. J. Geophys. Res., 68, 1103-1113.

Fujita, T. T., 1958: Structure and movement of a dry front. Bul. Amer. Meteor. Soc., 39, 574-582.

Haltiner, G. J., 1971: Numerical Weather Prediction. John Wiley and Sons, Inc., New York, 317 pp.

Holton, J. R., 1967: The diurnal boundary layer wind oscillation above sloping terrain. Tellus, 19, 2, 199-205.

Hylton, D. A., and Y. Sasaki, 1973: Analysis of surface and upper air wind fields using variational low-pass and band-pass filtering technique. Atmospheric Research Laboratory, WEAT Rept. 8, Norman, Oklahoma, 91 pp.

Inman, R. L., 1969: Computation of temperature at the lifted condensation level. J. Appl. Meteor., 8, 155-158.

Iribarne, J. V., and W. L. Godson, 1973: Atmospheric Thermodynamics. Reidel Publishing Company, 222 pp.

Klemp, J. B., and D. K. Lilly, 1978: Numerical simulation of hydrostatic mountain waves. J. Atmos. Sci., 35, 78-107.

______, and R. B. Wilhelmson, 1978: The simulation of three-dimensional convective storm dynamics. J. Atmos. Sci., 35, 1070-1096.

Krishna, K., 1968: A numerical study of the diurnal variations of meteorological parameters in the planetary boundary layer. Mon. Wea. Rev., 96, 269-276.

Leith, C. E., 1968: Diffusion approximation for two-dimensional turbulence. Phys. Fluids, 10, 1417-1423.

______, 1969: Two-dimensional eddy viscosity coefficients. Proc. WMO/IUGG Symp. Numerical Weather Prediction, 26 Nov. - 4 Dec., 1968, Meteor. Soc. Japan, Tokyo, 1-41.

Lilly, D. K., 1965: On the computational stability of numerical solutions of time-dependent non-linear geophysical fluid dynamics problems. Mon. Wea. Rev., 93, 11-26.

______, 1968: Models of cloud-topped mixed layers under a strong inversion. Quart. J. Roy. Meteor. Soc., 94, 292-309.

Mahrer, Y., and R. A. Pielke, 1975: A numerical study of the air flow over mountains using the two-dimensional version of the University of Virginia mesoscale model. J. Atmos. Sci., 32, 2144-2155.

Mahrt, L., 1976: Mixed layer moisture structure. Mon. Wea. Rev., 104, 1403-1407.

______, and D. H. Lenschow, 1976: Growth dynamics of the convectively mixed layer. J. Atmos. Sci., 33, 41-51.

Matsuno, T., 1966: False reflection of waves at the boundary due to the use of finite differences. J. Meteor. Soc. Japan, 44, 145-157.

Matteson, G. T., 1969: The west Texas dry front of June 1967. M.S. Thesis, University of Oklahoma, Norman, Oklahoma, 63 pp.

McGuire, E. L., 1962: The vertical structure of the three drylines as revealed by aircraft traverses. National Severe Storms Project Report, No. 7, NSSL, Norman, Oklahoma, 10 pp.

McPherson, R. D., 1968: A three dimensional numerical study of the Texas coast sea breeze. Atmospheric Science Group, Rept. 15, University of Texas, Austin, Texas, 252 pp.

Means, L. L., 1952: On thunderstorm forecasting in the central United States. Mon. Wea. Rev., 80, 165-189.

Mellor, G. L., 1973: Analytic prediction of the properties of stratified planetary surface layers. J. Atmos. Sci., 30, 1061-1069.

Nitta, T., 1962: The outflow boundary condition in numerical time integration of advective equations. J. Meteor. Soc. Japan, 40, 13-24.

O'Brien, J. J., 1970: A note on the vertical structure of the eddy exchange coefficient in the planetary boundary layer. J. Atmos. Sci., 27, 1213-1215.

Ogura, Y., and Y. Chen, 1977: A life history of an intense mesoscale convective storm in Oklahoma. J. Atmos. Sci., 34, 1458-1476.

Orlanski, I., 1976: A simple boundary condition for unbounded hyperbolic flows. J. Comput. Phys., 21, 251-269.

Phillips, N. A., 1956: The general circulation of the atmosphere, a numerical experiment. Quart. J. Roy Meteor. Soc., 82, 123-164.

Pielke, R. A., 1974a: A three-dimensional numerical model of the sea breezes. Mon. Wea. Rev., 102, 115-139.

______, 1974b: A comparison of three-dimensional and two-dimensional numerical predictions of sea breezes. J. Atmos. Sci., 31, 1577-1585.

______, and Y. Mahrer, 1975: Representation of the heated planetary boundary layer in mesoscale models with coarse vertical resolution. J. Atmos. Sci., 32, 2288-2308.

Pitchford, K. L., and J. London, 1962: The low-level jet as related to nocturnal thunderstorms over Midwest United States. J. Appl. Meteor., 1, 43-47.

Rhea, J. O., 1966: A study of thunderstorm formation along dry lines. J. Appl. Meteor., 5, 58-63.

Robert, A. J., F. G. Schuman and J. P. Gerrity, Jr., 1970: On partial difference equations in mathematical physics. Mon. Wea. Rev., 98, 1-6.

______, 1966: The integration of a low order spectral form of the primitive meteorological equations. J. Meteor. Soc. Japan, 44, 237-245.

Sanders, F., and R. J. Paine, 1975: The structure and thermodynamics of an intense mesoscale convective storm in Oklahoma. J. Atmos. Sci., 32, 1563-1579.

Schaefer, J. T., 1973: The motion and morphology of the dry line. NOAA Tech. Memo. ERL NSSL-66, Norman, Oklahoma, 81 pp.

______, 1974a: The life cycle of the dry line. J. Appl. Meteor., 13, 444-449.

______, 1974b: A simulative model of the dry line motion. J. Atmos. Sci., 31, 956-964.

______, 1976: Moisture features of the convective layer in Oklahoma. Quart. J. Roy. Meteor. Soc., 102, 447-451.

Stull, R. B., 1976: The energetics of entrainment across a density interface. J. Atmos. Sci., 33, 1260-1267.

Taylor, P. A., 1977: Numerical study of neutrally stratified planetary boundary layer flow above gentle topography. Boundary-layer Meteor., 12, 1, 37-60.

Tennekes, H., 1973: A model for the dynamics of the inversion above a convective boundary layer. J. Atmos. Sci., 30, 558-567.

Tetens, O., 1930: Über einige meteorologiche Begriffe. Zeitsch. für Geophys., 6, 297-309.

Wallace, J. M., 1975: Diurnal variations in precipitation and thunderstorm frequency over the conterminous United States. Mon. Wea. Rev., 103, 406-419.

Weston, K. J., 1972: The dry line of Northern India and its role in cumulonimbus convection. Quart. J. Roy. Meteor. Soc., 98, 519-531.

Wexler, H., 1961: A boundary layer interpretation of the low-level jet. Tellus, 13, 3, 368-378.

Wyngaard, J. C., 1975: Modelling the planetary boundary layer - extension to the stable case. Boundary-layer Meteor., 9, 441-460.

Zeman, O., and H. Tennekes, 1977: Parameterization of the turbulent energy budget at the top of the daytime atmospheric boundary layer. J. Atmos. Sci., 34, 111-123.

Zilitinkevich, S. S., 1972: On the determination of the height of Ekman Boundary Layer. Boundary-layer Meteor., 3, 141-145.

______, 1975: Comments on "A model for the dynamics of the inversion above a convective boundary layer." J. Atmos. Sci., 32, 991-992.

APPENDIX A

COMPUTATION OF VERTICAL EDDY EXCHANGE COEFFICIENTS IN THE ATMOSPHERIC BOUNDARY LAYER

Surface Layer Computation

In the surface layer, the most commonly used empirical non-dimensional profile functions (Businger, 1973) for momentum, heat, and moisture, respectively are:

$$\varphi_{(m)}(\hat{\zeta}) = \begin{cases} (1 - 15\hat{\zeta})^{-\frac{1}{4}} & , \quad \hat{\zeta} \leq 0 \\ 1 + 4.7\hat{\zeta} & , \quad \hat{\zeta} > 0 \end{cases} \tag{A.1}$$

$$\varphi_{(H)}(\hat{\zeta}) = \varphi_{(q)}(\hat{\zeta}) = \begin{cases} 0.74(1 - 9\hat{\zeta})^{-\frac{1}{2}} & , \quad \hat{\zeta} \leq 0 \\ 0.74 + 4.7\hat{\zeta} & , \quad \hat{\zeta} > 0 \end{cases} \tag{A.2}$$

where $\varphi_{(m)}(\hat{\zeta}) = \frac{k\hat{z}}{u_*}\frac{\partial u}{\partial \hat{z}}$, $\varphi_{(H)}(\hat{\zeta}) = \frac{k\hat{z}}{\theta_*}\frac{\partial \theta}{\partial \hat{z}}$ and $\varphi_{(q)}(\hat{\zeta}) = \frac{k\hat{z}}{q_*}\frac{\partial q}{\partial \hat{z}}$.

The non-dimensional stability parameter $\hat{\zeta} = \hat{z}/L$ and the Monin-Obukhov length $L = u_*^2/k\,\beta\,\theta_*$ will have the same sign corresponding to different thermal stratifications.

In order to obtain u_*, θ_* and q_*, we integrate (A.1) and (A.2) from z_o to a certain height $\hat{z}$ within the surface layer. Thus, the integrated versions of the profiles are:

$$u = \frac{u_*}{k}[\ln \frac{\hat{z}}{z_o} - \psi_1(\hat{\zeta})] \tag{A.3}$$

$$\theta - \theta_s = \frac{0.74\,\theta_*}{k}[\ln \frac{\hat{z}}{z_o} - \psi_2(\hat{\zeta})] \tag{A.4}$$

$$q - q_s = \frac{0.74\,q_*}{k}[\ln \frac{\hat{z}}{z_o} - \psi_2(\hat{\zeta})] \tag{A.5}$$

where

$$\psi_1(\hat{\zeta}) = \begin{cases} 2\ln[\frac{(1+\alpha)}{2}] + \ln[\frac{(1+\alpha^2)}{2}] - 2\tan^{-1}\alpha + \frac{\pi}{2}\,, & \hat{\zeta} \le 0 \\ -\,4.7\hat{\zeta} & , \hat{\zeta} > 0 \end{cases} \tag{A.6}$$

and

$$\alpha = \varphi^{-1}_{(m)} = (1 - 15\hat{\zeta})^{1/4}\,, \text{ and}$$

$$\psi_2(\hat{\zeta}) = \begin{cases} \ln[\frac{1+\gamma}{2}]^2 & , \quad \hat{\zeta} \le 0 \\ -4.7\hat{\zeta}/0.74 \,, & \hat{\zeta} > 0 \end{cases} \tag{A.7}$$

with $\gamma = 0.74\,\varphi^{-1}_{(H)} = (1 - 9\hat{\zeta})^{1/2}$.

In (A.3) to (A.5), we simply approximate u, θ and q at z_o by their surface values. Also, note that for neutral stratification ($\hat{\zeta} = 0$), we have $\psi_1 = \psi_2 = 0$. One can obtain u_*, θ_* and q_* by using one of the following three options:

(a) From the definition of the gradient Richardson number and the non-dimensional profile functions, we have

$$R_i = \frac{\varphi_{(H)}}{\varphi^2_{(m)}}\,\hat{\zeta}\,. \tag{A.8}$$

One can approximate R_i by the bulk Richardson number using information at two levels, i.e.,

$$R_{i_B} = \beta(\theta_2 - \theta_1)\,\frac{\sqrt{\hat{z}_1\hat{z}_2}\,\ln\frac{\hat{z}_2}{\hat{z}_1}}{(u_2 - u_1)^2}\,.$$

Then solve (A.8) for $\hat{\zeta}$ by iteration. After $\hat{\zeta}$, u, θ and q are known at two levels, one can determine u_*, θ_* and q_* through the integrated equations (A.3) to (A.5).

(b) If data are available at several different levels in the surface layer, one can first determine u_*, θ_* and q_* from the neutrally stratified versions of (A.3) to (A.5) by least-square fitting of the data; then compute ψ_1 and ψ_2 using (A.6) and (A.7) according to the stratifications. Thereafter re-fit the data using (A.3) to (A.5) to obtain the corrected values for u_*, θ_* and q_*. Repeat this successive correction procedure several times to get the final values of u_*, θ_* and q_*.

(c) A non-iterative method using two-level ($\hat{z}_1$, $\hat{z}_2$) information is to make use of the definition of the Monin-Obukhov length (L) and the bulk Richardson number (R_{i_B}) in the integrated profile functions. Thus, one can obtain $(\hat{z}_2 - \hat{z}_2)/L$ (stable/neutral case) in terms of $\hat{z}_1/\hat{z}_2$ and R_{i_B} by solving a quadratic equation in $(\hat{z}_2 - \hat{z}_1)/L$; or express $\frac{z_2}{L}$ (unstable case) as a polynominal in terms of z_2/z_1 and R_{i_B}. After L is determined, u_*, θ_* and q_* can be determined from the integrated profile functions.

Once all the characteristic quantities u_*, θ_* and q_* are obtained, the vertical eddy coefficients are computed through the hypothesized flux-gradient relation, i.e.,

$$K_z^{(\eta)} = k \frac{u_* \hat{z}}{\varphi_{(\eta)}(\zeta)} , \qquad \text{(A.9)}$$

where η is momentum, heat, or moisture. In this numerical study, the non-iterative strategy (c) is used because the required computer time is less.

Turning Layer Computations

The proper technique for specifying eddy exchange coefficients in the Ekman layer is generally not as clear as in the surface layer where similarity theory is well justified. Different profiles have been used in numerical studies. The most satisfactory profile function is due to O'Brien (1970). The interpolating Hermite polynominal is determined with the given conditions - the height of ABL ($\hat{z}_i$) and surface layer ($\hat{z}_h$), the values of eddy coefficients and their slopes at $\hat{z}_i$ and $\hat{z}_h$. The resulting cubic polynomial is:

$$K(\hat{z}) = K_i + [(\hat{z} - \hat{z}_i)^2/(\hat{z}_i - \hat{z}_h)^2] \times$$

$$\{K_h - K_i + (\hat{z} - \hat{z}_h)[K_h' + 2(K_h - K_i)/(\hat{z}_i - \hat{z}_h)]\}, \qquad \text{(A.10)}$$

where $K_i = K(\hat{z}_i)$, $K_h = K(\hat{z}_h)$ with $K_h' = K'(\hat{z}_h)$ and $K'(\hat{z}_i) = 0$.

APPENDIX B

LINEAR MODEL ANALYSIS

For a diagnostic analysis of atmospheric waves inherent in this model, a set of linearized perturbation equations can be derived from the governing equations. With the basic state in hydrostatic and geostrophic balance, the simplified perturbation equations are:

$$\frac{\partial u'}{\partial t} = f\,v' - \bar{\theta}\,\frac{\partial \pi'}{\partial x} + \frac{\theta'}{\bar{\theta}}\,g\,z'_G \,, \tag{B.1}$$

$$\frac{\partial v'}{\partial t} = -f\,u' \,, \tag{B.2}$$

$$\frac{\partial \theta'}{\partial t} + w'S = 0 \,, \tag{B.3}$$

$$\frac{\partial u'}{\partial x} + \frac{\partial w'}{\partial \hat{z}} = 0 \,, \tag{B.4}$$

$$\frac{\partial \pi'}{\partial \hat{z}} = g\,\frac{\theta'}{\bar{\theta}^2} \,, \tag{B.5}$$

where $S = \frac{\partial \bar{\theta}}{\partial \hat{z}}$; the Boussinesq approximation is used for the buoyancy term.

For convenience, we rewrite (B.1) to (B.5) by denoting $\frac{g}{\bar{\theta}} = \beta$, $\bar{\theta}\,\pi' = \hat{\pi}$ and $z'_G = m$. Thus,

$$\frac{\partial u'}{\partial t} - f\,v' + \frac{\partial \hat{\pi}}{\partial x} - \beta\, m\, \theta' = 0 \,, \qquad \text{(B.6)}$$

$$\frac{\partial v'}{\partial t} + f\,u' = 0 \,, \qquad \text{(B.7)}$$

$$\frac{\partial \theta'}{\partial t} + w' S = 0 \,, \qquad \text{(B.8)}$$

$$\frac{\partial u'}{\partial x} + \frac{\partial w'}{\partial \hat{z}} = 0 \,, \qquad \text{(B.9)}$$

$$\frac{\partial \pi'}{\partial \hat{z}} - \beta\,\theta' = 0 \,. \qquad \text{(B.10)}$$

Seeking the normal mode solutions

$$\begin{pmatrix} u' \\ v' \\ w' \\ \theta' \\ \hat{\pi} \end{pmatrix} = \begin{pmatrix} U \\ V \\ W \\ \Theta \\ \pi \end{pmatrix} e^{i(\mu x + k \hat{z} - \nu t)}$$

requires that

$$\begin{vmatrix} -i\nu & -f & 0 & -\beta m & i\mu \\ f & -i\nu & 0 & 0 & 0 \\ 0 & 0 & S & -i\nu & 0 \\ i\mu & 0 & ik & 0 & 0 \\ 0 & 0 & 0 & -\beta & ik \end{vmatrix} = 0 \,.$$

Whence, after discarding the root $\nu = 0$ as a trivial solution, the following dispersion relation is determined.

$$\nu = \pm\left[f^2 + \frac{N^2 \mu(\mu - m\,k)}{k^2} \right]^{\frac{1}{2}} , \qquad \text{(B.11)}$$

where $N^2 = \beta S$ is the square of the Brunt-Väisälä frequency. Thus, as indicated in (B.11), the dominant wave disturbances in this model are the inertial-gravitational oscillations.

For an estimation of the possible maximum phase speed, assume

$$f^2 \sim .696 \times 10^{-8} \text{ sec}^{-2} ,$$

$$N^2 \sim 10^{-4} \text{ sec}^{-2} ,$$

$$\mu_{min} = \frac{2\pi}{L} \sim 4.23 \times 10^{-6} \text{ m}^{-1} ,$$

$$k_{min} = \frac{\pi}{2H} \sim 3.40 \times 10^{-4} \text{ m}^{-1} ,$$

$$m \sim -1/600 :$$

then the maximum horizontal phase speed is

$$|c_x| = \left|\frac{\nu}{\mu}\right| \sim 37 \text{ m s}^{-1} ,$$

and the corresponding vertical phase speed is

$$|c_z| = \left|\frac{\nu}{k}\right| \sim 0.5 \text{ m s}^{-1} .$$

APPENDIX C

FORMULATION OF LATERAL BOUNDARY CONDITIONS

The type of lateral boundary condition used in this limited-domain integration is the Somerfeld radiation condition in which wave disturbances are allowed to be transmitted at the outflow boundary. The condition simply is

$$\frac{\partial \varphi}{\partial t} + c_x \frac{\partial \varphi}{\partial x} = 0 \ , \qquad (C.1)$$

with φ being the prognostic variable and c_x the horizontal phase speed of the wave disturbance.

In application of (C.1), it is necessary to determine a suitable phase speed c_x. The formulation used here was proposed by Orlanski (1976); it has been shown to be successful in controlling the instability arising from false reflections at the boundary. The phase speed is computed at each point along the boundaries. For instance, for grid points at the eastern boundary, one can approximate (C.1) by leap-frog differencing:

$$\frac{\varphi_N^t - \varphi_N^{t-2}}{2\Delta t} = - \frac{c_x}{\Delta x}\left[\frac{\varphi_N^t + \varphi_N^{t-2}}{2} - \varphi_{N-1}^{t-1}\right] \ , \qquad (C.2)$$

where the space differencing is centered at a point one-half grid interval from the boundary; this is consistent with the space-derivative scheme used at interior grid points. Due to the time-splitting character of the leap-frog scheme (Chapter II), the first term on the right-hand side of (C.2) is used to control the same numerical modes as those in the time derivatives, so that mixing of modes and strong reflections at the boundary are avoided. Thus, the phase speed computed from (C.2) is

$$c_x = - \frac{[\varphi_{N-1}^{t} - \varphi_{N-1}^{t-2}]}{[\varphi_{N-1}^{t} + \varphi_{N-1}^{t-2} - 2\,\varphi_{N-2}^{t-1}]} \frac{\Delta x}{\Delta t} \,. \tag{C.3}$$

Rewriting (C.2) by advancing one time level, we obtain the boundary condition:

$$\varphi_N^{t+1} = \frac{[1 - (\frac{\Delta t}{\Delta x}) c_x]}{[1 + (\frac{\Delta t}{\Delta x}) c_x]} \varphi_N^{t-1} + \frac{[2(\frac{\Delta t}{\Delta x}) c_x]}{[1 + (\frac{\Delta t}{\Delta x}) c_x]} \varphi_{N-1}^{t} \,. \tag{C.4}$$

(C.4) is used when the computed phase speed satisfies $0 \leq c_x \leq \frac{\Delta x}{\Delta t}$ as is also required by the Courant-Friedrichs-Lewy stability criterion.

For $c_x > \Delta x/\Delta t$, we set $c_x = \frac{\Delta x}{\Delta t}$ and (C.4) becomes

$$\varphi_N^{t+1} = \varphi_{N-1}^{t} \,. \tag{C.5}$$

If $c_x < 0$, we set $c_x = 0$ and (C.4) requires

$$\varphi_N^{t+1} = \varphi_N^{t-1} \,. \tag{C.6}$$

For grid points at the western boundary, similar procedures are used.

In application of this type of radiation boundary condition, it is also feasible to use a fixed value of c_x; for example, taking $c_x \sim 40$ m s^{-1} as computed in Appendix B; or using the approximation of averaging c_x (C.3) along the boundary. Essentially the same results were obtained in this numerical experiment by using these two alternatives. Successful use of these boundary conditions was also demonstrated by Klemp and Wilhelmson (1978) and by Klemp and Lilly (1978).

Since the condition (C.4) is nonlinear in nature, a theoretical analysis of its reflective characteristics is not possible for the general dispersive case. However, it is a simple matter to prove that for a single wave with constant phase speed, this boundary condition will produce no reflection since the scheme measures the phase speed at time level t-1 and applies it at time level t. Orlanski (1976) has tested this condition under severe conditions and minimal contamination of the flow field was found. In this dry line numerical model, control of the computational reflections by this boundary formulation is also quite satisfactory.

APPENDIX D

THERMODYNAMIC COMPUTATIONS

The moisture-related thermodynamic variables in this numerical study are computed for each grid point according to the following procedures:

<u>Relative Humidity and Dew-point Temperature</u>

(i) The saturated vapor pressure (in millibars) is computed using the empirical Magnus formula (Tetens, 1930):

$$\log_{10} e_s = \frac{7.5\ t}{237.3+t} + 0.7858 \qquad \text{(D.1)}$$

where $t = T - 273.16$, and $T = \frac{\pi\theta}{c_p}$.

(ii) The unsaturated and saturated mixing ratios, and the relative humidity are computed as follows:

$$\omega = \frac{q}{1-q}\ , \qquad \text{(D.2)}$$

$$\omega_s = 0.622\ e_s/(P - e_s)\ , \qquad \text{(D.3)}$$

$$U_w = \frac{\omega}{\omega_s} \times 100\%\ , \qquad \text{(D.4)}$$

where

$$P = 1000\ \left(\frac{\pi}{c_p}\right)^{\frac{c_p}{R_d}} \qquad \text{(D.5)}$$

(iii) The dew-point temperature is obtained through the use of the integrated version of the Clausius-Clapeyron equation (e.g., Iribarne and Godson, 1973); thus,

$$- \ln U_w = \frac{L_v}{R_v} \left(\frac{1}{T_d} - \frac{1}{T}\right) ,$$

or

$$T_d = \left[\frac{1}{T} - \frac{L_v}{R_v} \ln U_w\right]^{-1} , \tag{D.6}$$

Wet-bulb Potential Temperature and Lifting Condensation Level (LCL)

(i) The temperature at the LCL is computed by Inman's (1969) approximation:

$$T_c = t_d - (0.2071 + 0.001571\, t_d - 0.000436\, t_s)\Delta T_d , \tag{D.7}$$

where $\Delta T_d = T - T_d$ is the dew-point temperature depression.

(ii) The pseudo-adiabatic lapse rate is computed by (e.g. Hess, 1956)

$$\gamma_m = - \left(\frac{\partial T}{\partial z}\right)_{\text{pseudo-adia.}} = \gamma_d\left[\frac{1 + \frac{L_v}{R_d}\frac{\omega_s}{T}}{1 + \frac{0.622\, L_v^2}{c_p R_d}\frac{\omega_s}{T^2}}\right] , \tag{D.8}$$

where $\gamma_d = \frac{g}{c_p}$ is the dry-adiabatic lapse rate.

(iii) The approximate wet-bulb potential temperature is determined by integration of (D.8) with respect to pressure and by making use of the hydrostatic equation and the equation of state; thus,

$$\theta_w = T_c\left(\frac{1000}{P_c}\right)^{\frac{\gamma_m R}{g}}, \tag{D.9}$$

where $P_c = P\left(\frac{T_c}{T}\right)^{\frac{R_d}{c_p}}$ is the pressure at the LCL and $R = (1 + 0.61\,q)R_d$ is the specific gas constant for moist air.

(iv) The LCL for the lower layer can be obtained from

$$\hat{z}_c = \hat{z} + \frac{T - T_c}{\gamma_d}. \tag{D.10}$$

APPENDIX E

THE HORIZONTAL FILTER FOR THE
UNEVEN GRID SYSTEM

A simple one-dimensional, three-point asymmetrical filter analogous to the Fickian diffusion term is constructed for use in the stretched grid system. From the configuration of the grid system shown in Fig. 2.3, one can express the dependent variable φ at the grid points i+l and i-l in terms of φ and its derivatives at grid point i through the use of a Taylor series expansion. Thus, the second derivative at grid point i can be expressed as

$$\varphi_i'' = \frac{2}{d_i d_{i-1}(1+\lambda)}[\varphi_{i+1} + \lambda\,\varphi_{i-1} - (1+\lambda)\varphi_i] - \frac{d_i - d_{i-1}}{3}\varphi_i''' + \ldots\ldots\ldots,$$

or

$$d_i d_{i-1}\varphi_i'' \simeq \frac{2}{1+\lambda}[\varphi_{i+1} + \lambda\,\varphi_{i-1} - (1+\lambda)\varphi_i] + O(d_i - d_{i-1}) .$$

Then we construct the smoothing operator

$$\bar{\varphi}_i = \varphi_i + \frac{S}{2} d_i d_{i-1}\varphi_i'' ,$$

or

$$\bar{\varphi}_i = \varphi_i + \frac{S}{1+\lambda}[\varphi_{i+1} + \lambda\,\varphi_{i-1} - (1+\lambda)\varphi_i] , \qquad \text{(E.1)}$$

where S is the smoothing parameter. Since λ and the d's can vary from one grid point to another, a global analysis of the response function of (E.1) is not appropriate. However, a localized response analysis can be given.

Let $\varphi(x) = A\,e^{ikx}$ be a sinusoidal function in the domain; in the case of discrete points we can write

$$\varphi_j = \varphi(j\overset{*}{d}) = A\,e^{ikj\overset{*}{d}}$$

where $\overset{*}{d}$ is some scaling grid interval. The function values at adjacent points may be denoted by

$$\varphi_{j+\alpha} = \varphi[(j+\alpha)\overset{*}{d}] = A\,e^{ik(j+\alpha)\overset{*}{d}} = \varphi_j\,e^{ikd_j}, \quad \text{(E.2)}$$

$$\varphi_{j-\beta} = \varphi[(j-\beta)\overset{*}{d}] = A\,e^{ik(j-\beta)\overset{*}{d}} = \varphi_j\,e^{-ikd_{j-1}}, \quad \text{(E.3)}$$

where $d_j = \alpha\,\overset{*}{d}$ and $d_{j-1} = \beta\,\overset{*}{d}$.

The filter requires that

$$\bar{\varphi}_j = \varphi_j + \frac{S}{1+\lambda}[\varphi_{j+\alpha} + \lambda\,\varphi_{j-\beta} - (1+\lambda)\varphi_j]\ , \quad \text{(E.4)}$$

where $\lambda = \frac{\alpha}{\beta} = \frac{d_j}{d_{j-1}}$.

Substitution of (E.2) and (E.3) into (E.4) yields

$$\bar{\varphi}_j = \varphi_j\{1 + \frac{S}{1+\lambda}[e^{ikd_j} + \lambda\,e^{-ikd_{j-1}} - (1+\lambda)]\}.$$

Thus the response function is

$$R(k,S,\lambda) = \frac{\bar{\varphi}_j}{\varphi_j} = 1 + \frac{S}{1+\lambda}[e^{ikd_j} + \lambda\,e^{-ikd_{j-1}} - (1+\lambda)]\};$$

(E.5)

the magnitude of R is

$$|R| = \{[1 - S + \frac{S}{1+\lambda}(\cos \lambda k \hat{d} + \lambda \cos k \hat{d})]^2$$

$$+ \frac{S^2}{(1+\lambda)^2}(\sin \lambda k \hat{d} - \lambda \sin k \hat{d})^2\}^{\frac{1}{2}}, \qquad \text{(E.6)}$$

where we denote $\hat{d} = d_{j-1}$ and $\lambda \hat{d} = d_j$.

In the case of evenly spaced grid points, $\lambda = 1$, and (E.6) reduces to

$$R = 1 - S(1 - \cos k\hat{d}) , \qquad \text{(E.7)}$$

which is the familiar response function of the elementary filter. Taking $S = \frac{1}{2}$ for maximum suppression of 2-D irregularities, the response function (E.6) will differ only slightly from (E.7) for small amounts of stretching (say, for $1 < \lambda \leq 1.3$), as is seen in Fig. E.1. Although it is difficult to examine the overall properties of the operator (E.1) because of the scale-varying character, the application of (E.1) essentially produces the same smoothing effect as that of a regular filter, provided that the grid stretching is suitably small.

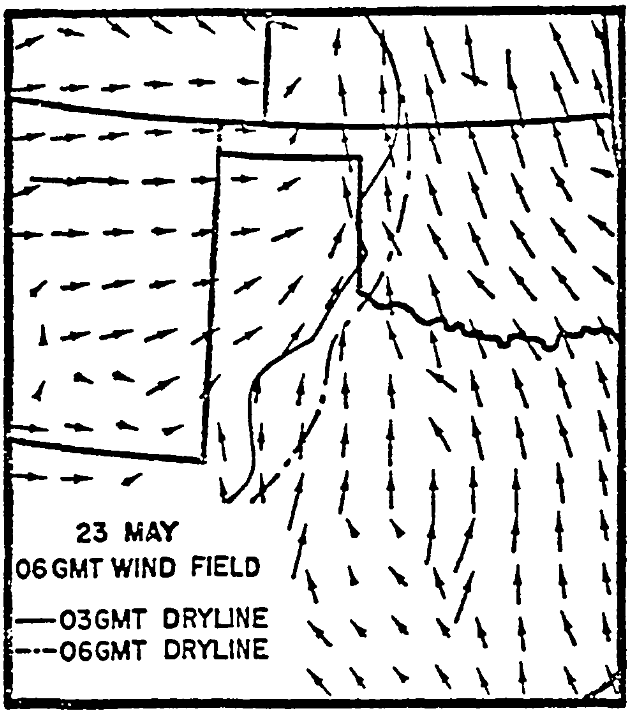

Fig. 1.1. Wind field for 0600 GMT 23 May 1966 and displacement of dry line (Shaefer, 1973).

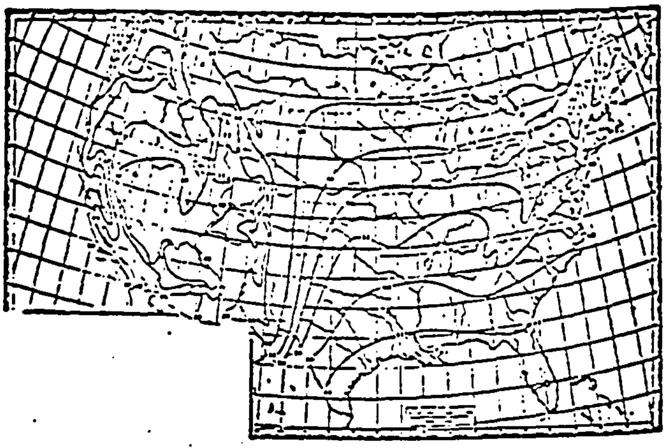

Fig. 2.1. Mean dew-point temperature field (°F) in May (from Dodd, 1965); (Shaefer, 1974).

Fig. 2.2. Mean topography of the United States in thousands of feet (from McClain, 1960).

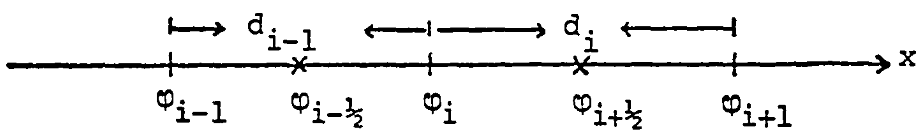

Fig. 2.3. The uneven grid system.

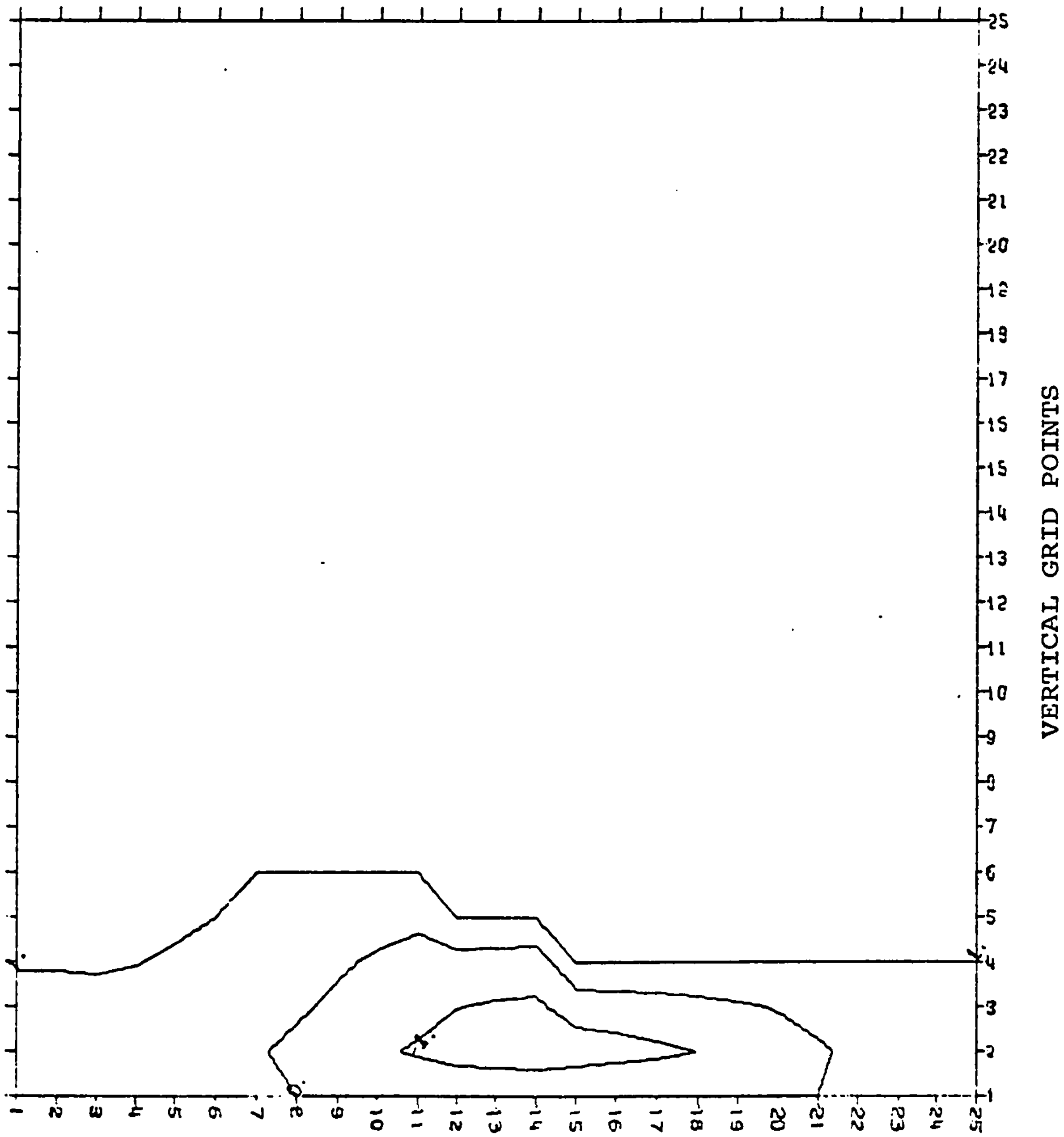

Fig. 2.4. Initial u-component wind (m sec^{-1}).

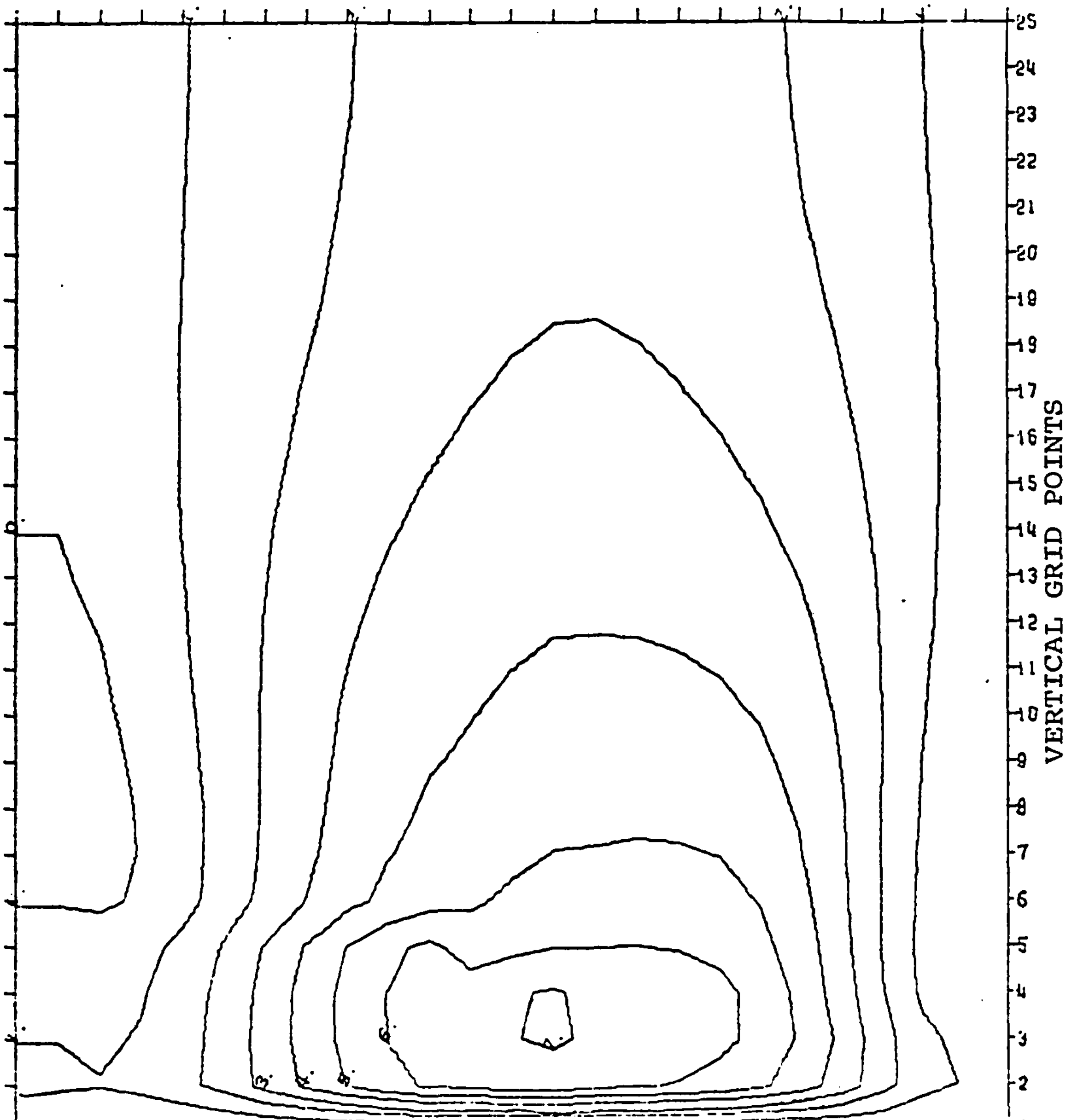

Fig. 2.5. Initial v-component wind (m sec^{-1}).

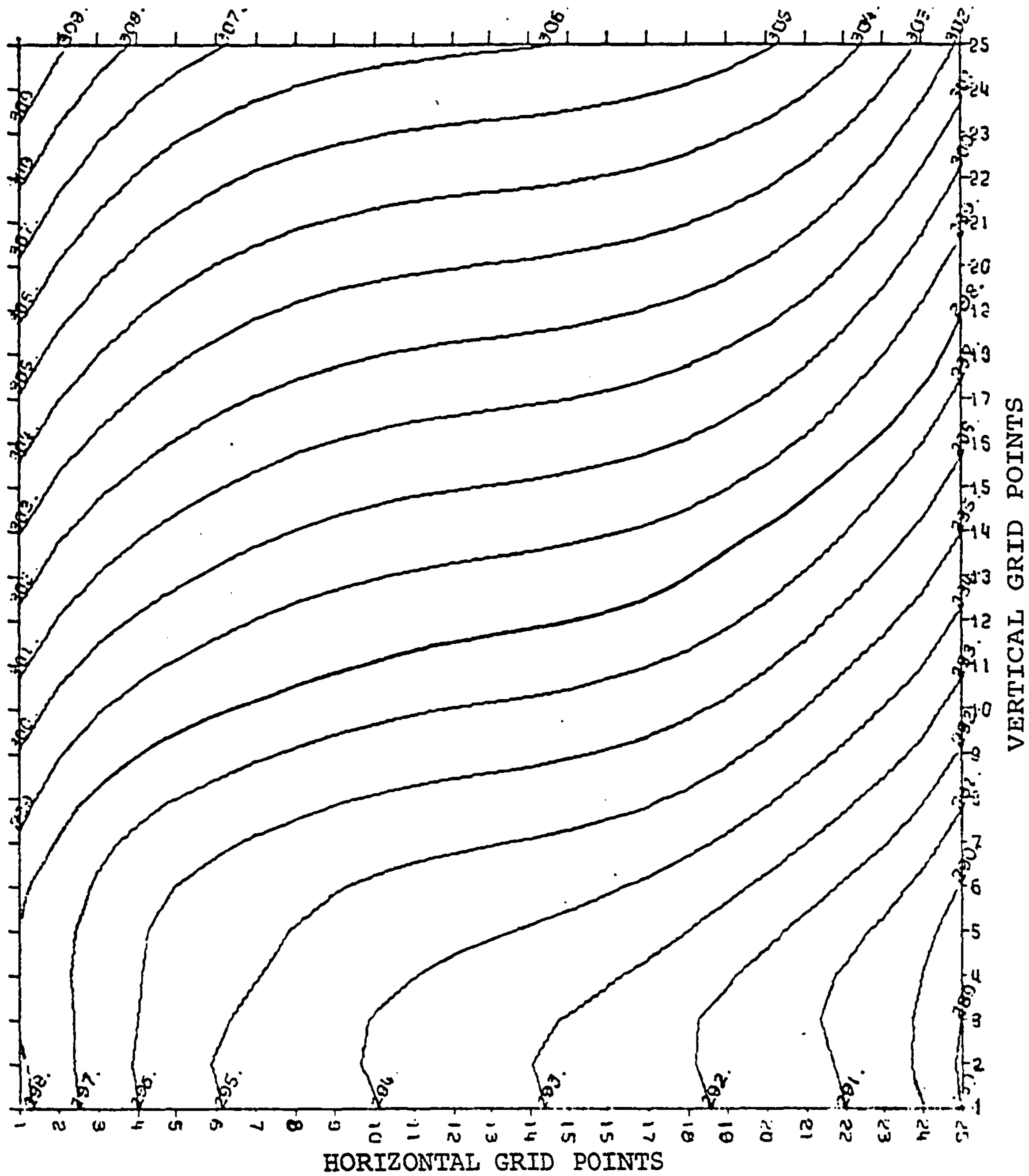

Fig. 2.6. Initial potential temperature (°K) field.

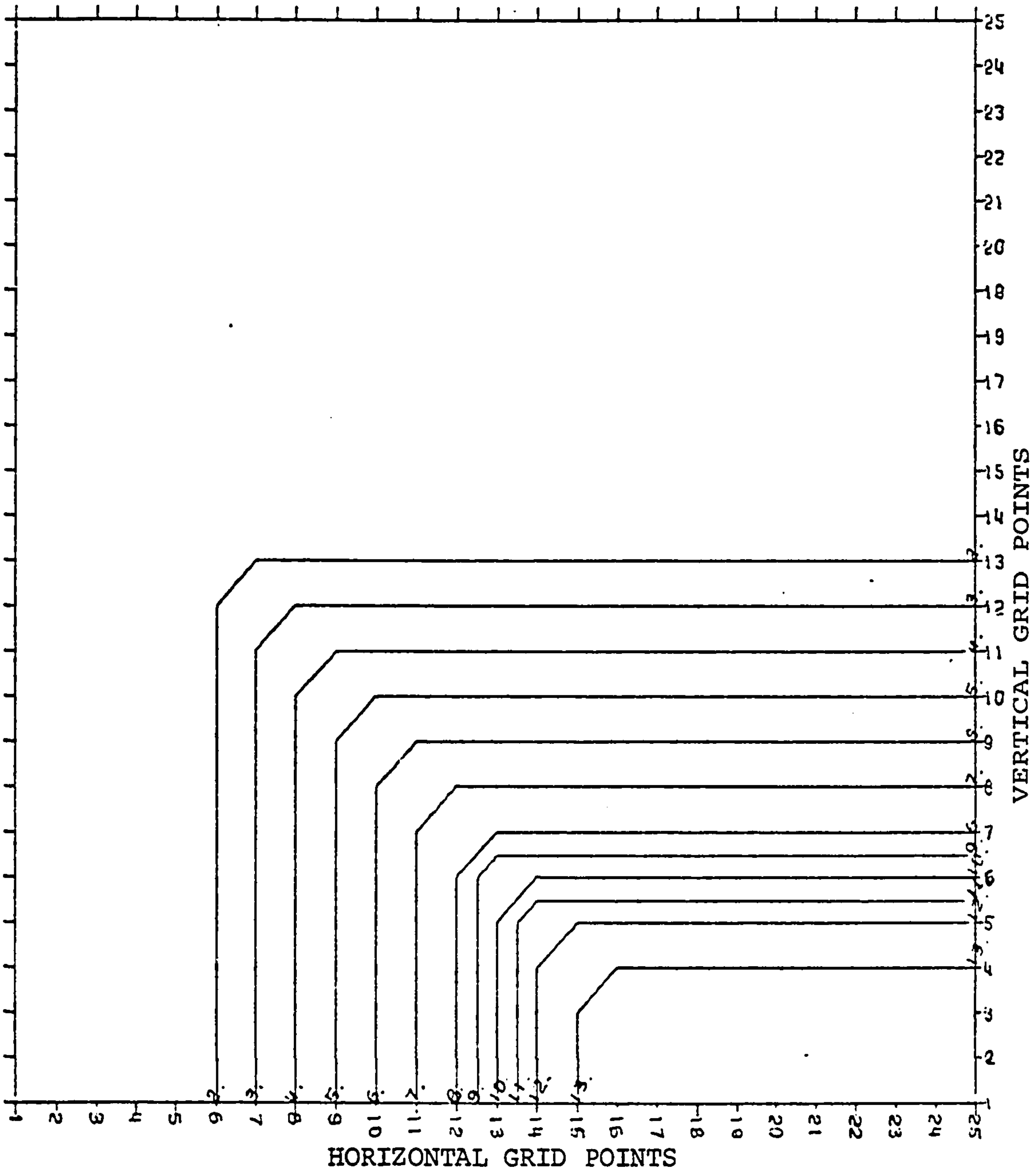

Fig. 2.7. Initial specific humidity (g kg^{-1}) field.

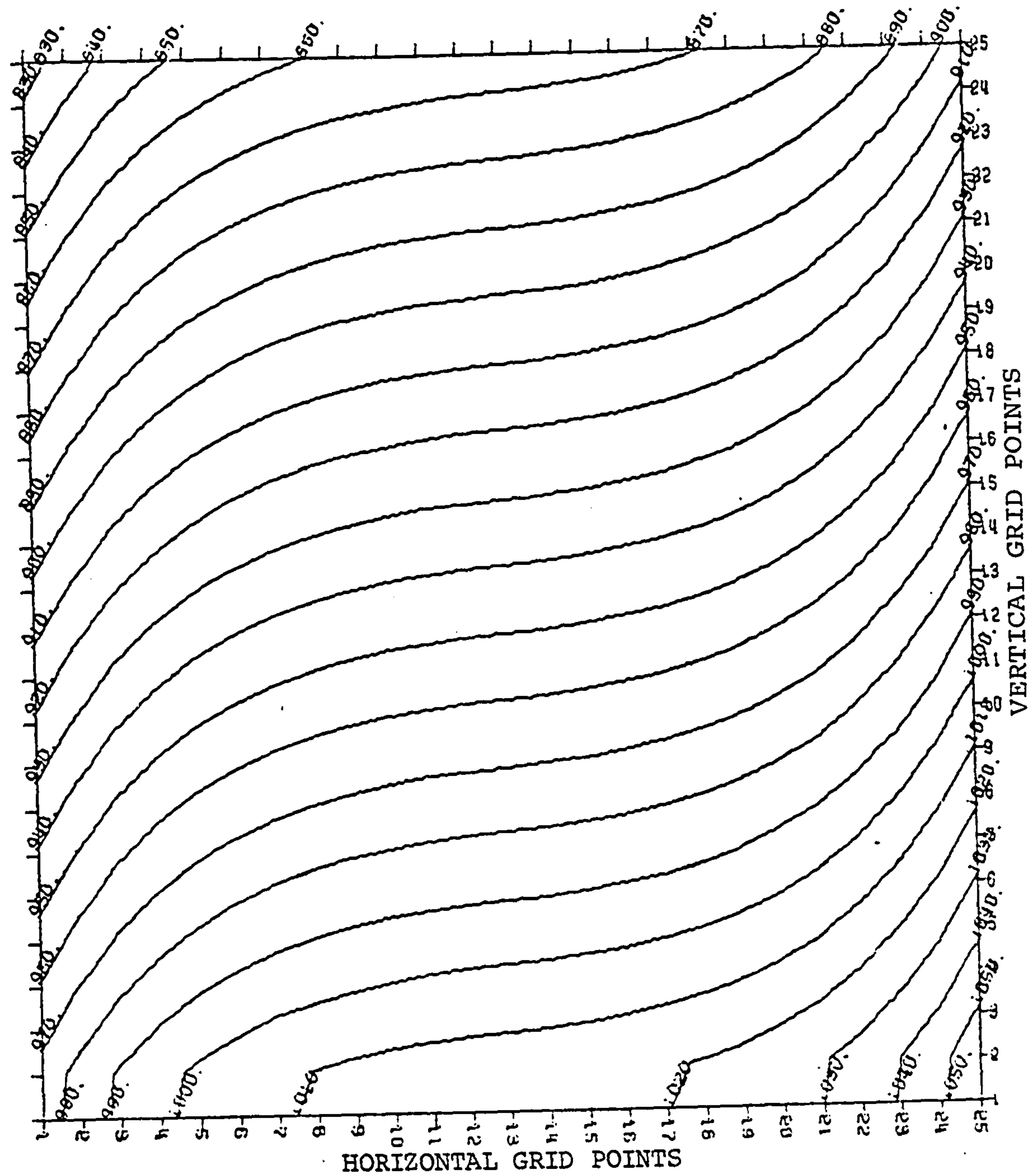

Fig. 2.8. Initial Exner function ($m^2\ sec^{-2}\ {}^\circ K^{-1}$) field.

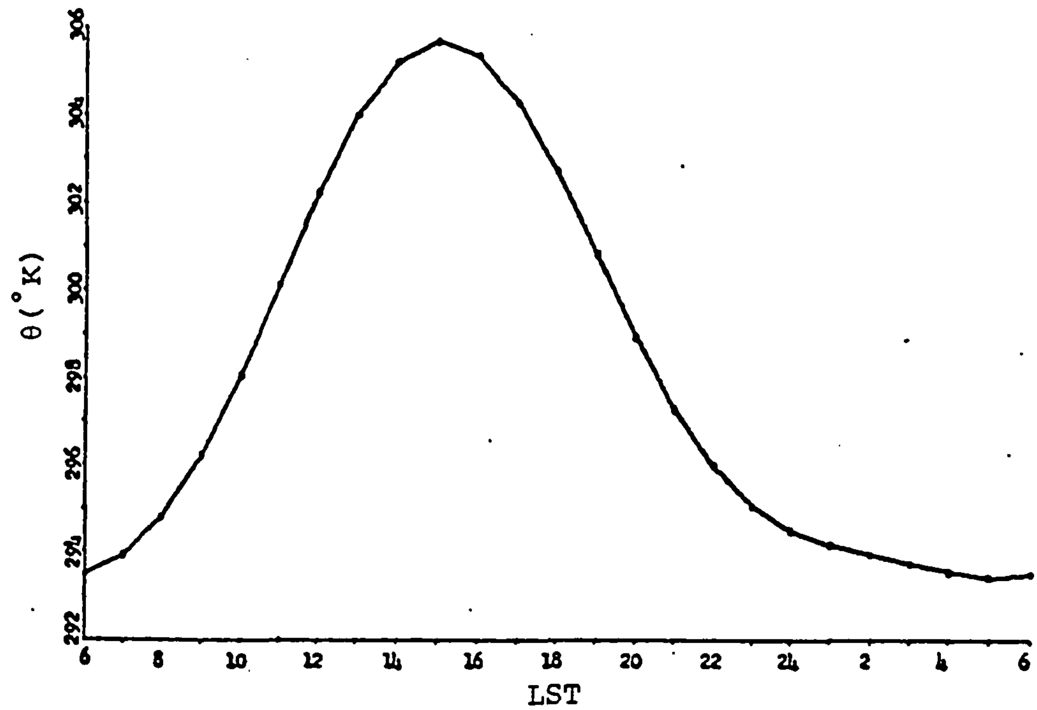

Fig. 2.9. Diurnal variation of surface potential temperature at middle grid point (i = 13).

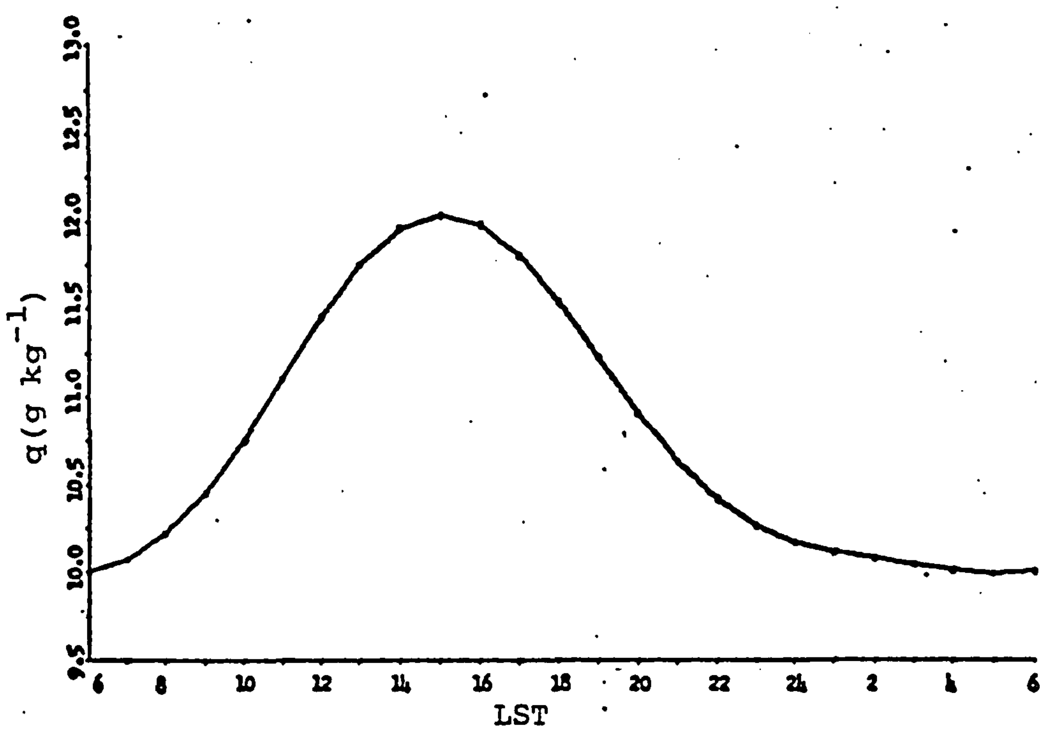

Fig. 2.10. The same as Fig. 2.9 except for specific humidity.

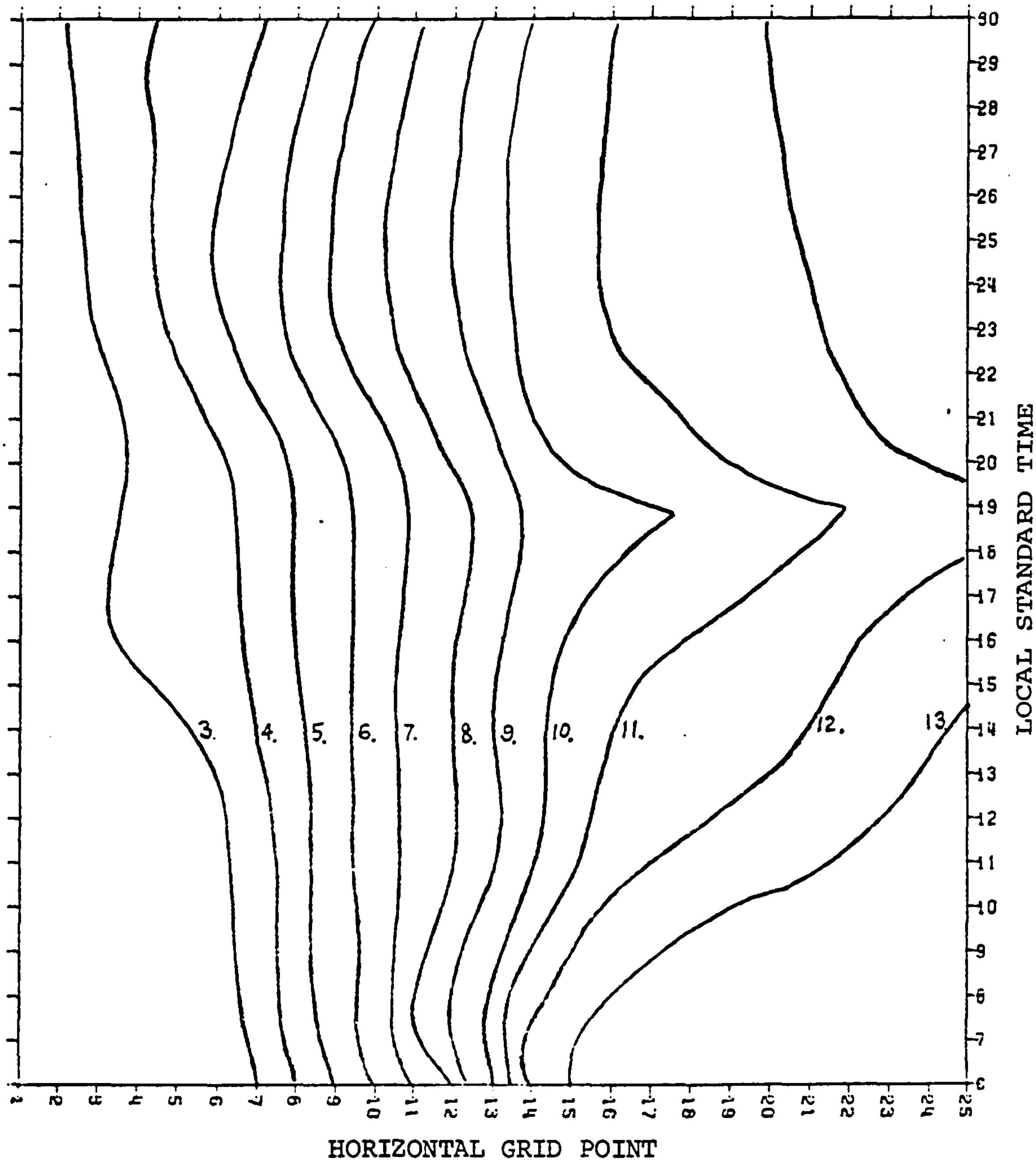

Fig. 3.1. Time section (x-t) of specific humidity (g kg^{-1}) at the top of the surface layer ($\hat{z}$ = 25 m) for a diurnal-cycle simulation, Case A_1; 25-30 LST stands for 01-06 LST of the second day.

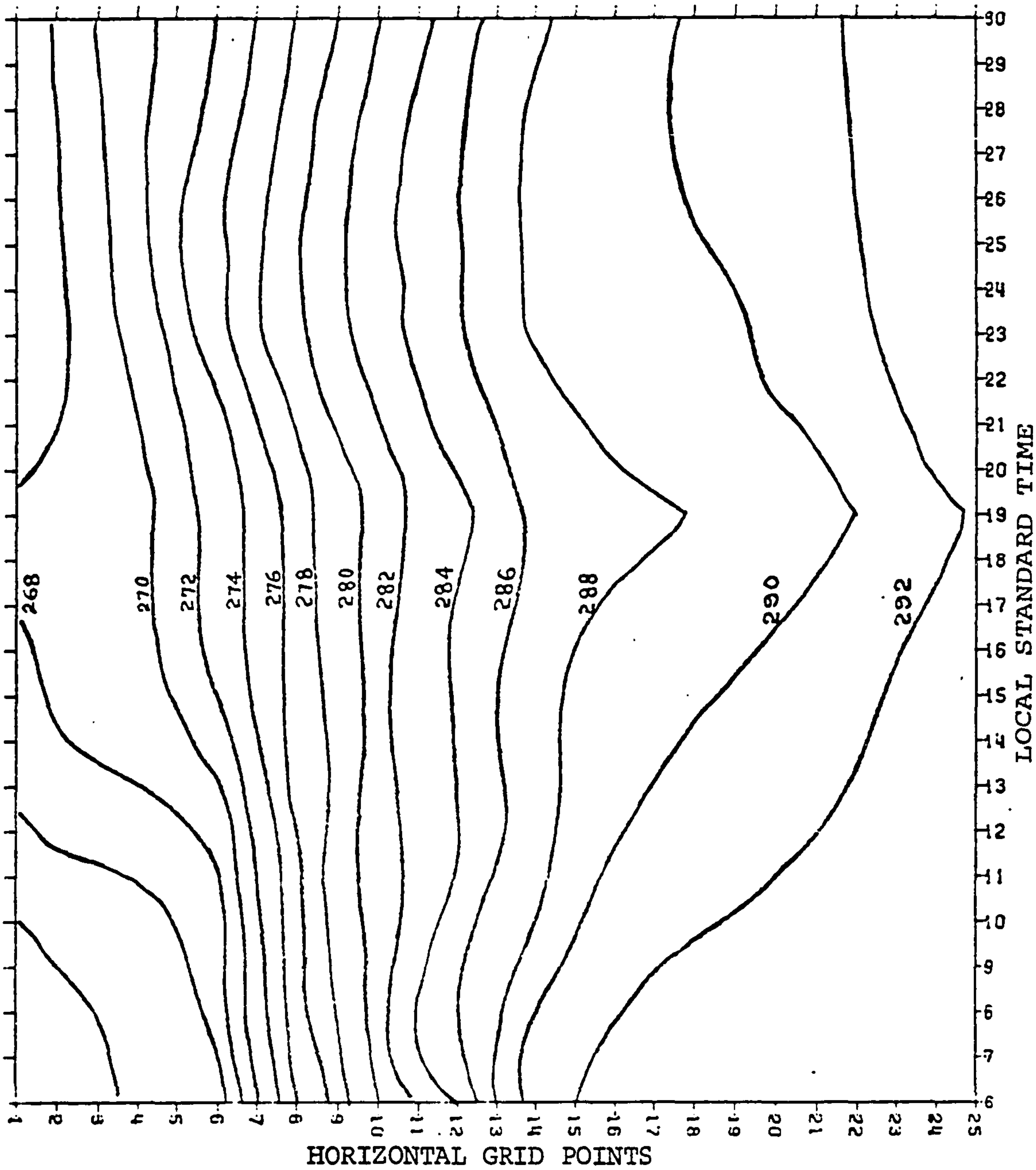

Fig. 3.2. Same as Fig. 3.1 except for dew-point temperature (°K).

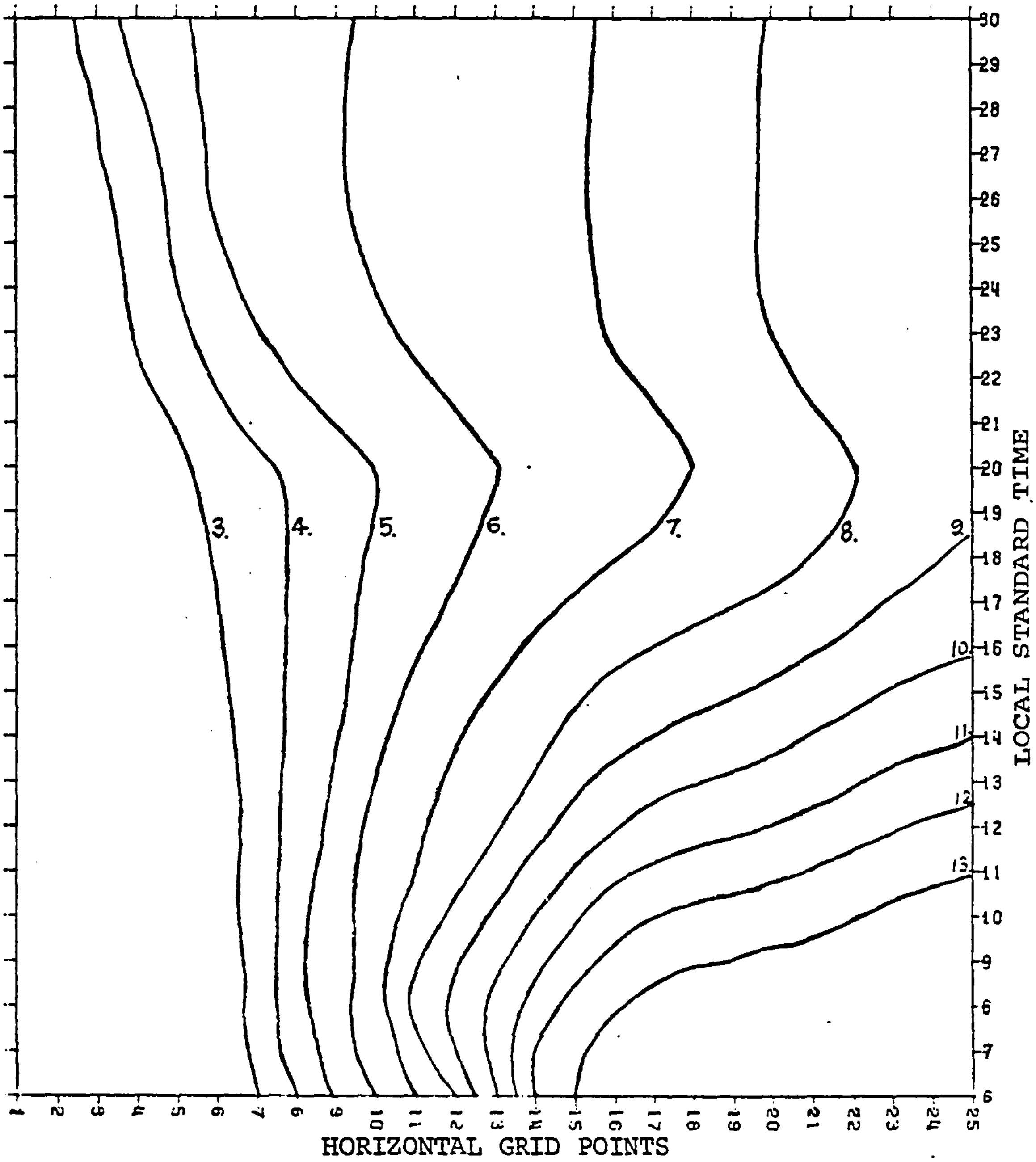

Fig. 3.3. Same as Fig. 3.1 except for Case A_2.

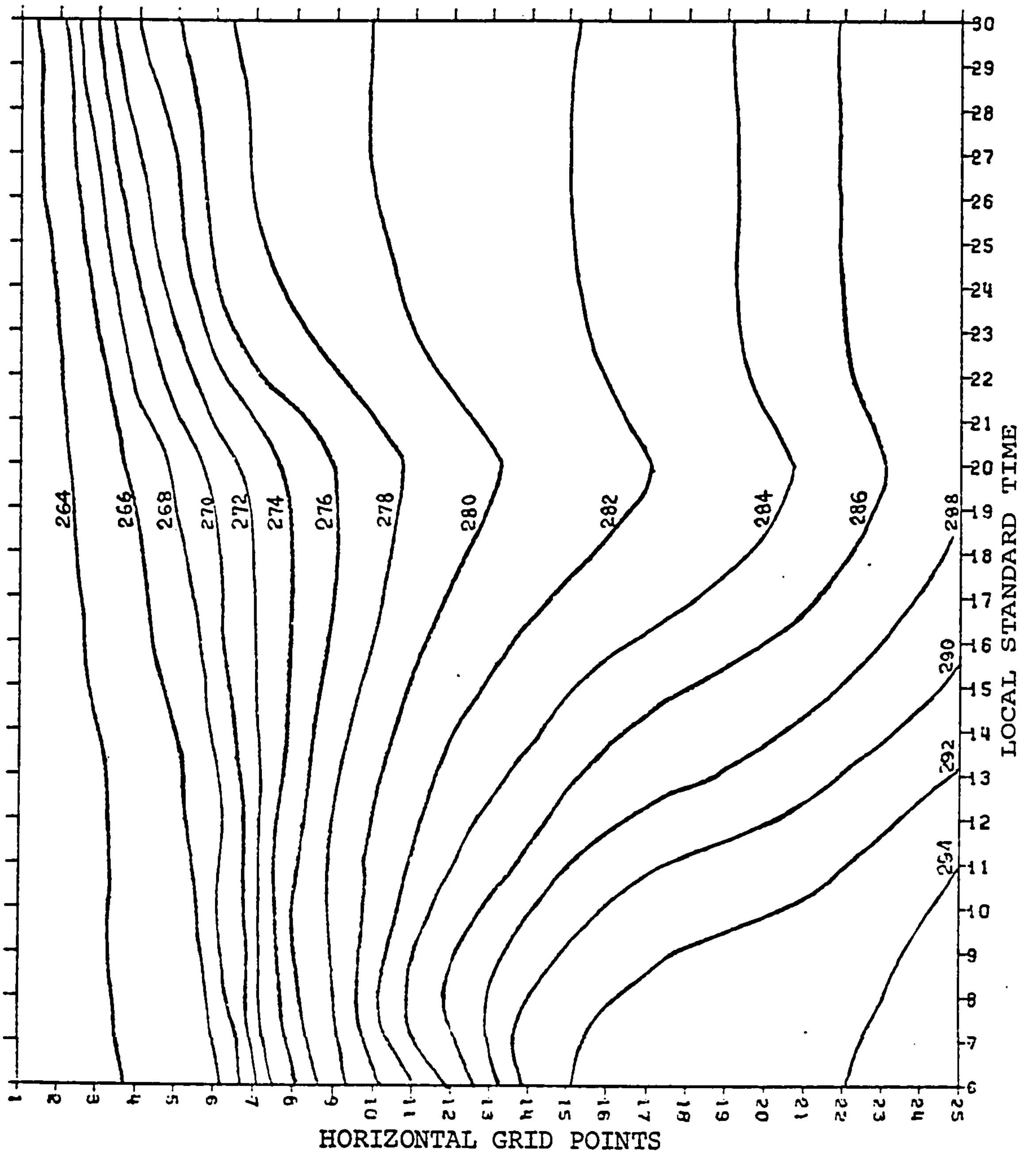

Fig. 3.4. Same as Fig. 3.2 except for Case A_2.

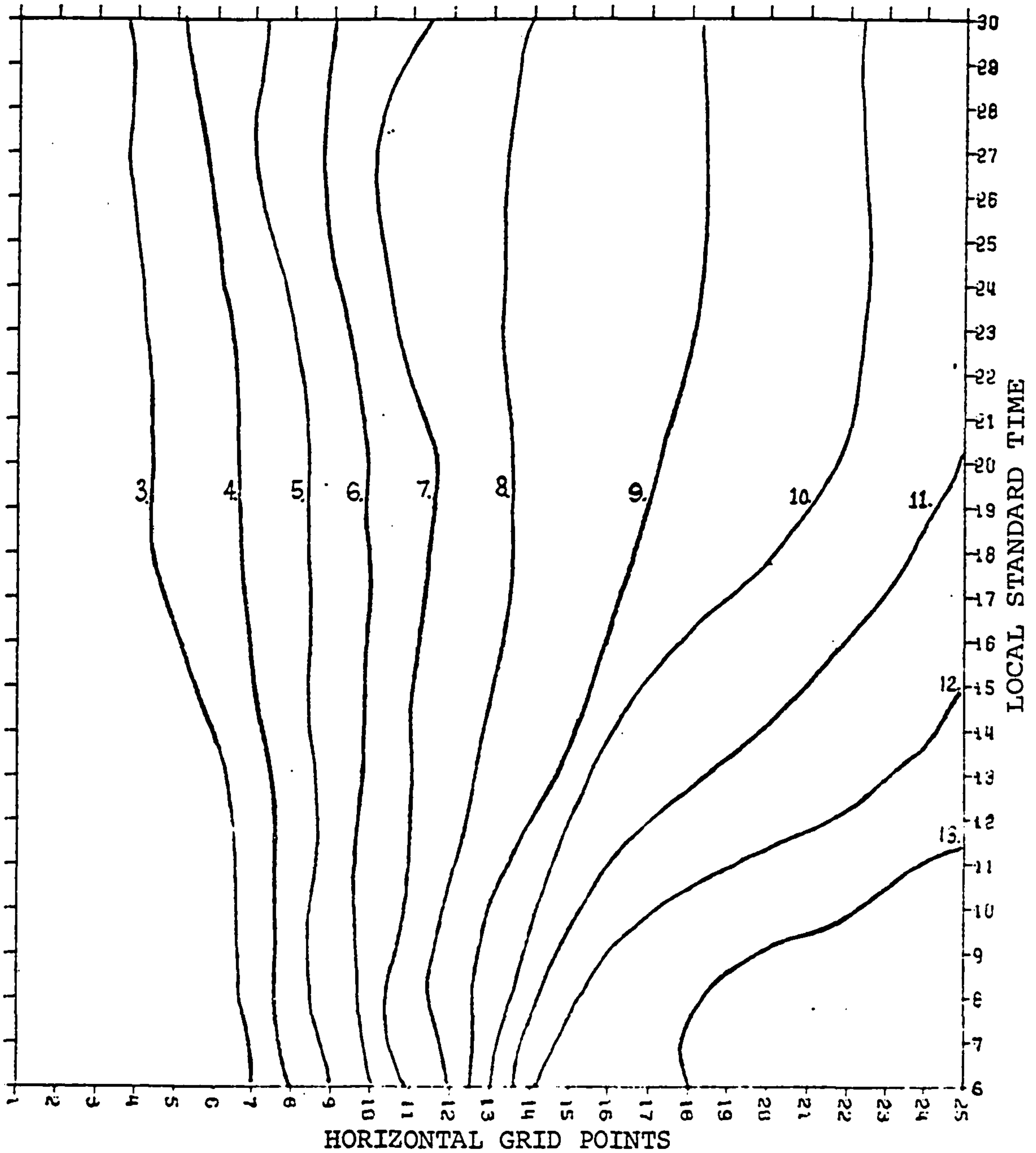

Fig. 3.5. Same as Fig. 3.1, except at the height $\hat{z}$ = 425 m.

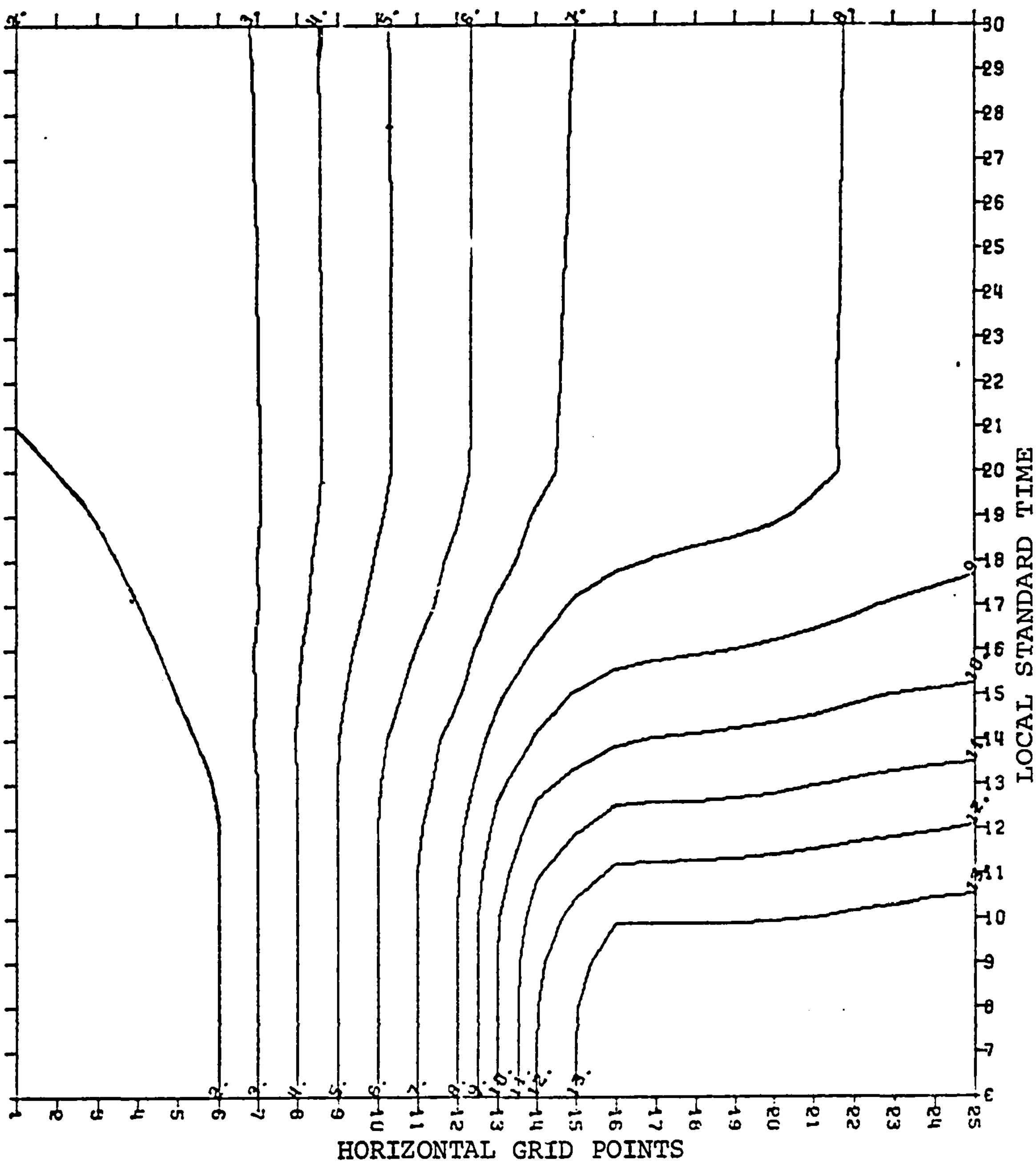

Fig. 3.6. Same as Fig. 3.1, except for Case B.

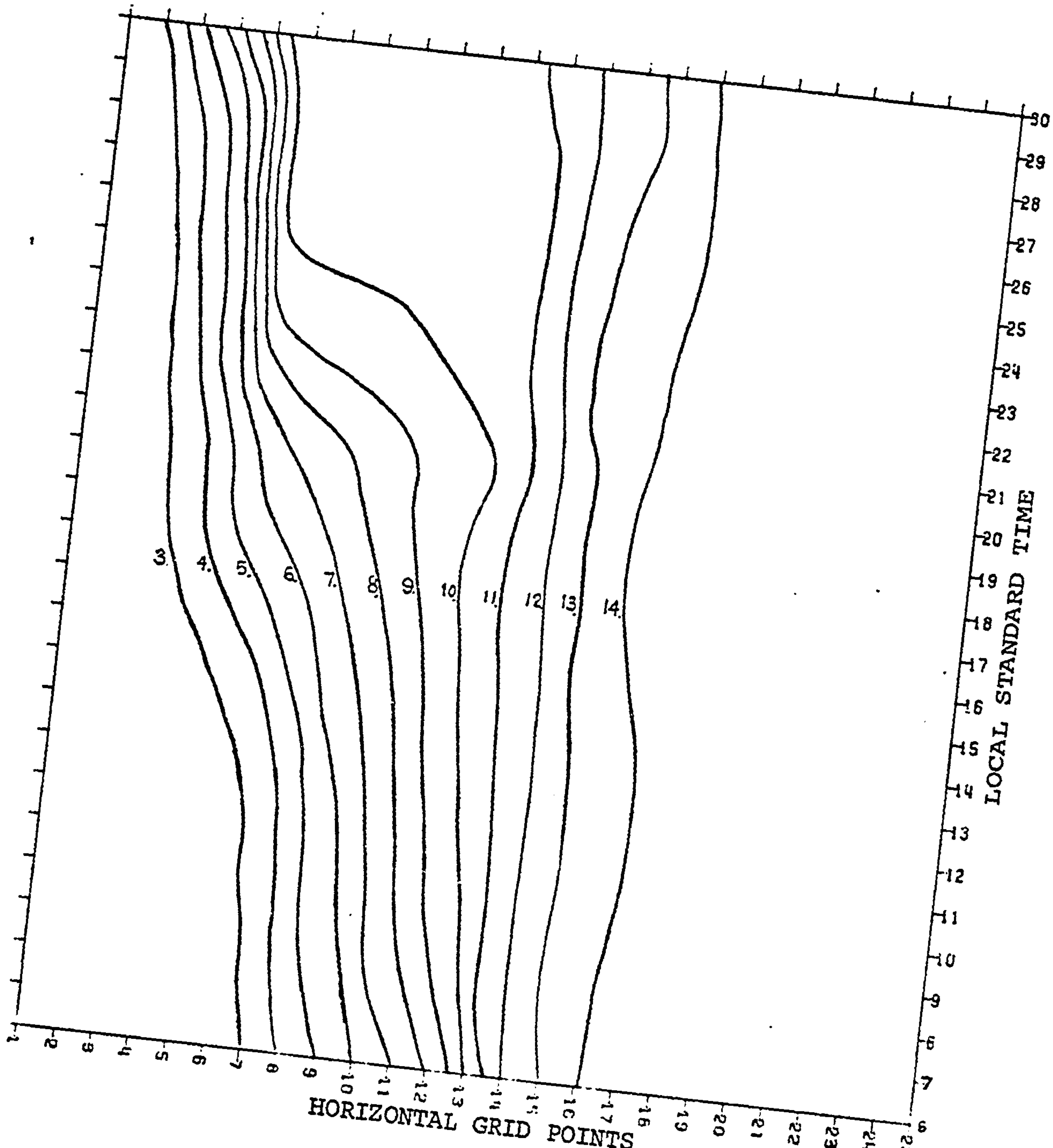

Fig. 3.7. Same as Fig. 3.1, except for Case C.

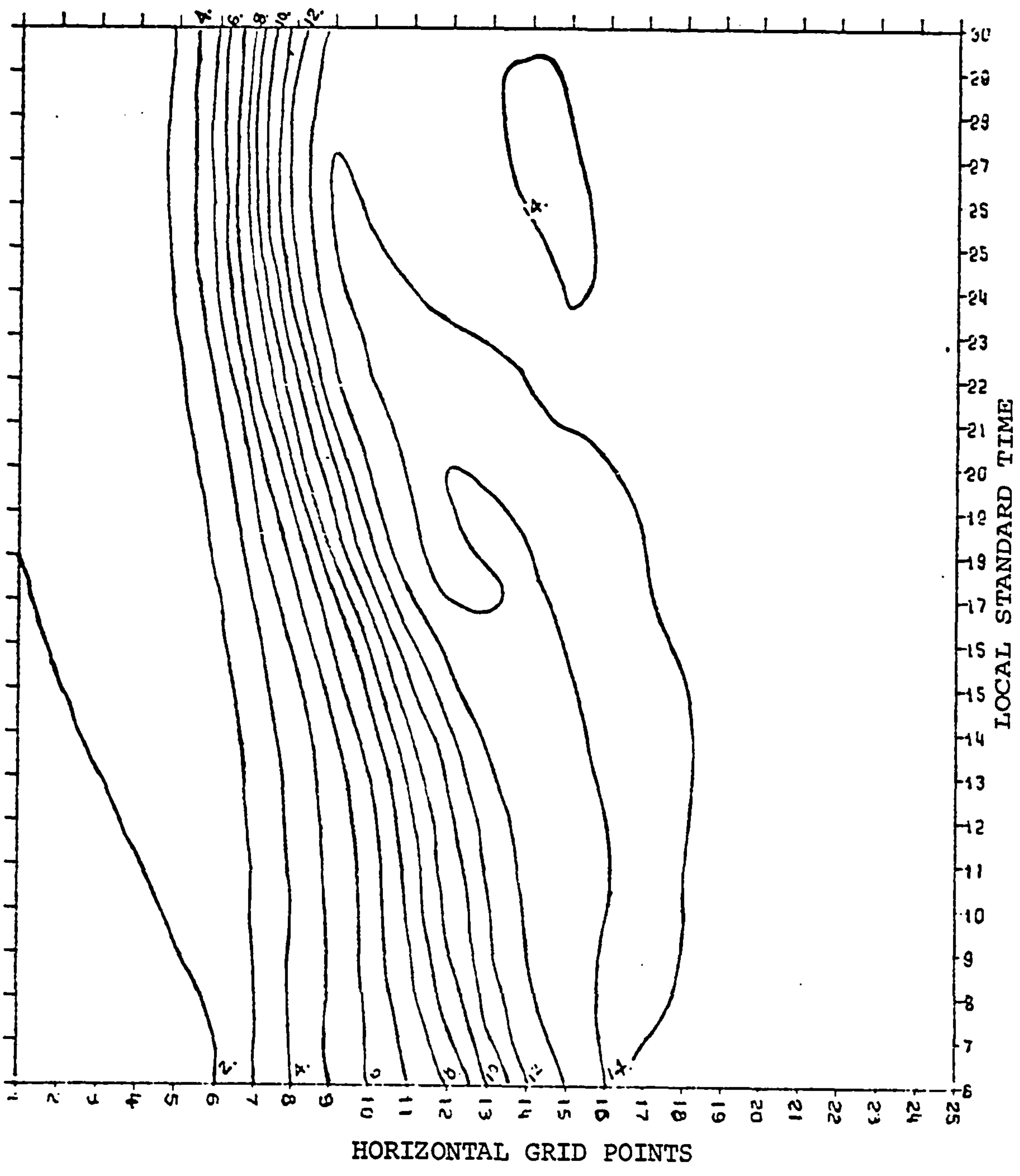

Fig. 3.8. Same as Fig. 3.1, except for Case D.

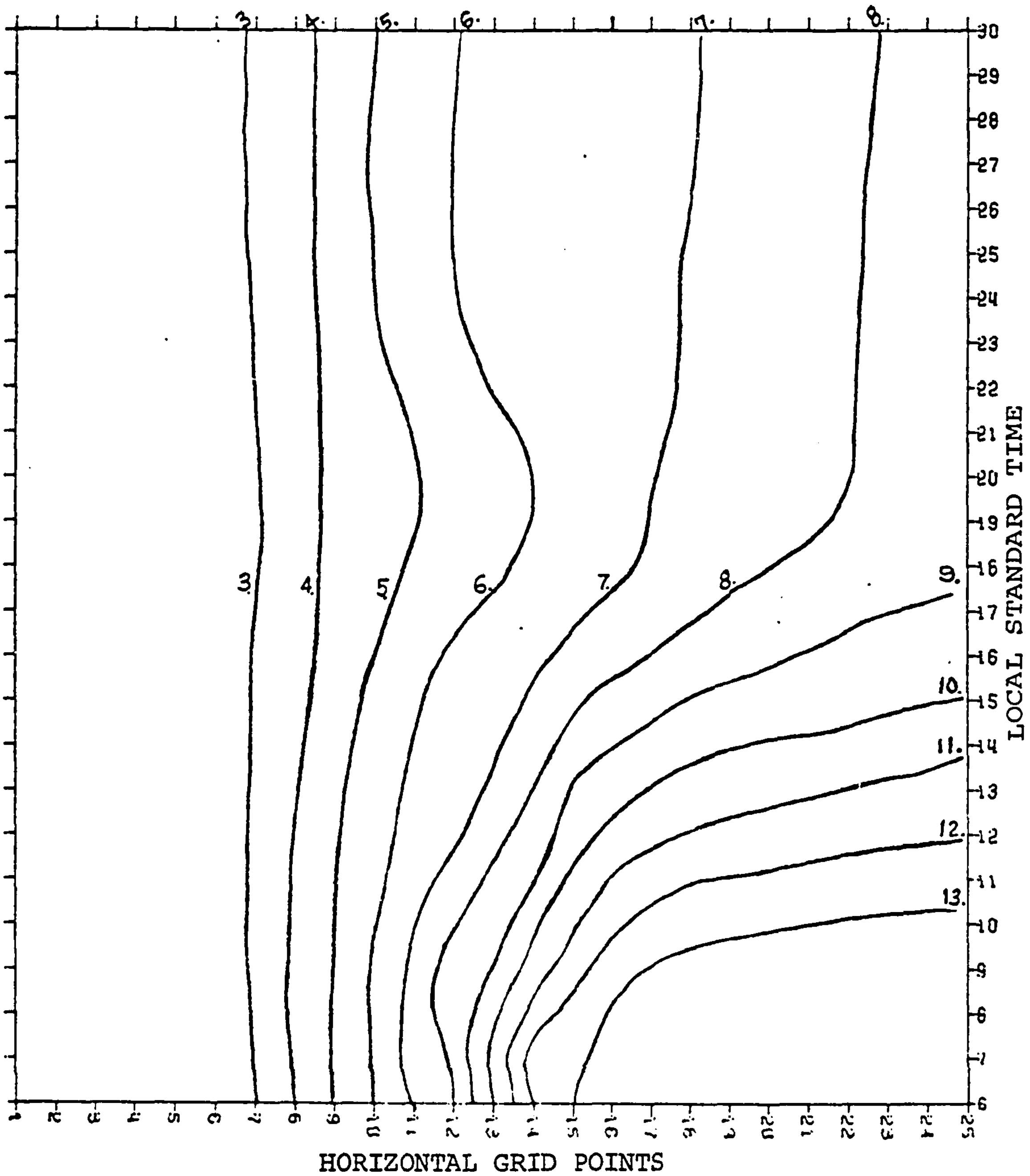

Fig. 3.9. Same as Fig. 3.1, except for Case E.

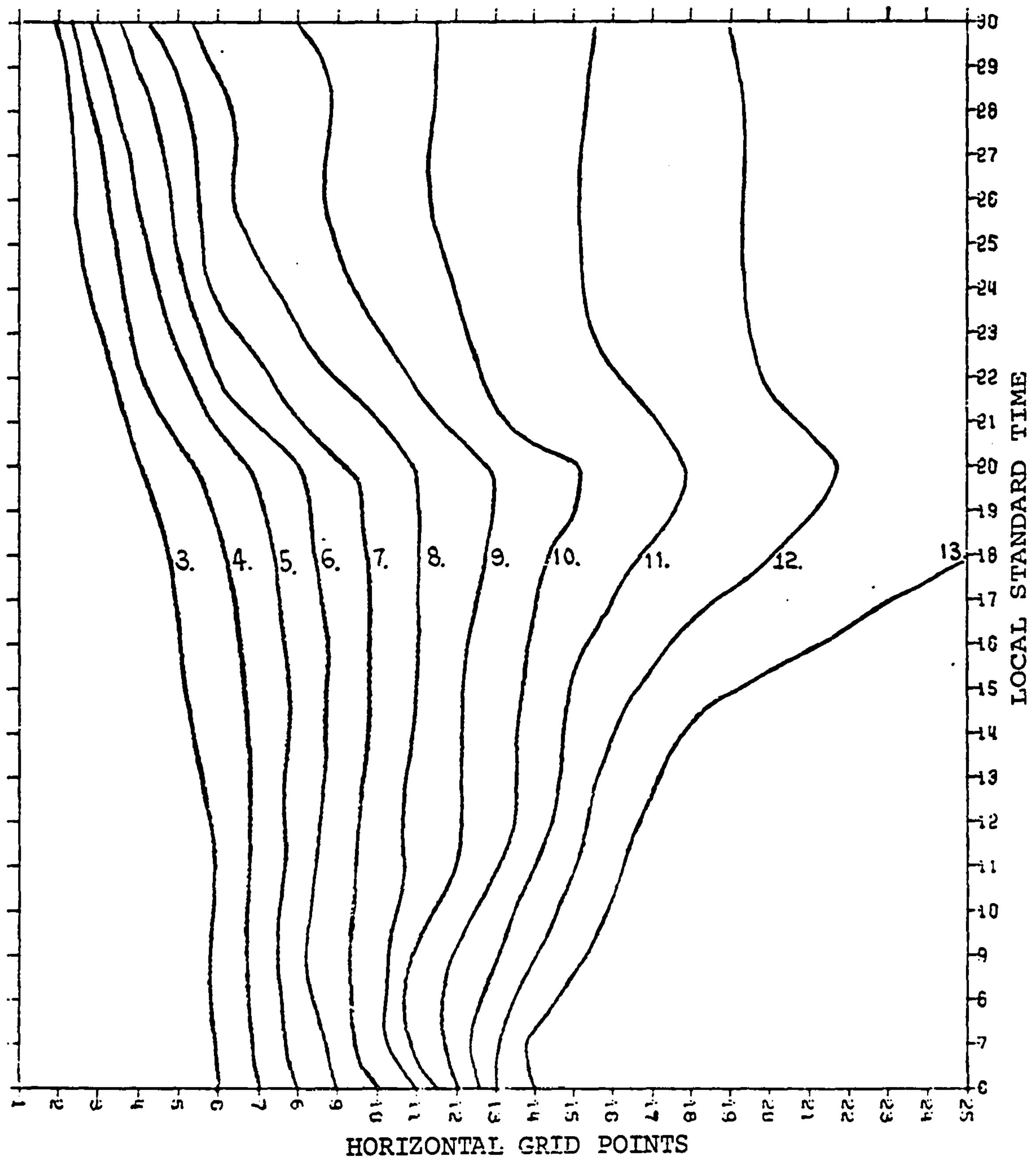

Fig. 3.10. Same as Fig. 3.1, except for Case F.

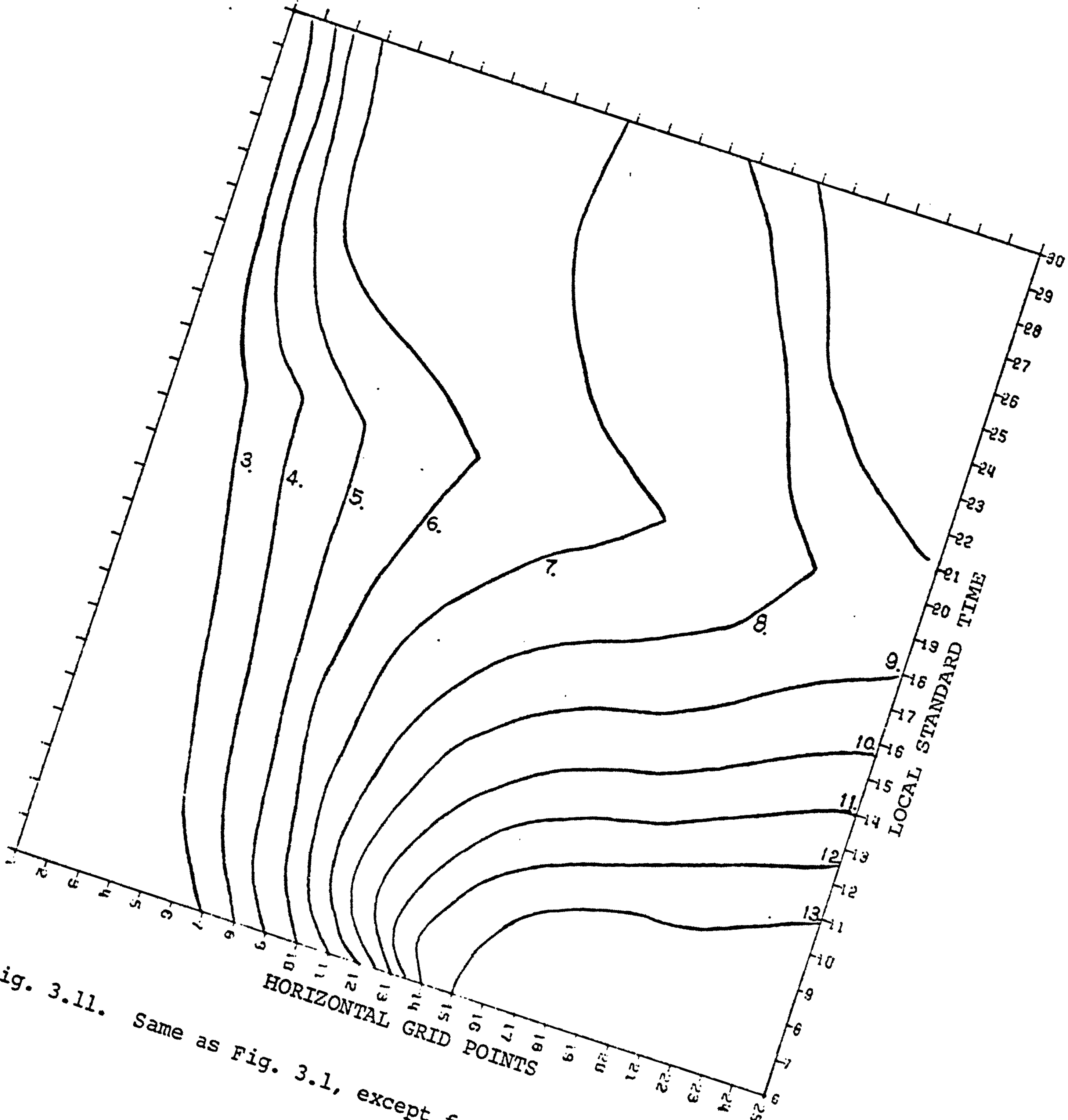

Fig. 3.11. Same as Fig. 3.1, except for Case G.

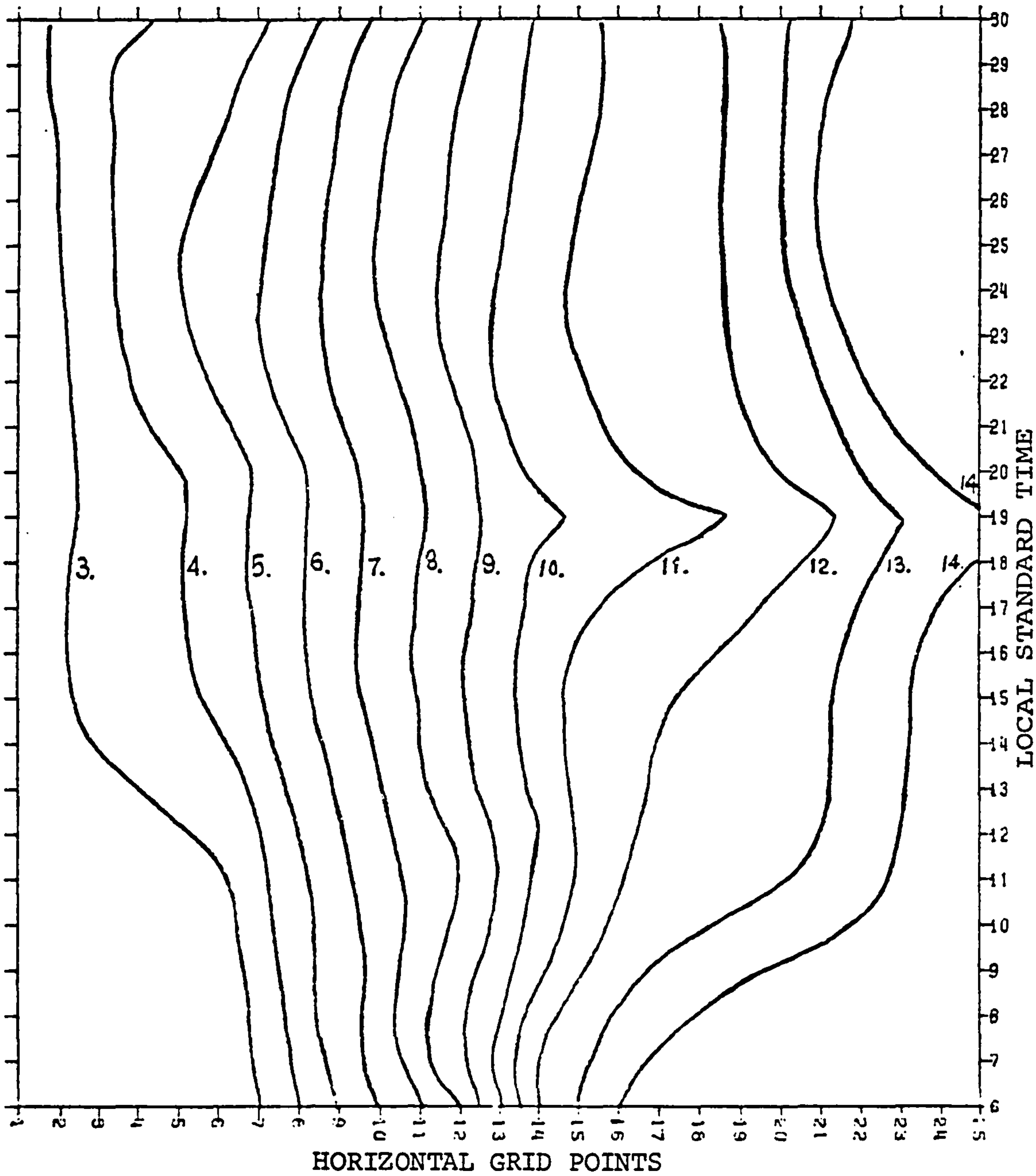

Fig. 3.12. Same as Fig. 3.1, except for Case H.

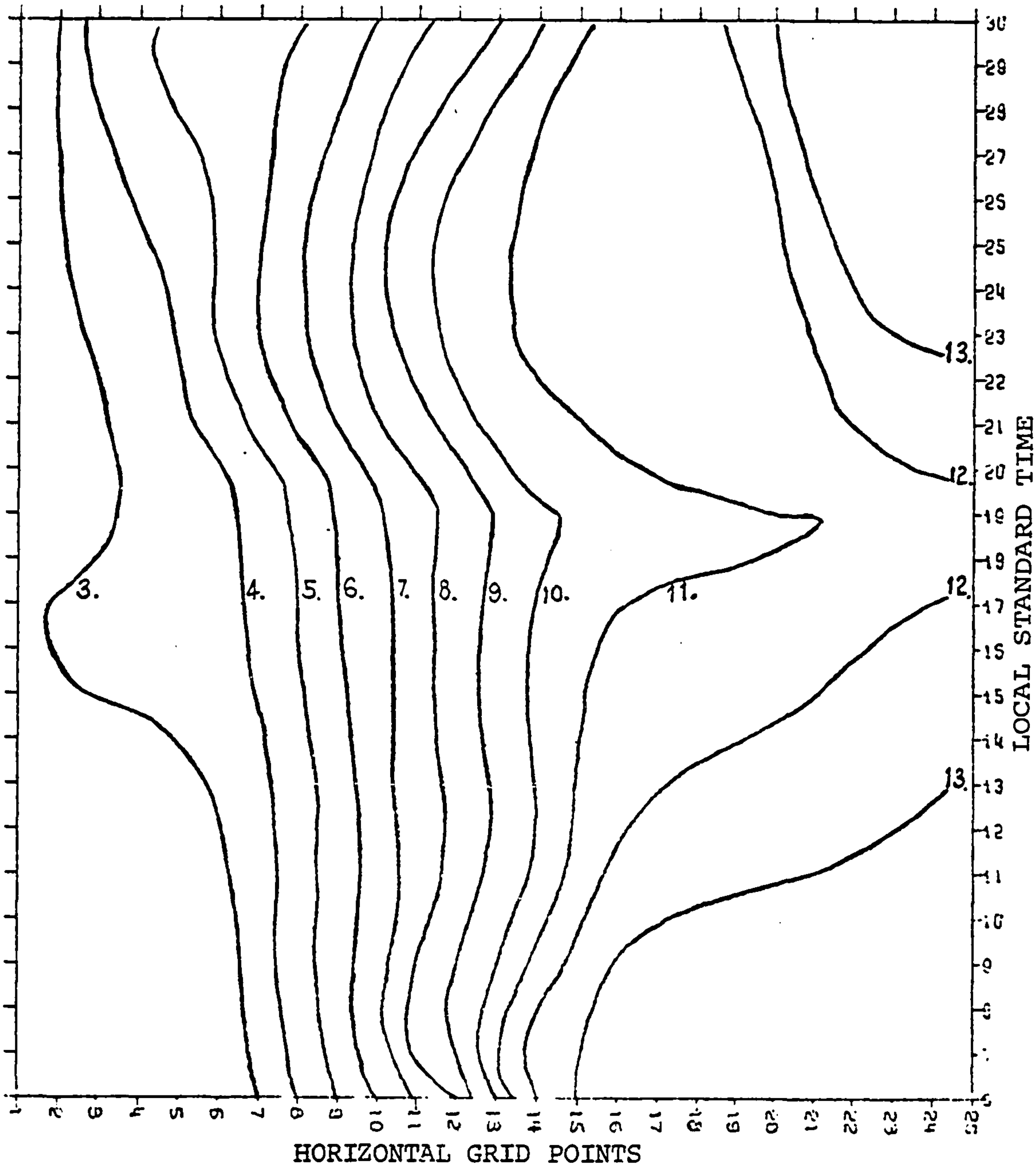

Fig. 3.13. Same as Fig. 3.1, except for Case I.

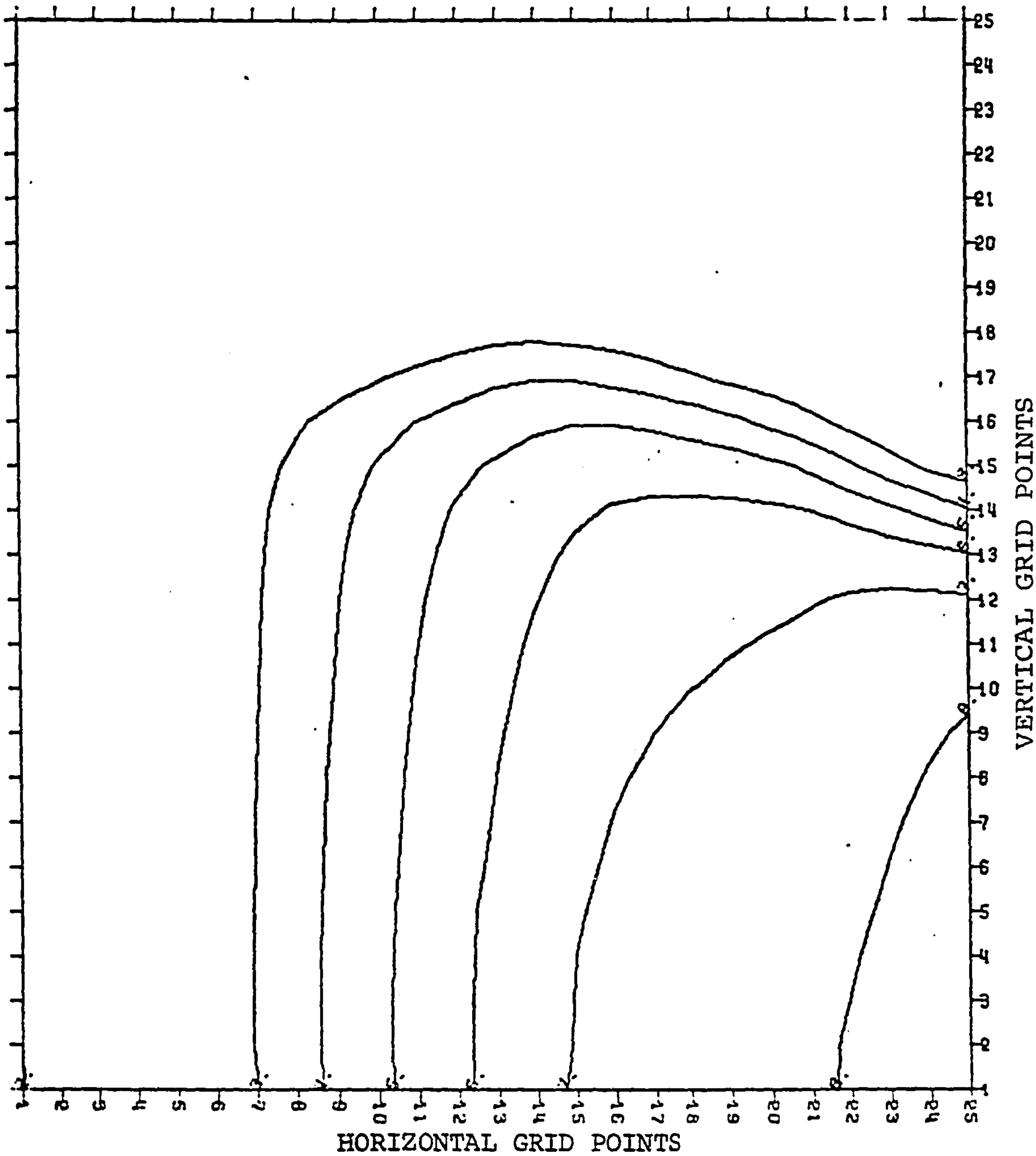

Fig. 3.14. Specific humidity (g kg^{-1}) at 2400 LST, Case B.

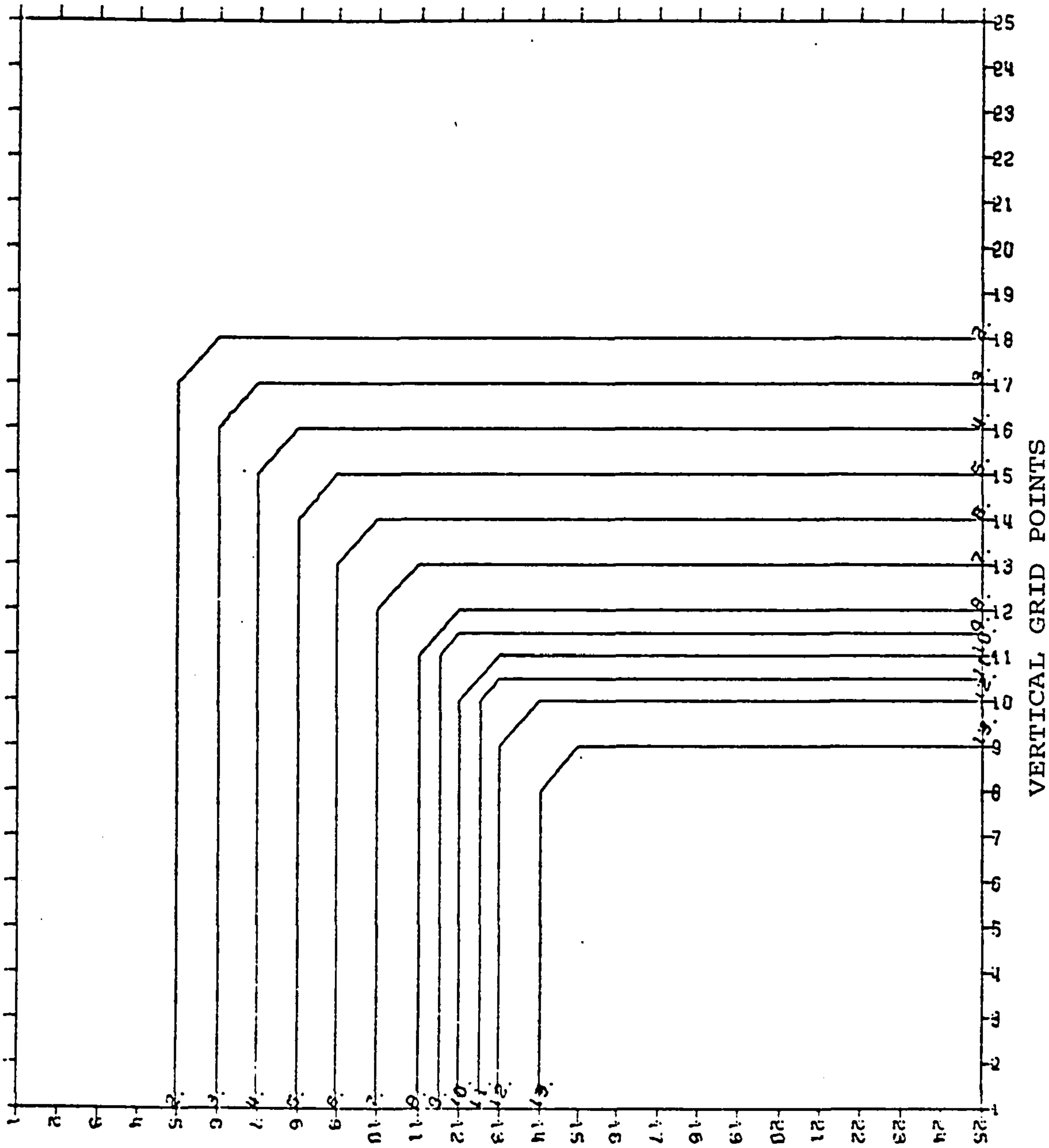

Fig. 3.15. Initial field of specific humidity (g kg^{-1}) for Case F.

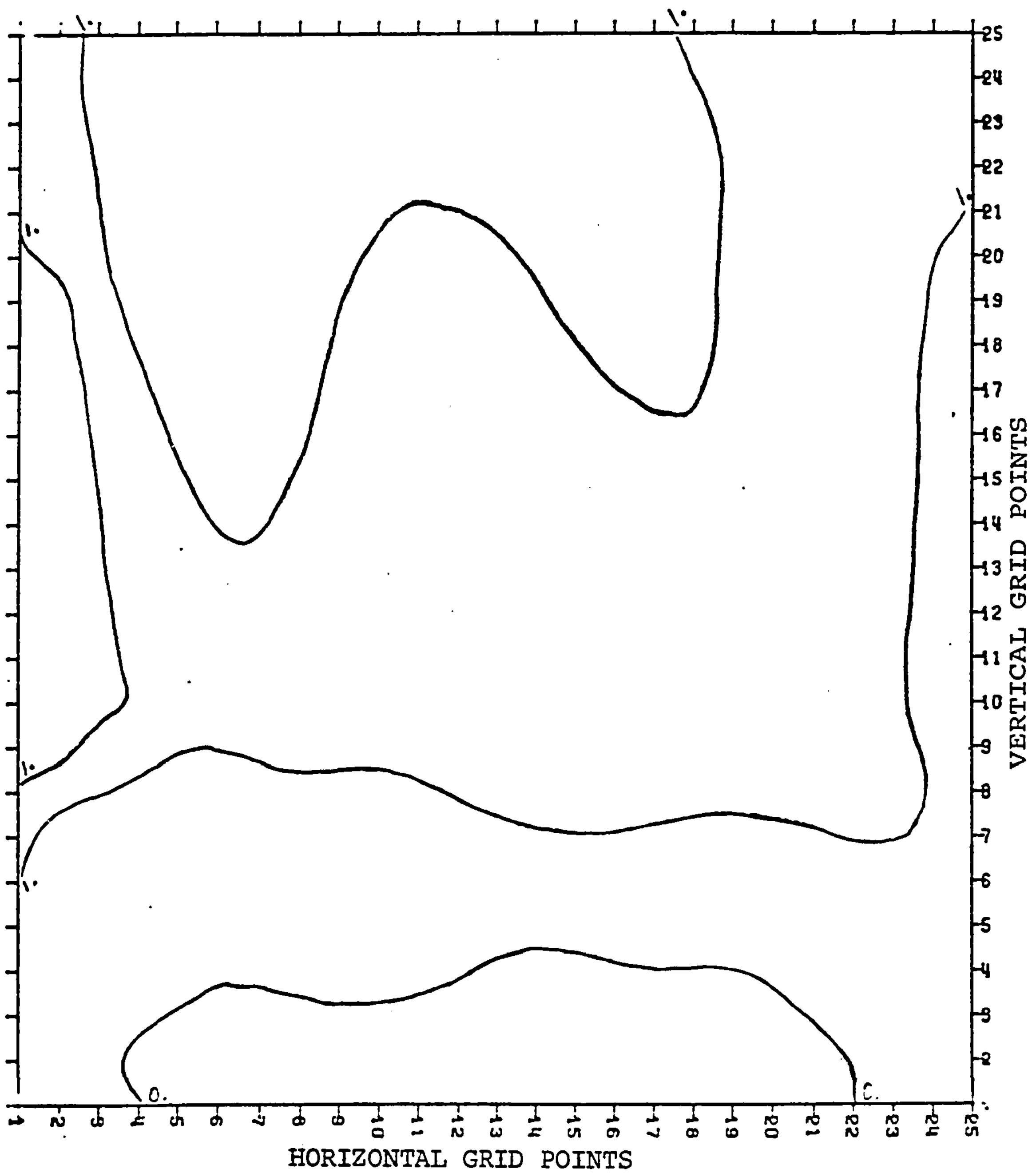

Fig. 4.1a. u-component wind field (m s^{-1}) at 1200 LST, Case A_1.

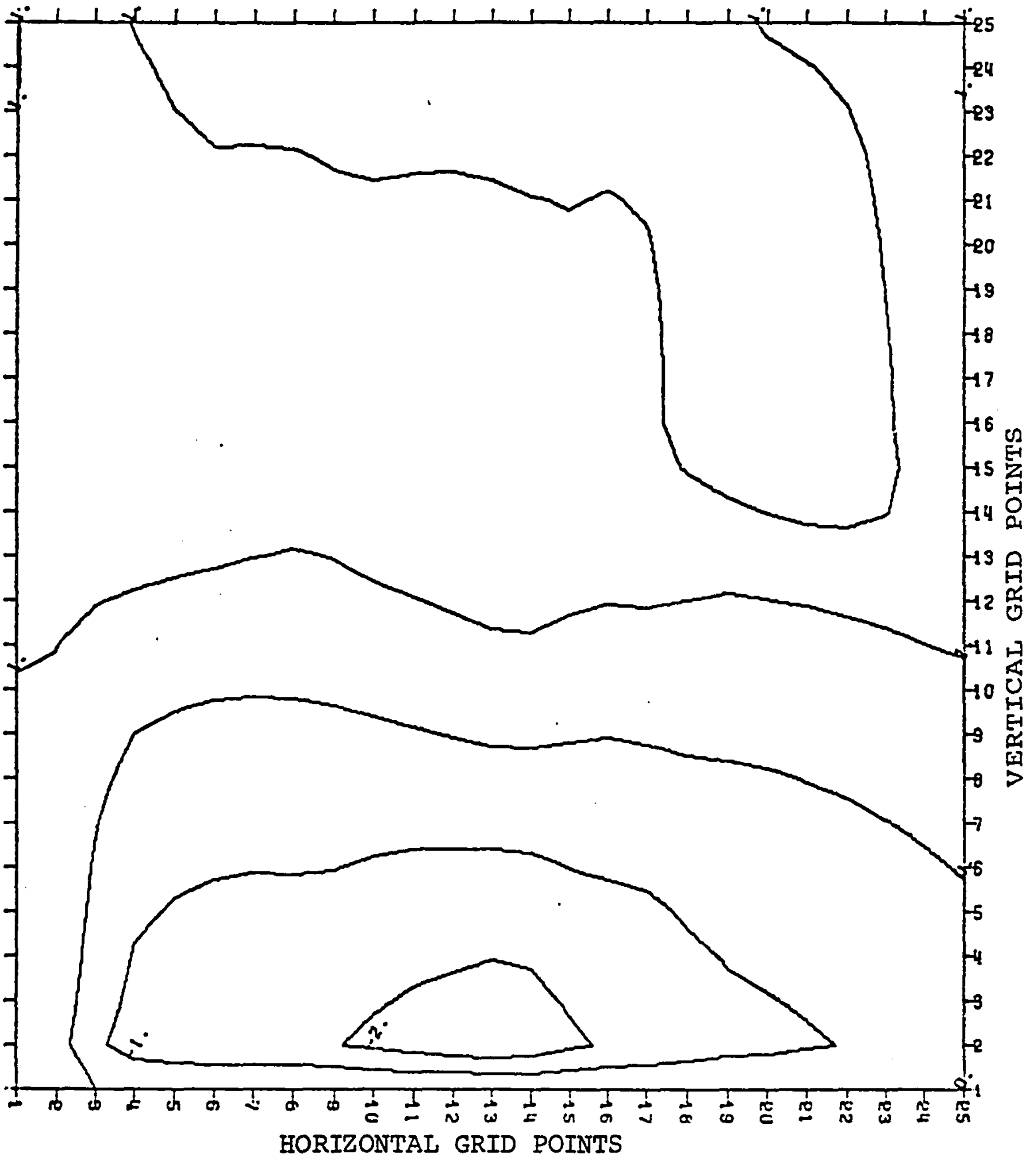

Fig. 4.1b. u-component wind at 1600 LST, Case A_1.

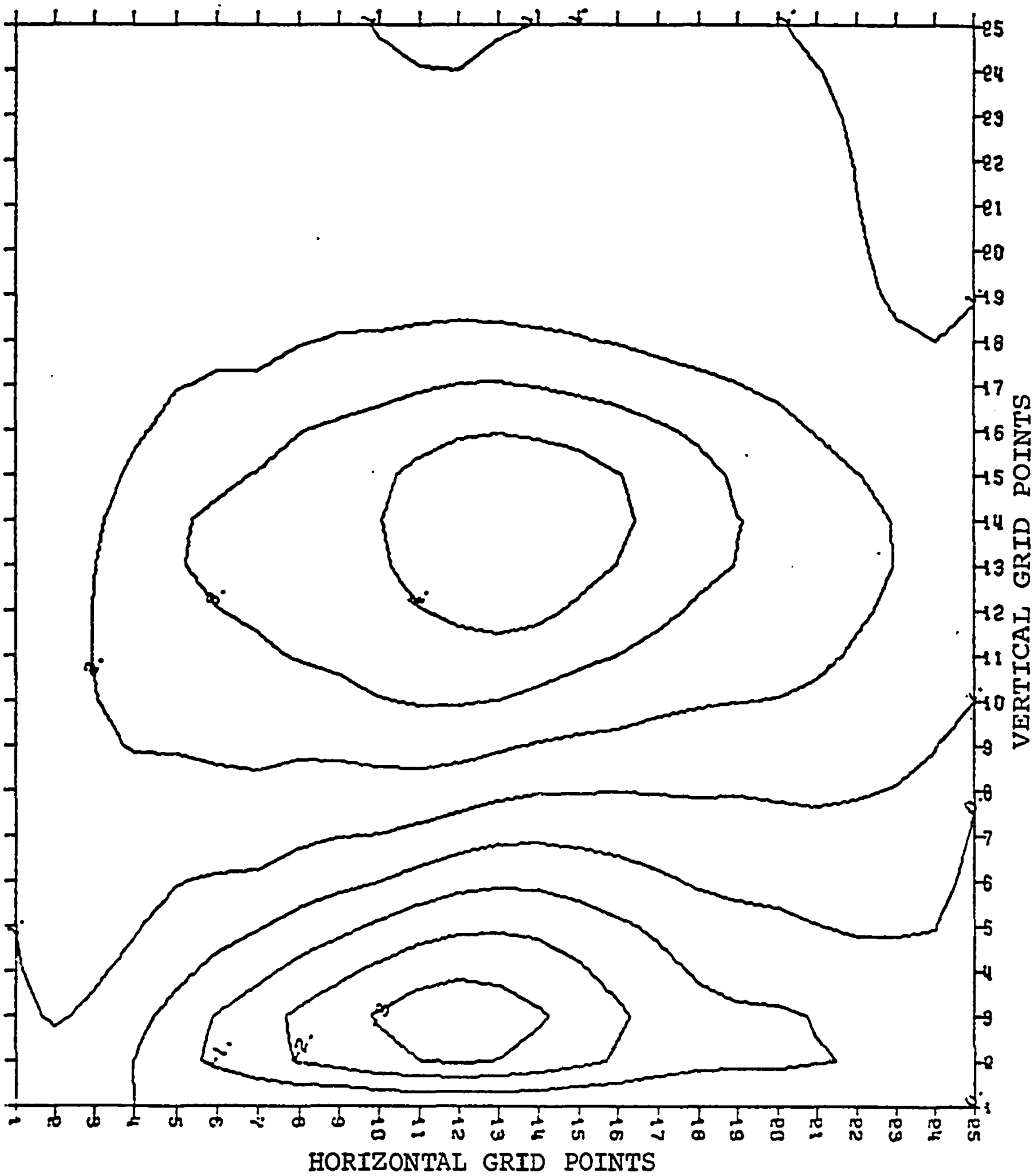

Fig. 4.1c. u-component wind at 2400 LST, Case A_1.

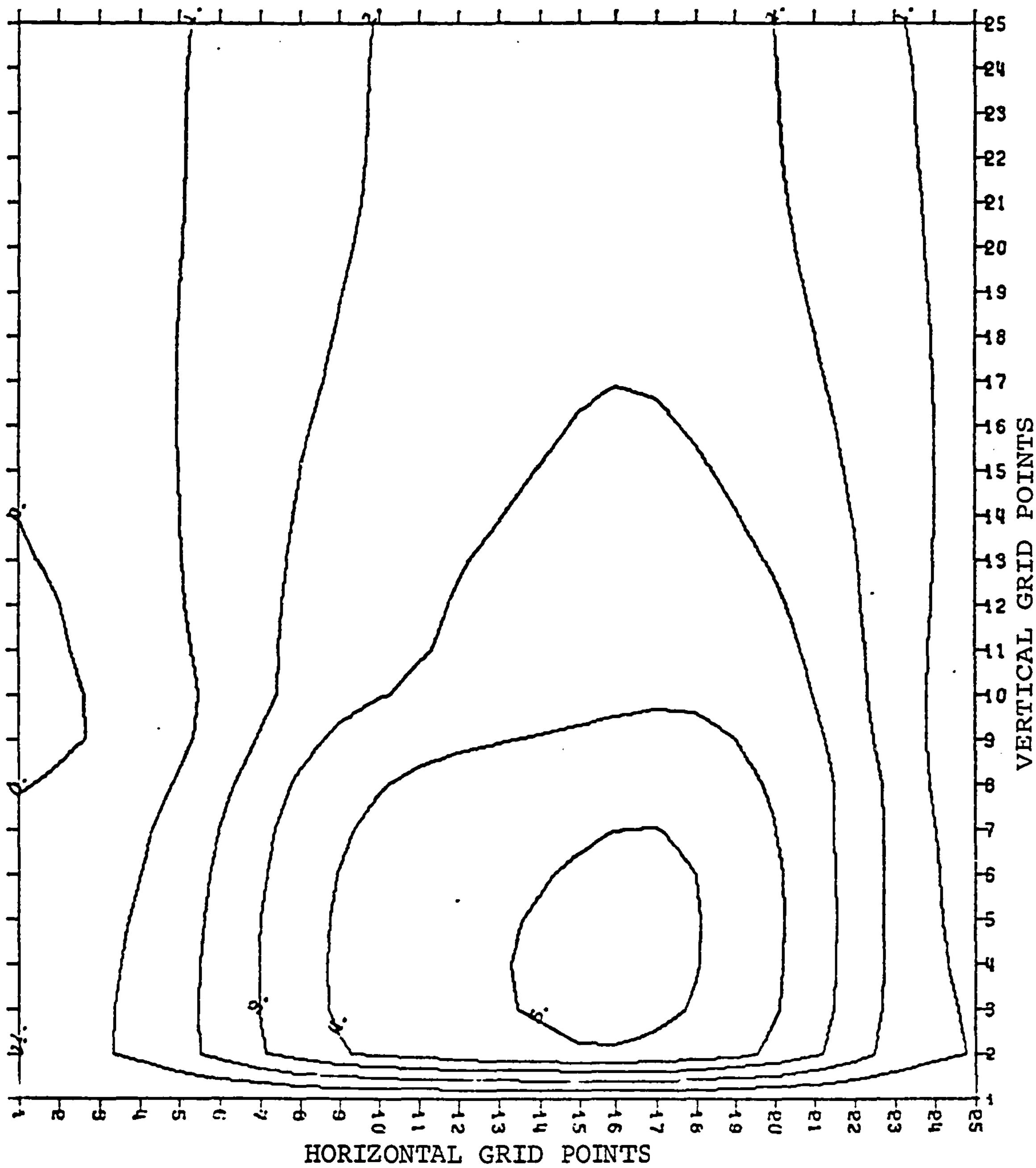

Fig. 4.2a. v-component wind (m s^{-1}) at 1200 LST, Case A_1.

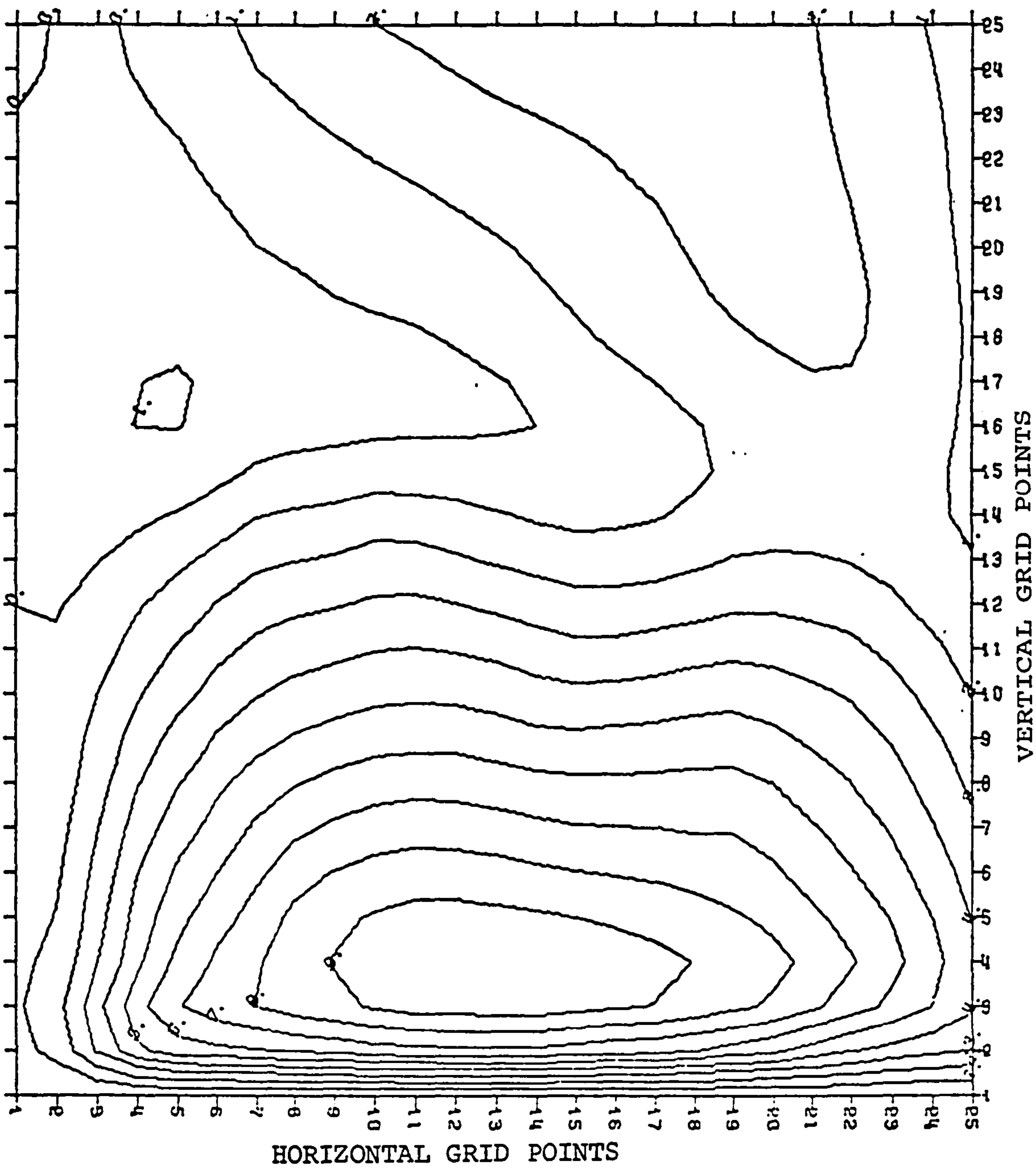

Fig. 4.2b. v-component wind at 2400 LST, Case A_1.

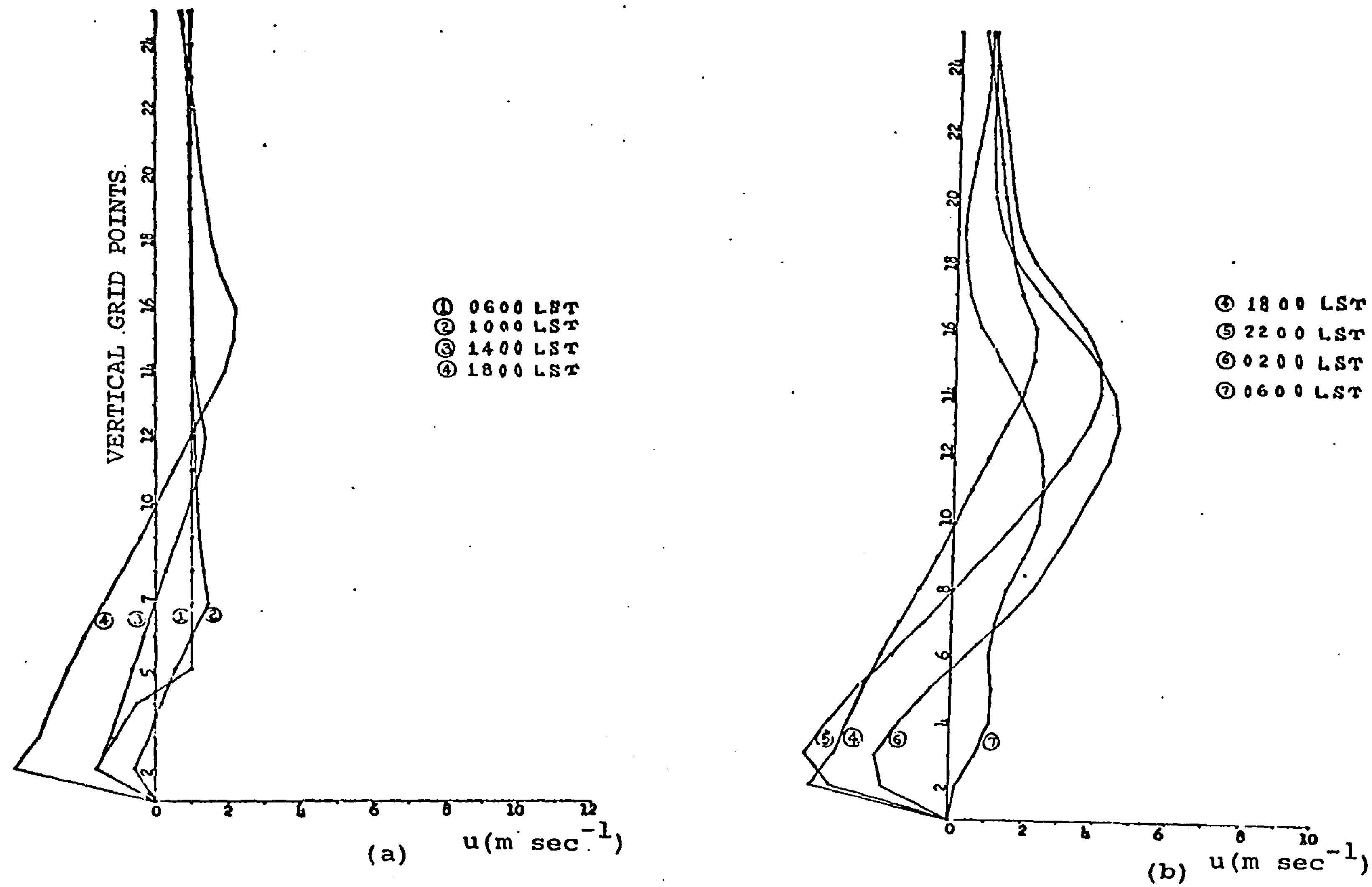

Fig. 4.3. Time variation of vertical profiles of u-component wind at middle grid point, Case A_1.

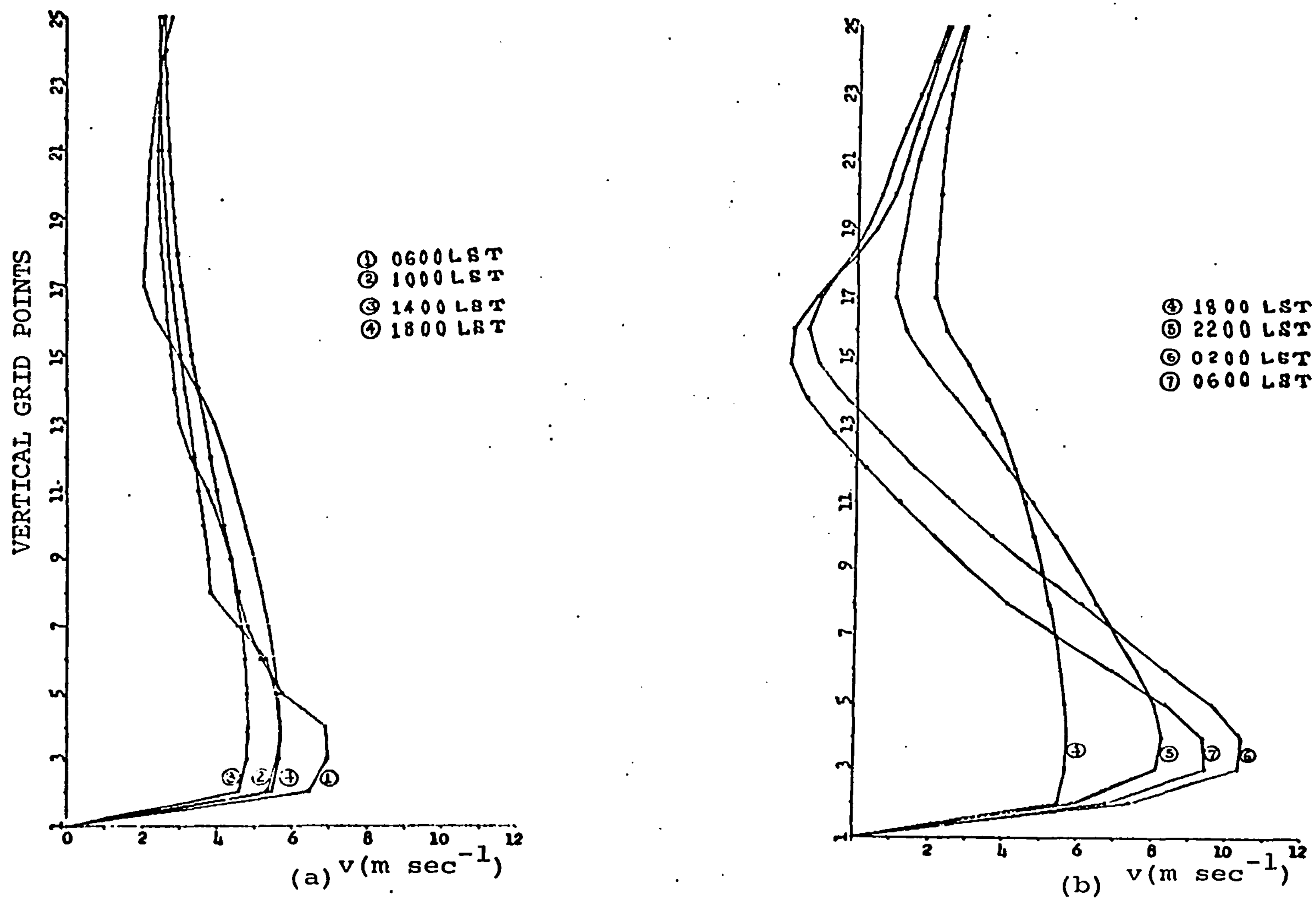

Fig. 4.4. Time variation of vertical profiles of v-component wind at middle grid point, Case A_1.

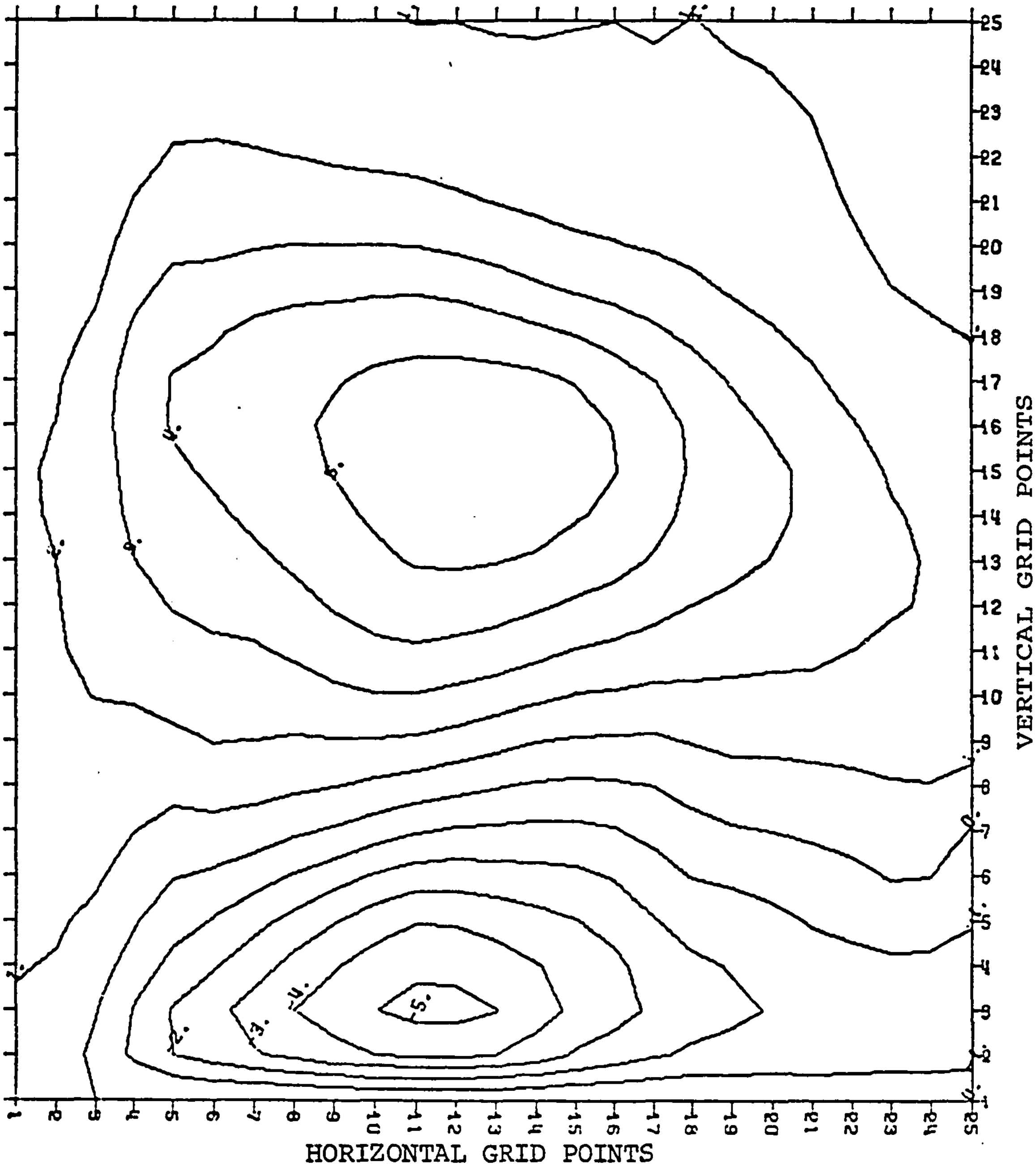

Fig. 4.5. u-component wind (m s^{-1}) at 2400 LST, Case H.

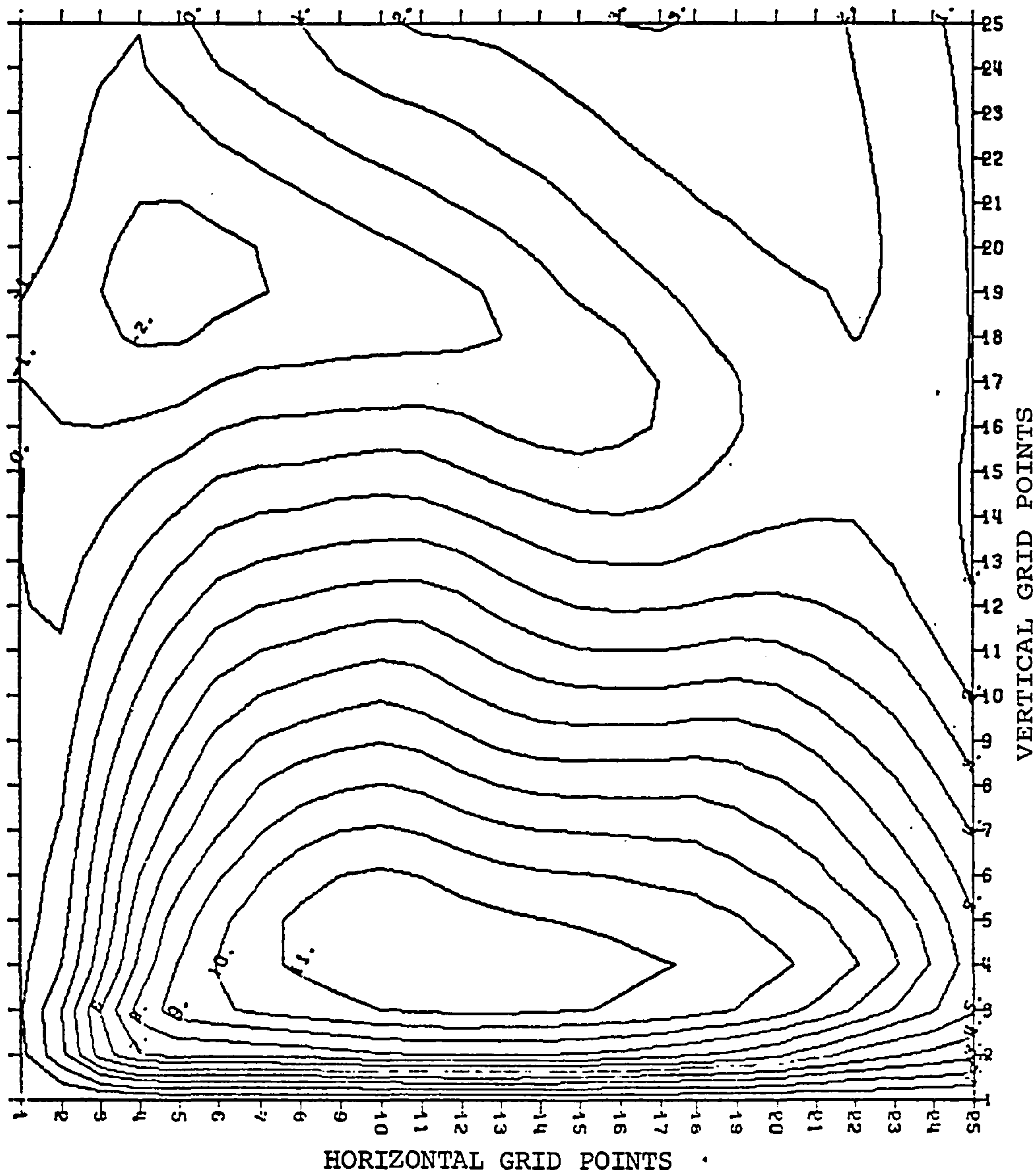

Fig. 4.6. v-component wind (m s^{-1}) at 2400 LST, Case H.

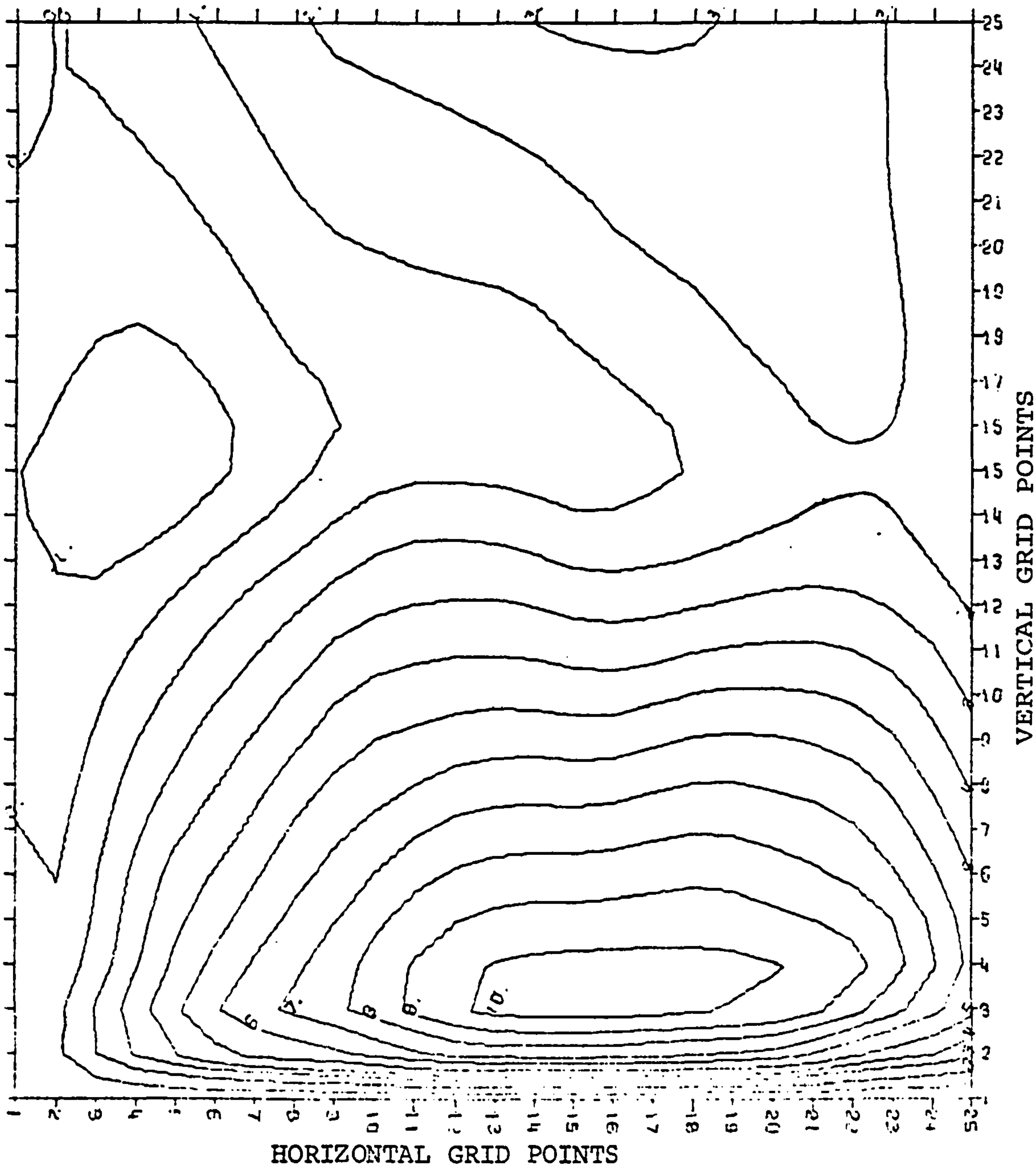

Fig. 4.7. v-component wind at 2400 LST, Case I.

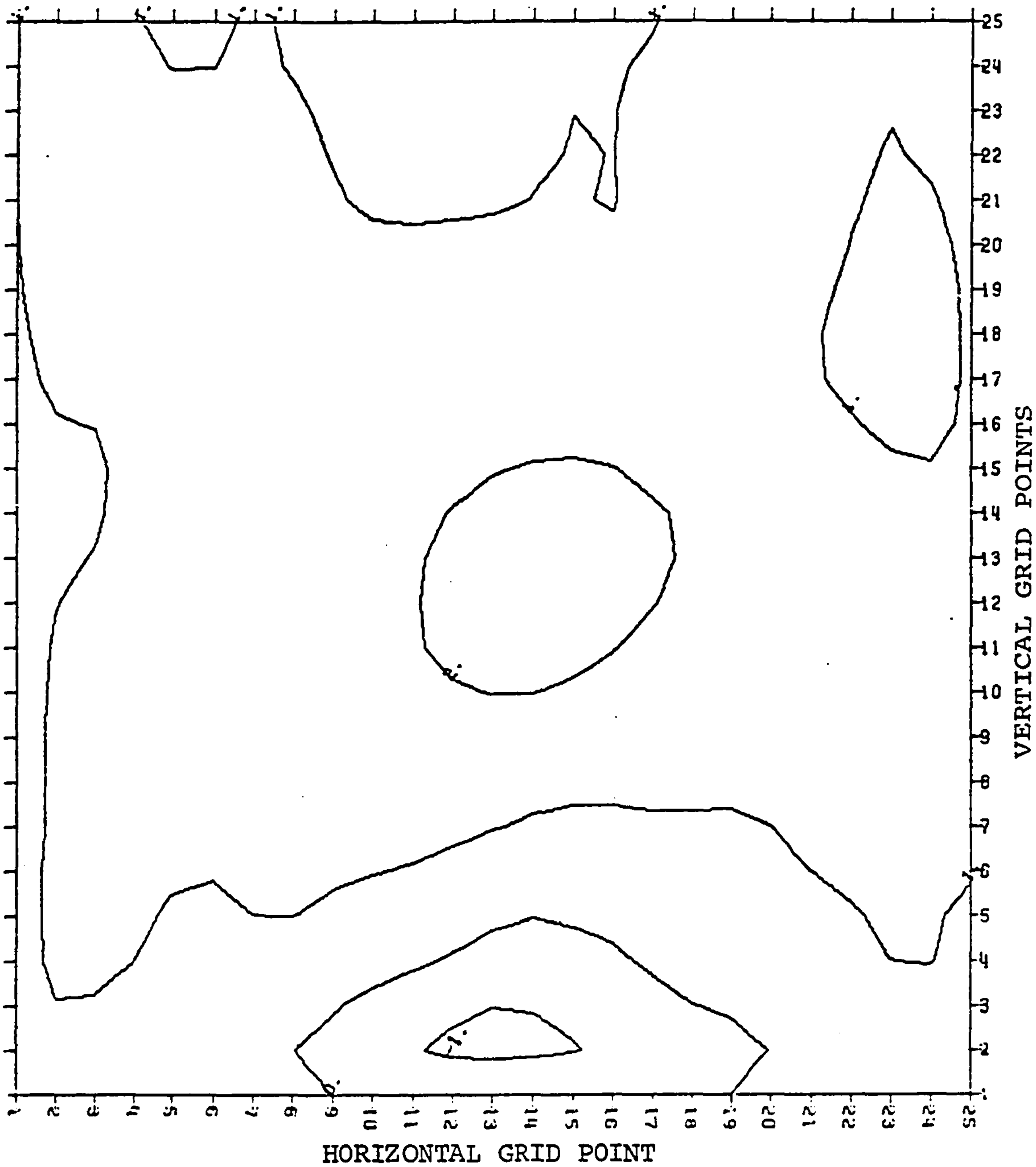

Fig. 4.8. u-component wind at 2400 LST, Case E.

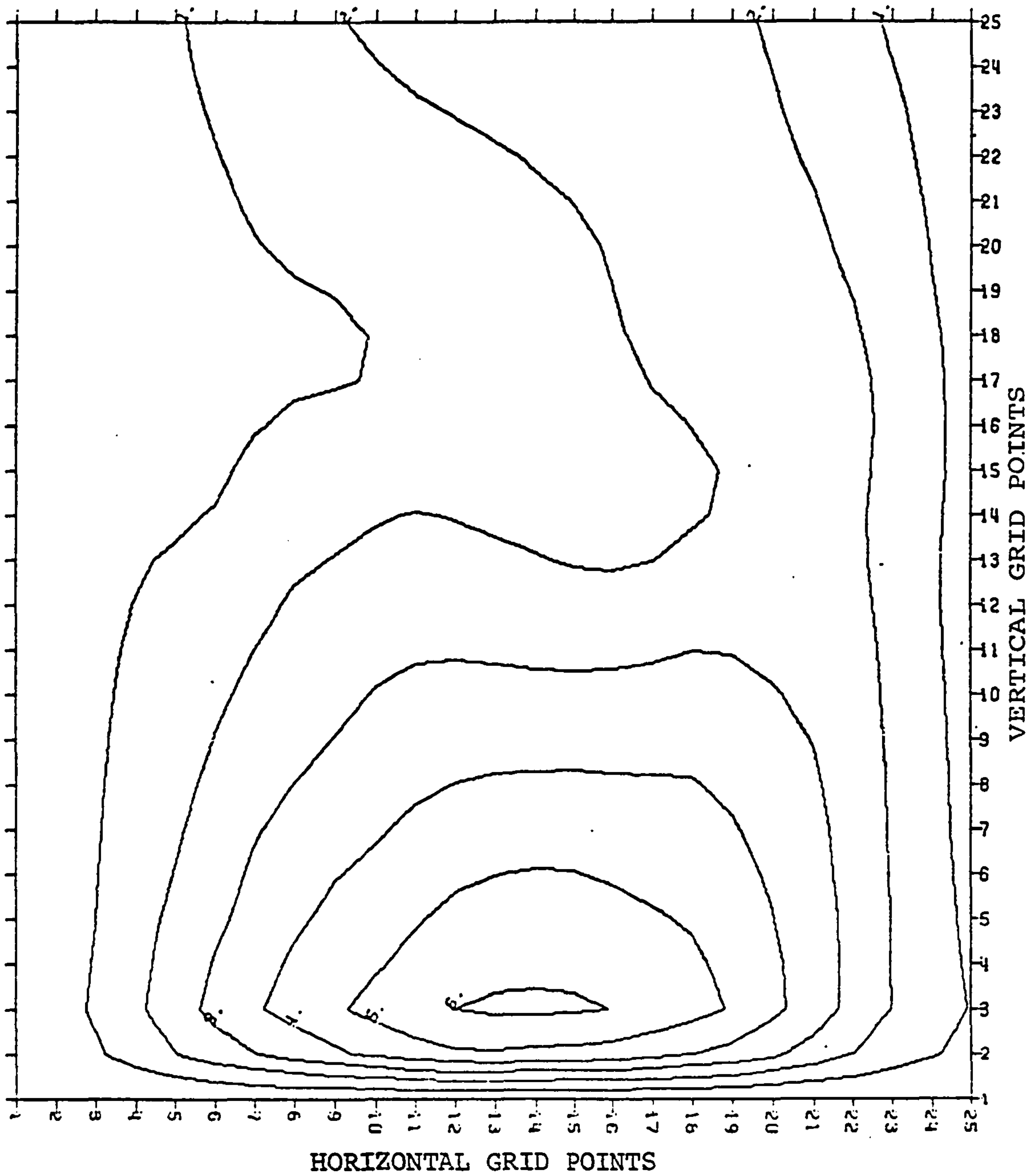

Fig. 4.9. v-component wind at 2400 LST, Case E.

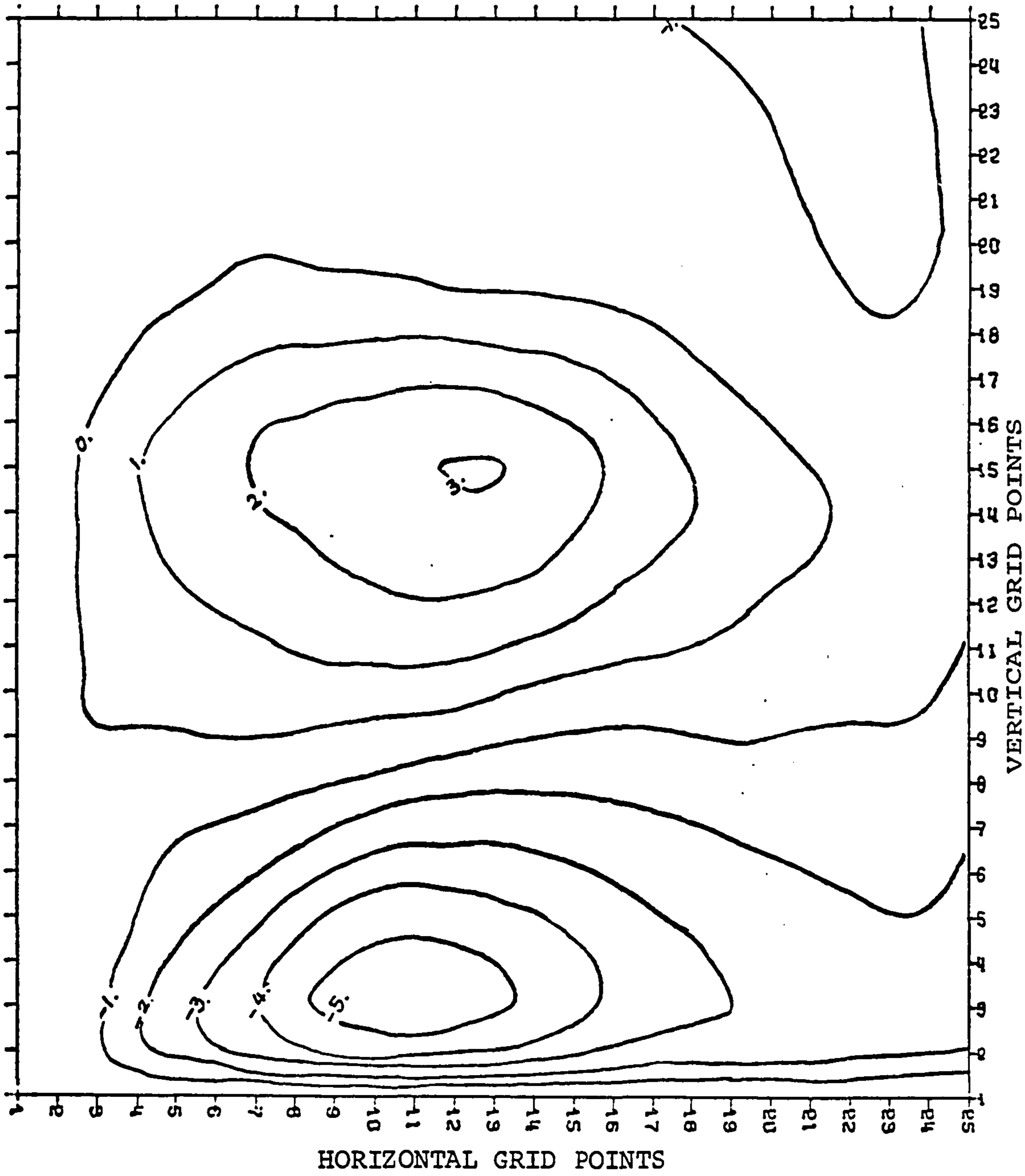

Fig. 4.10. u-component wind at 2400 LST, Case G.

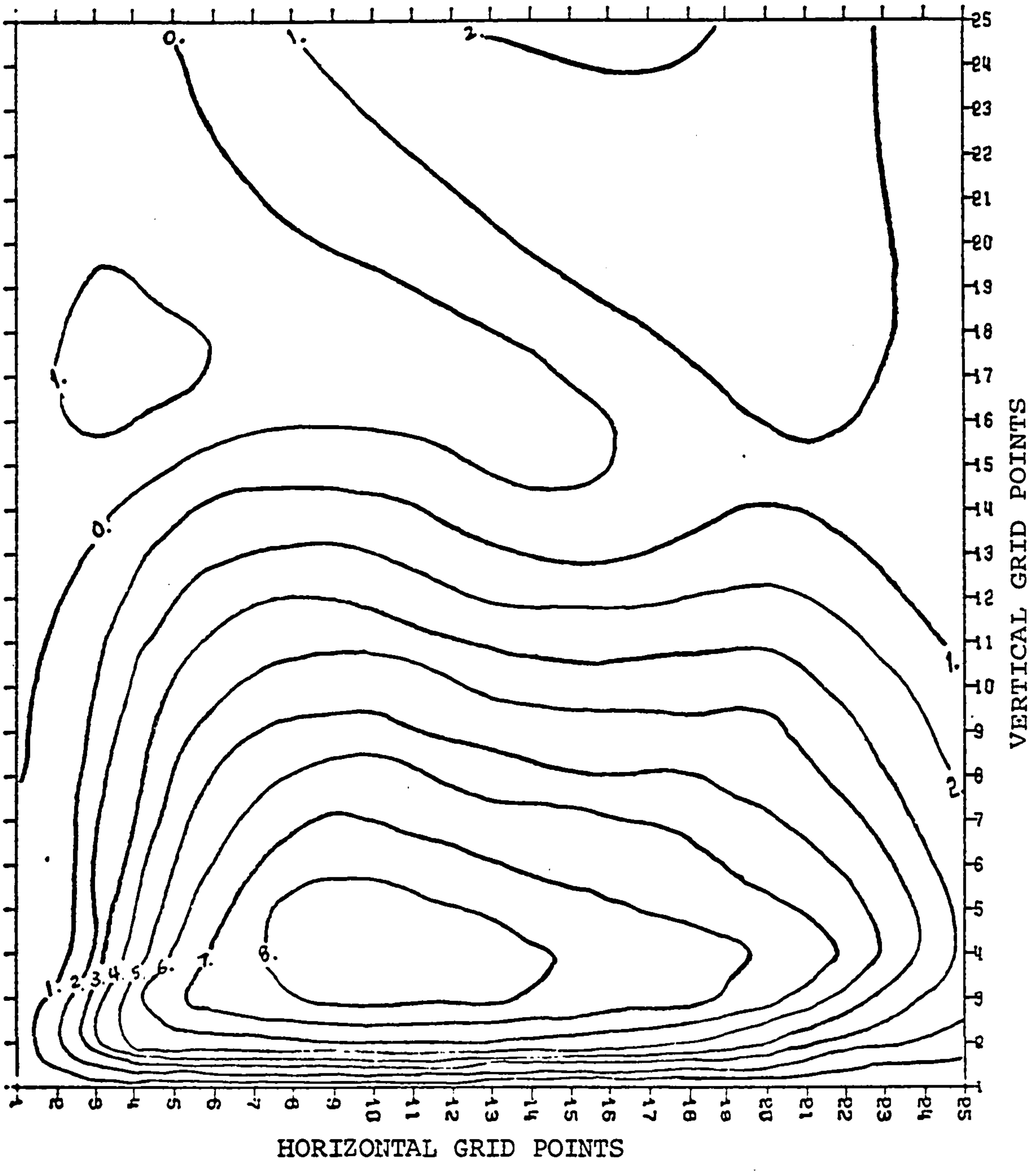

Fig. 4.11. v-component wind at 2400 LST, Case G.

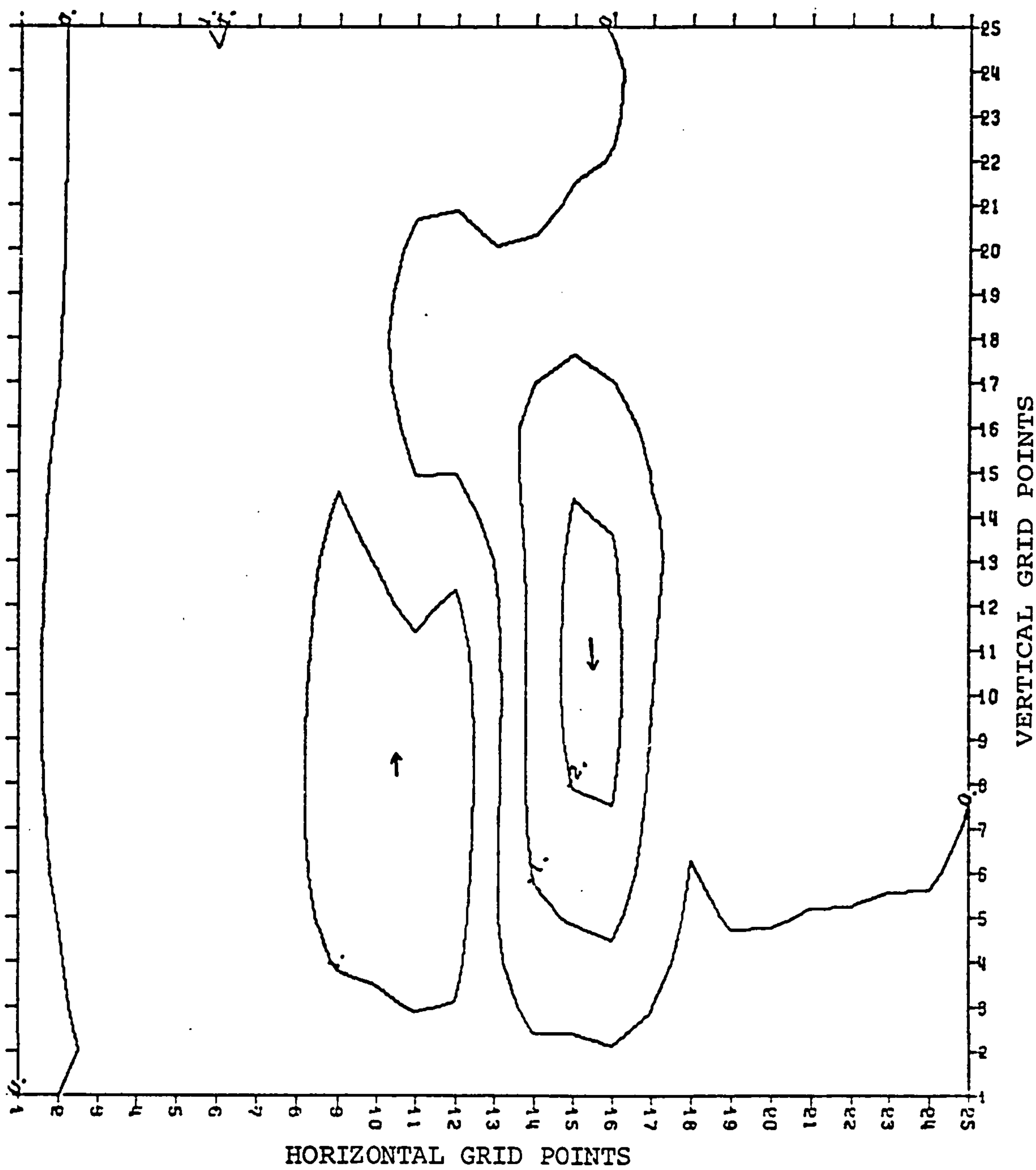

Fig. 4.12a. Vertical motion (cm sec^{-1}) at 2000 LST, Case A_1.

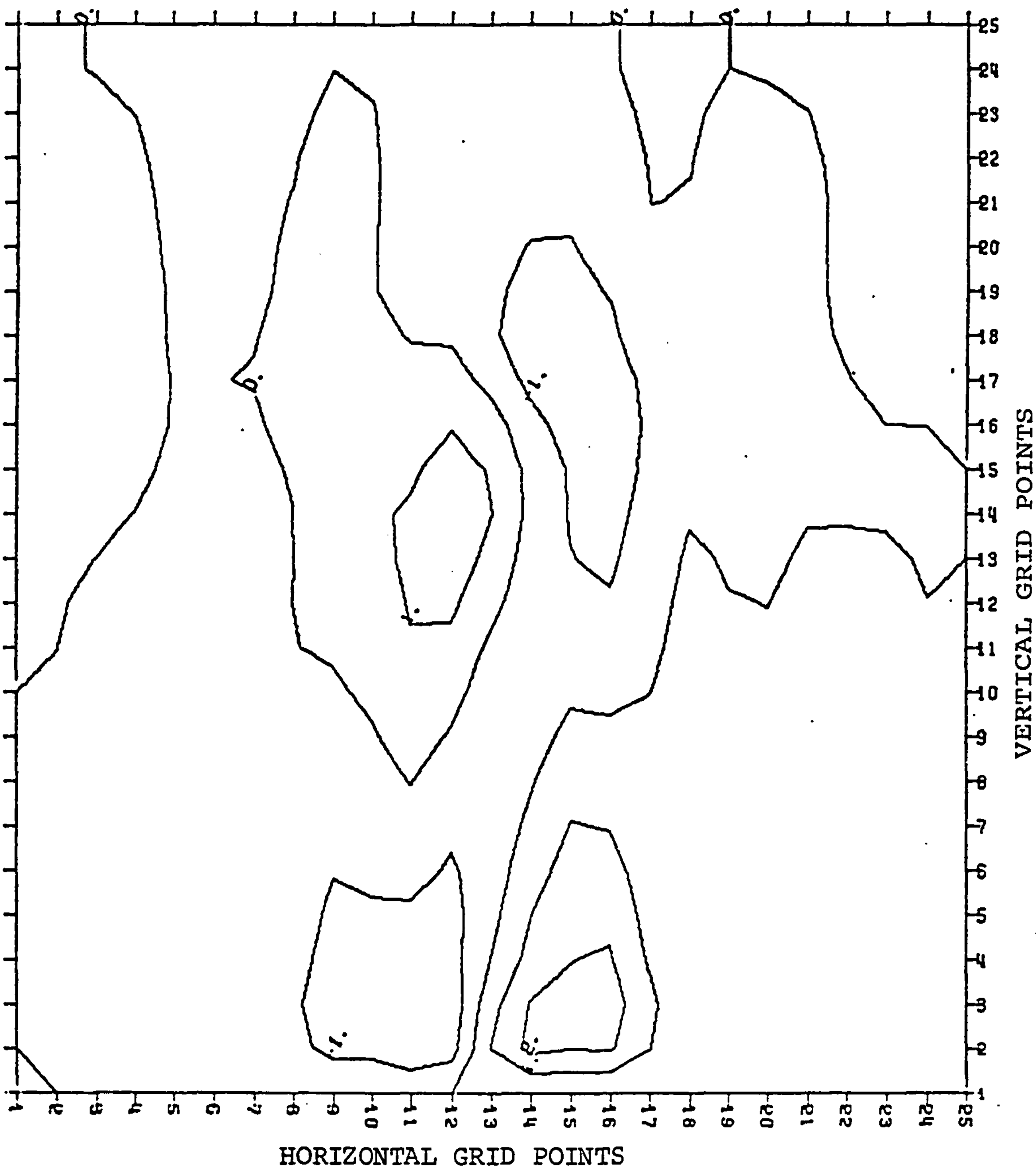

Fig. 4.12b. Divergence (10^{-5} sec^{-1}) at 2000 LST, Case A_1.

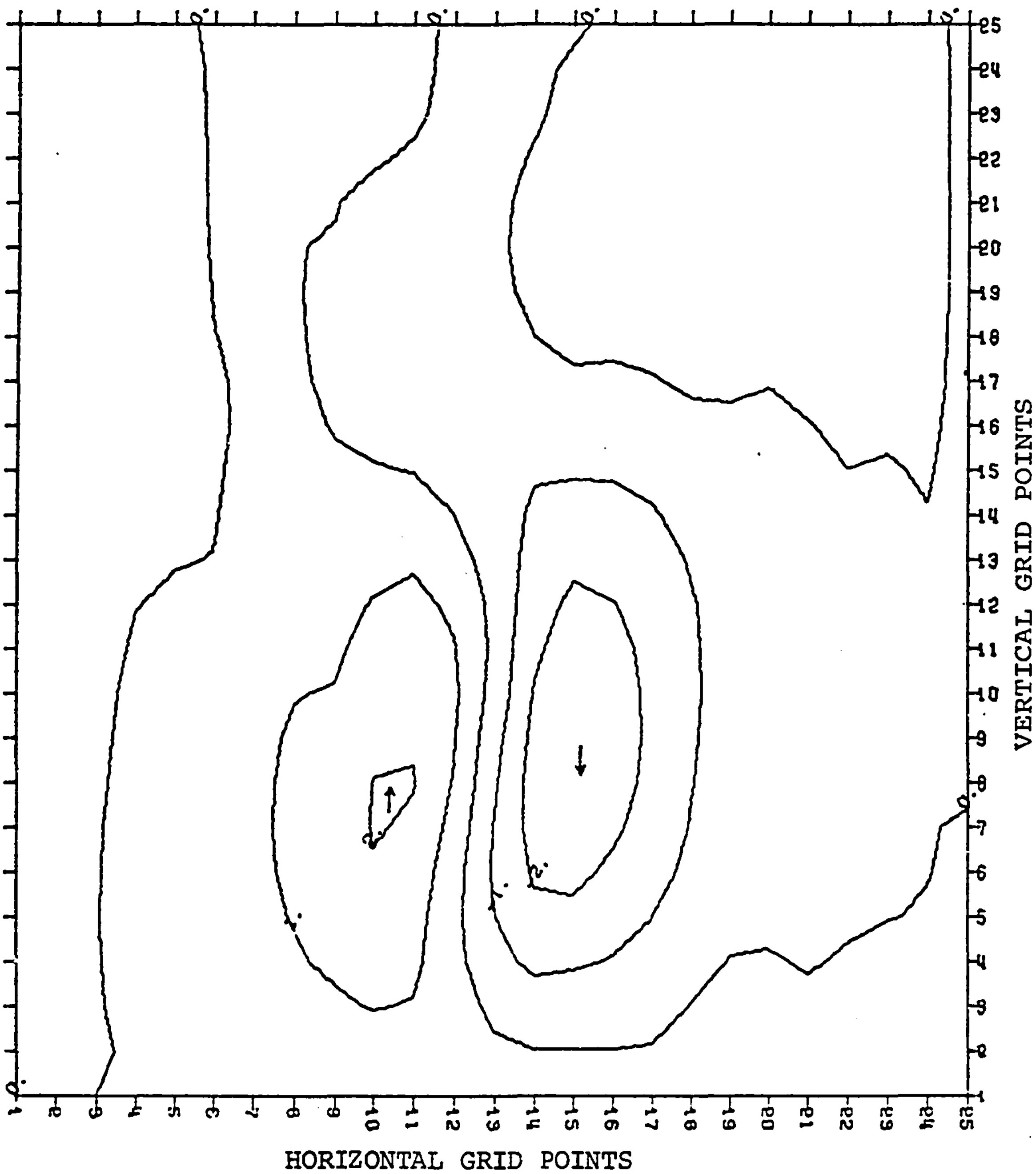

Fig. 4.13a. Vertical motion (cm sec^{-1}) at 2400 LST, Case A_1.

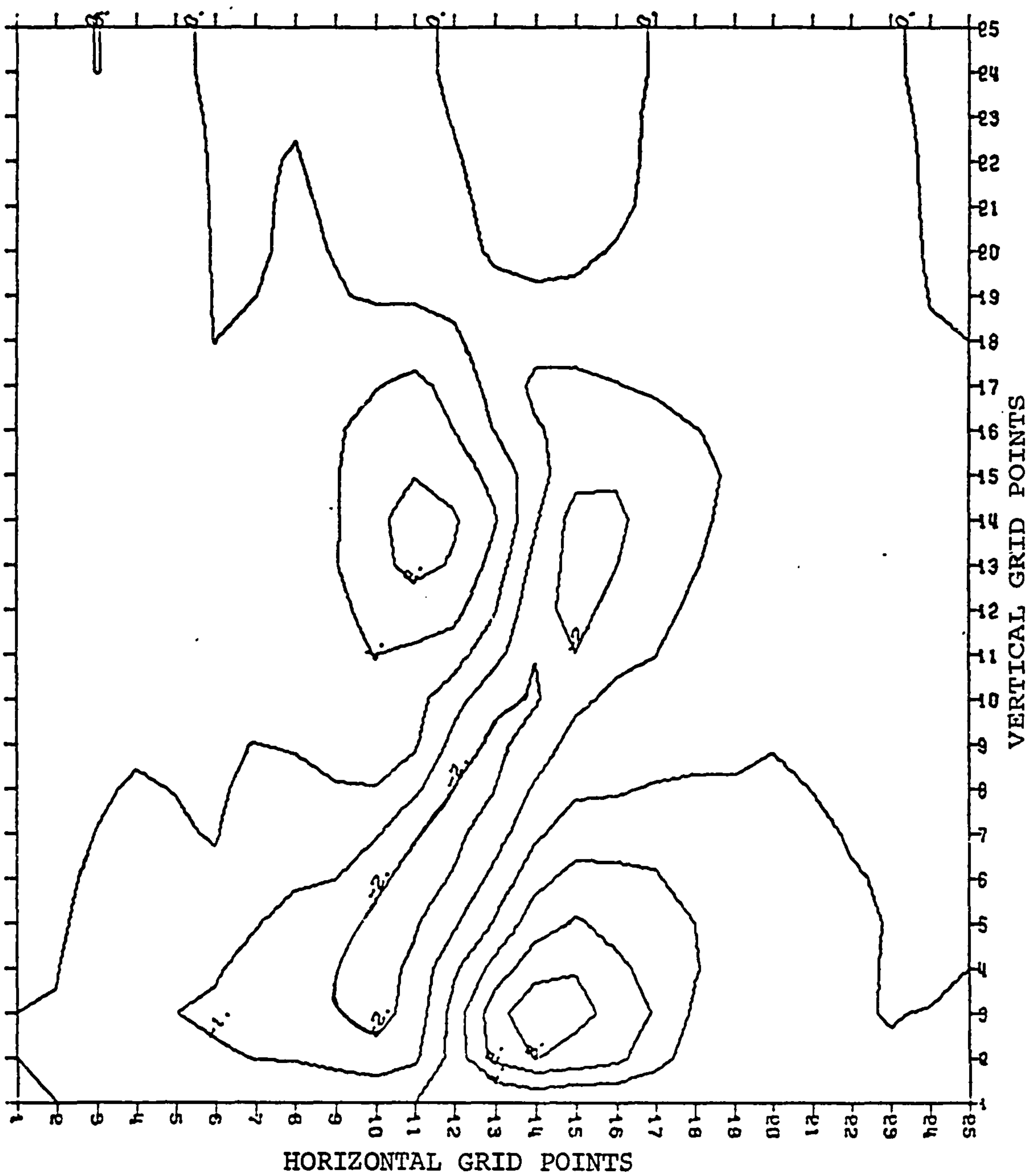

Fig. 4.13b. Divergence (10^{-5} sec^{-1}) at 2400 LST, Case A_1.

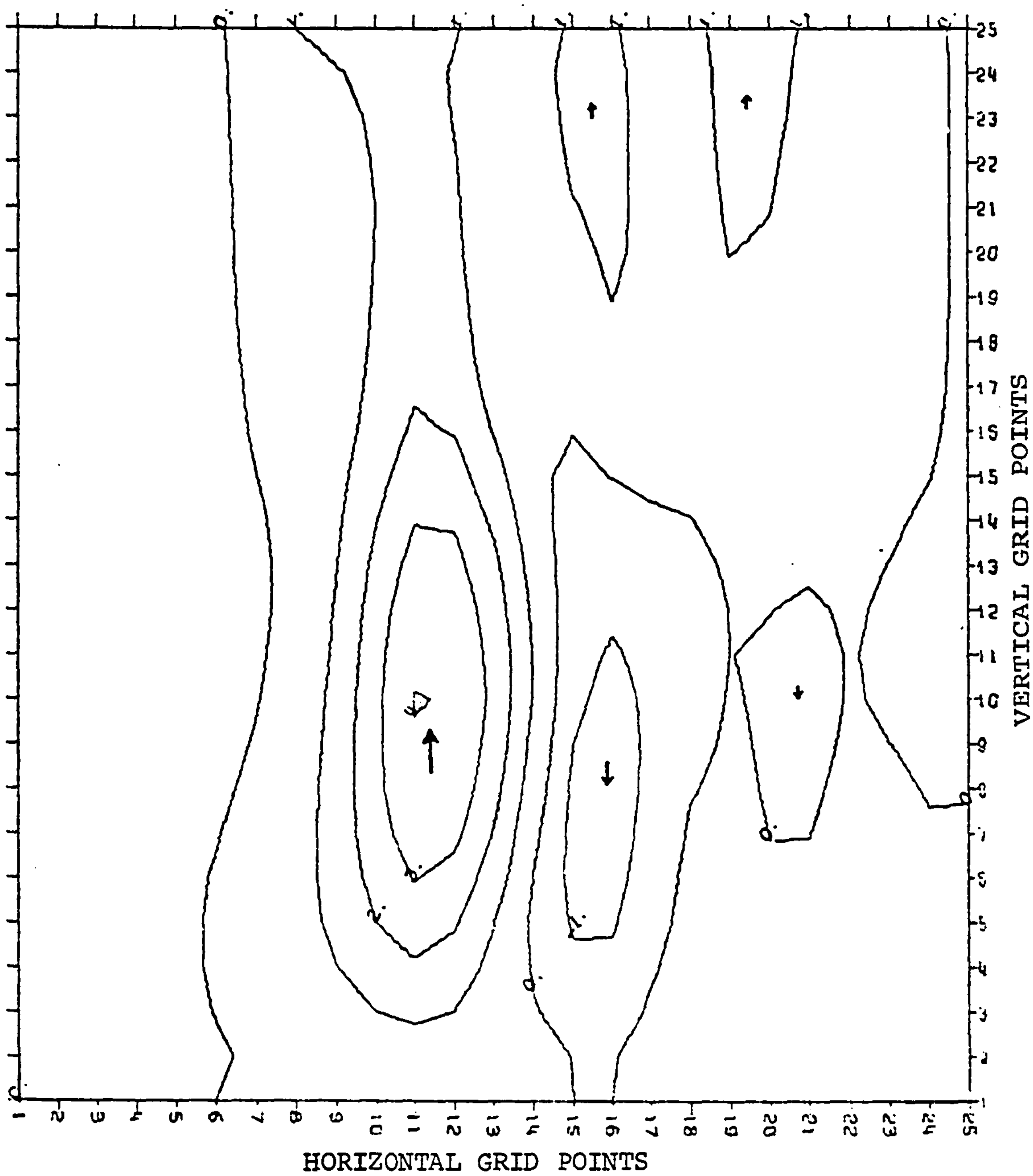

Fig. 4.14a. Vertical motion (cm sec^{-1}) at 2400 LST, Case I.

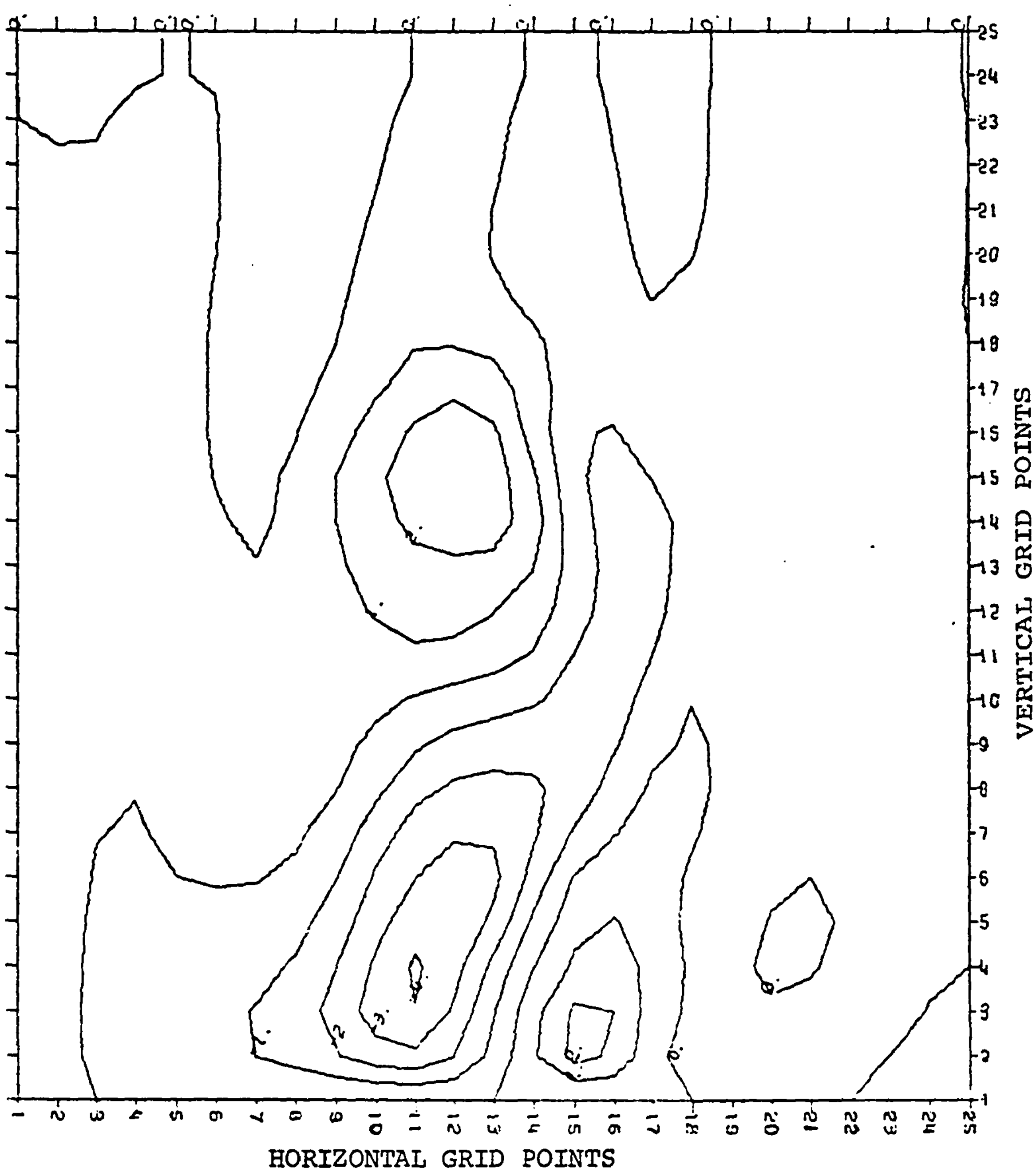

Fig. 4.14b. Divergence (10^{-5} sec^{-1}) at 2400 LST, Case I.

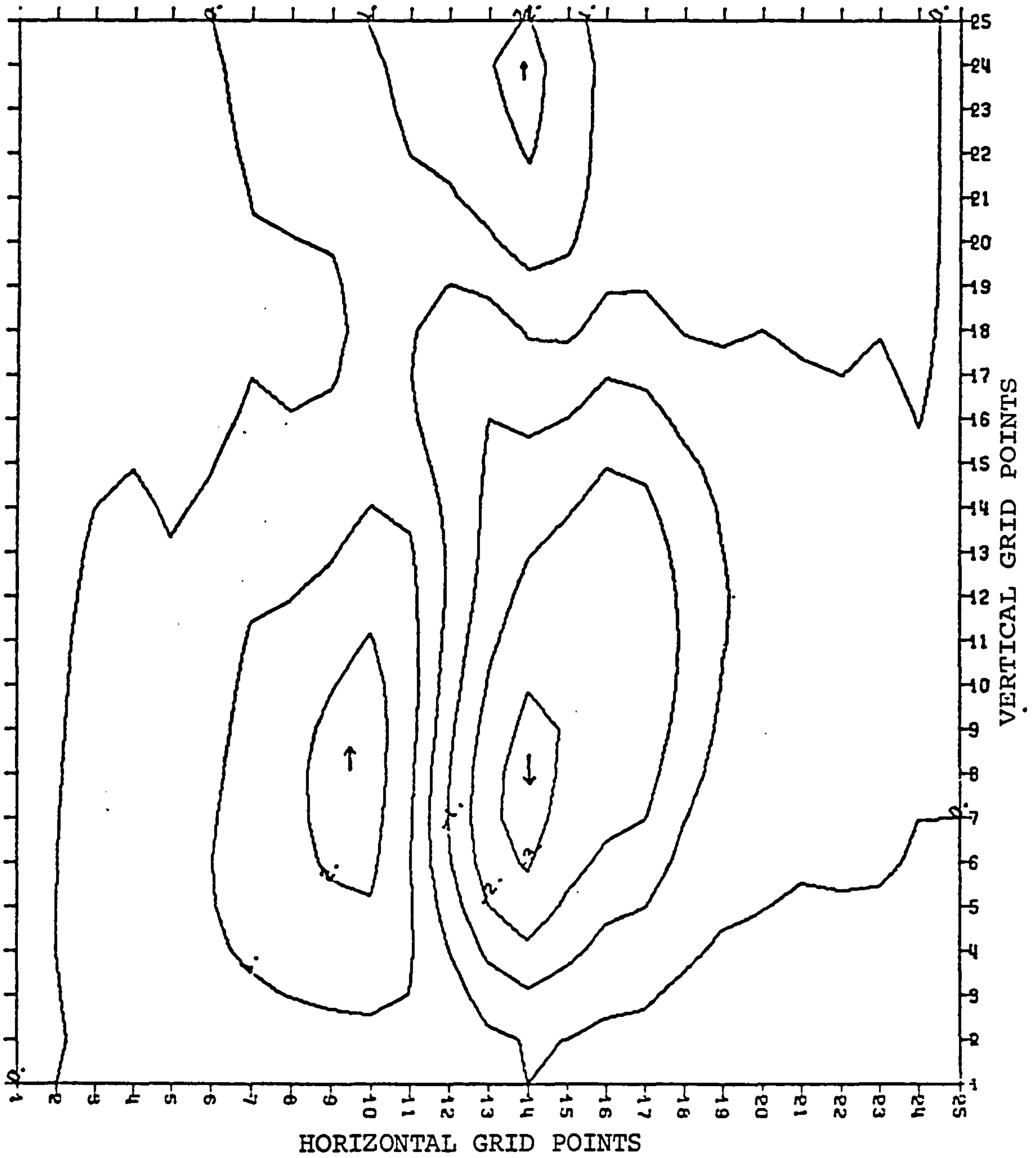

Fig. 4.15a. Vertical motion (cm sec^{-1}) at 2400 LST, Case H.

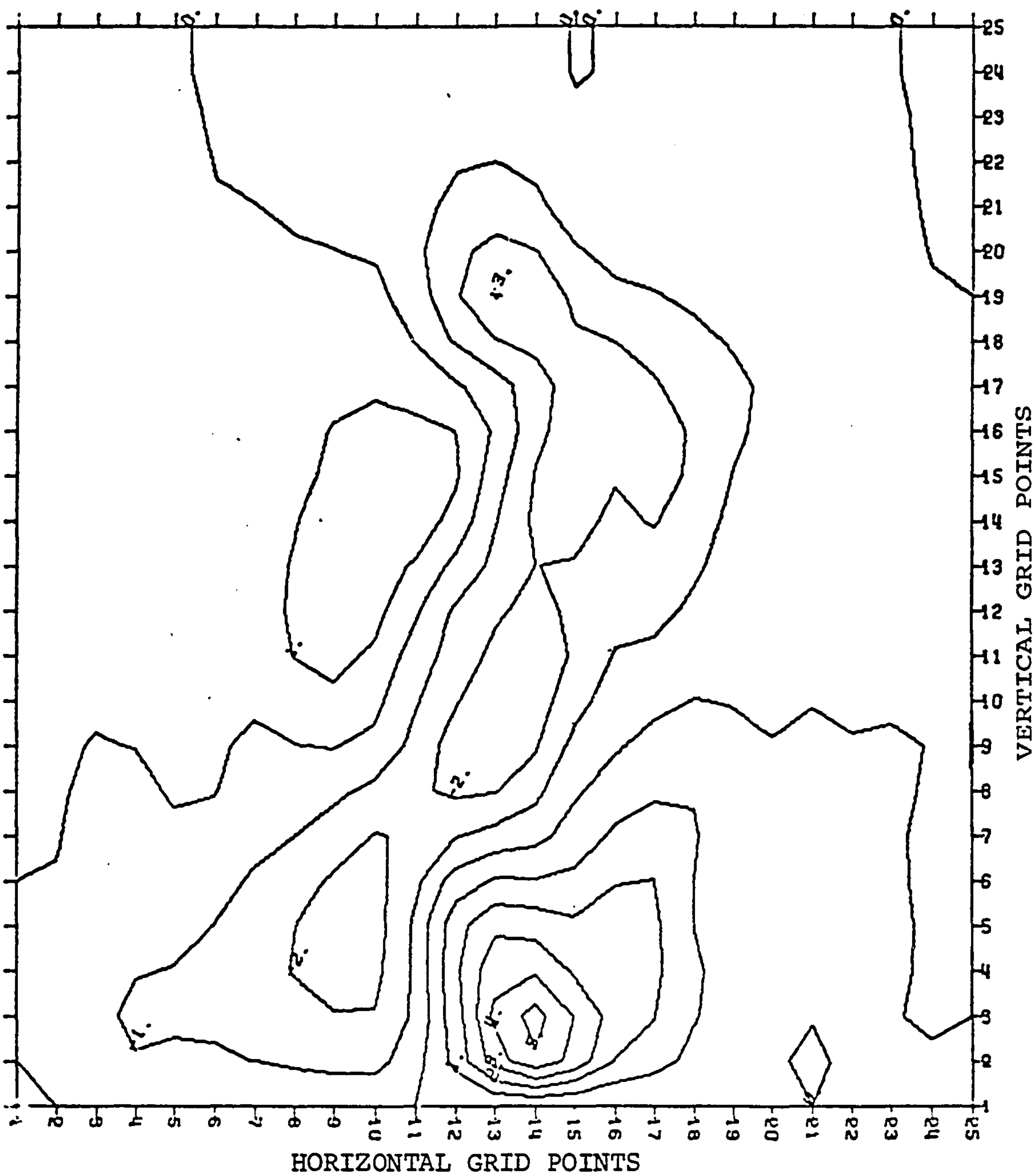

Fig. 4.15b. Divergence (10^{-5} sec^{-1}) at 2400 LST, Case H.

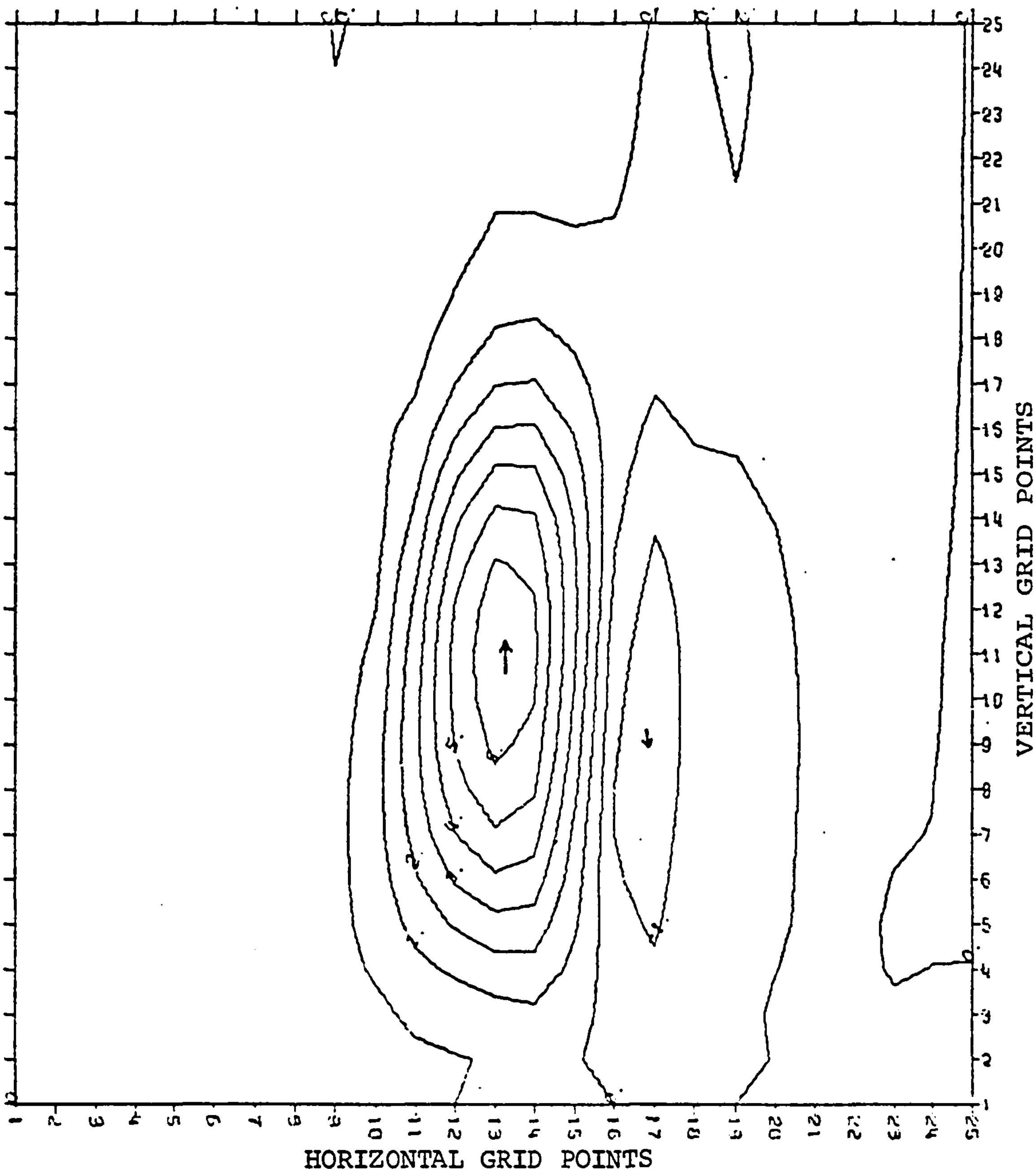

Fig. 4.16a. Vertical motion (cm sec^{-1}) at 0400 LST, Case I.

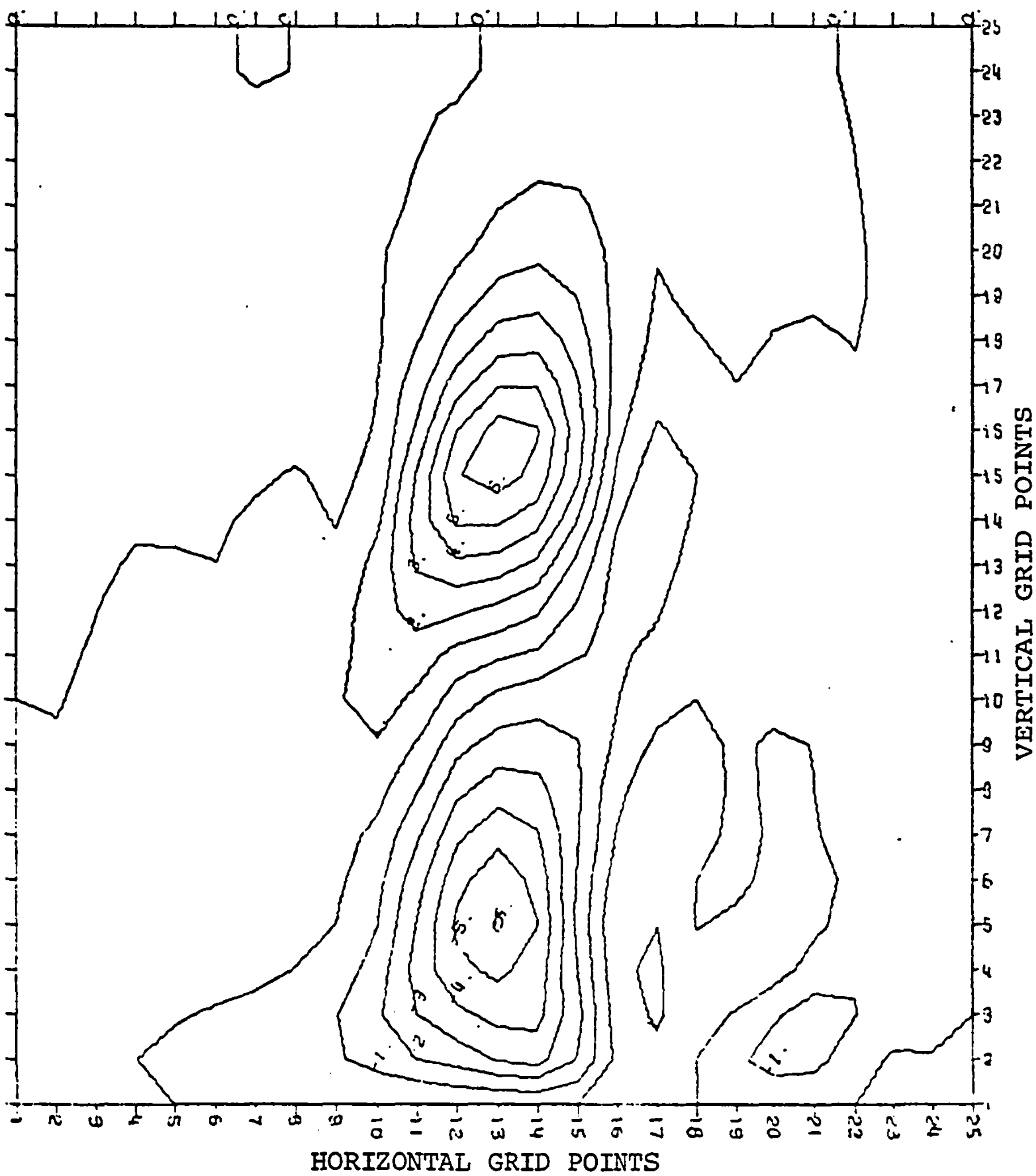

Fig. 4.16b. Divergence (10^{-5} sec^{-1}) at 0400 LST, Case I.

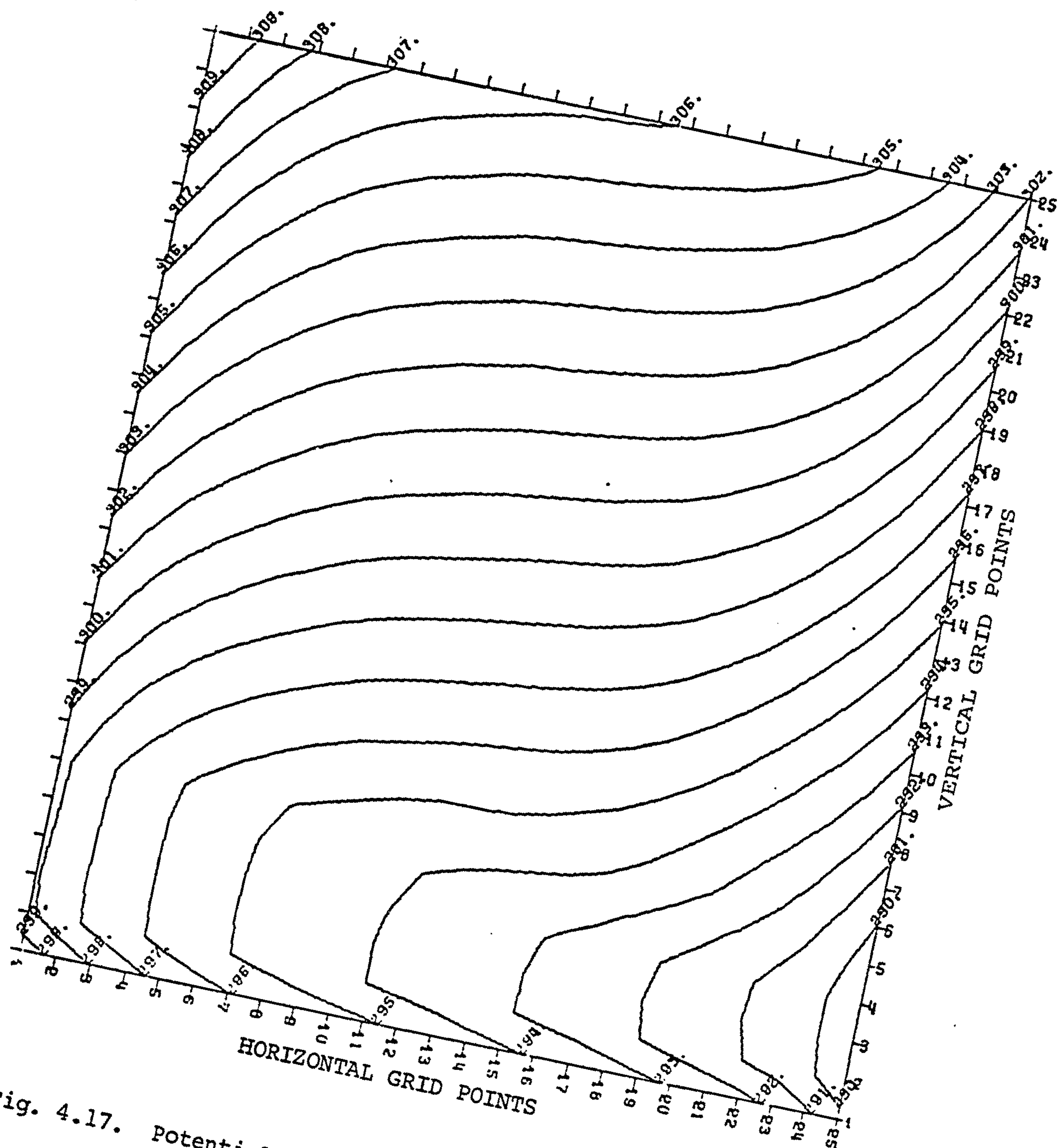

Fig. 4.17. Potential temperature (°K) at 0800 LST, Case A_1.

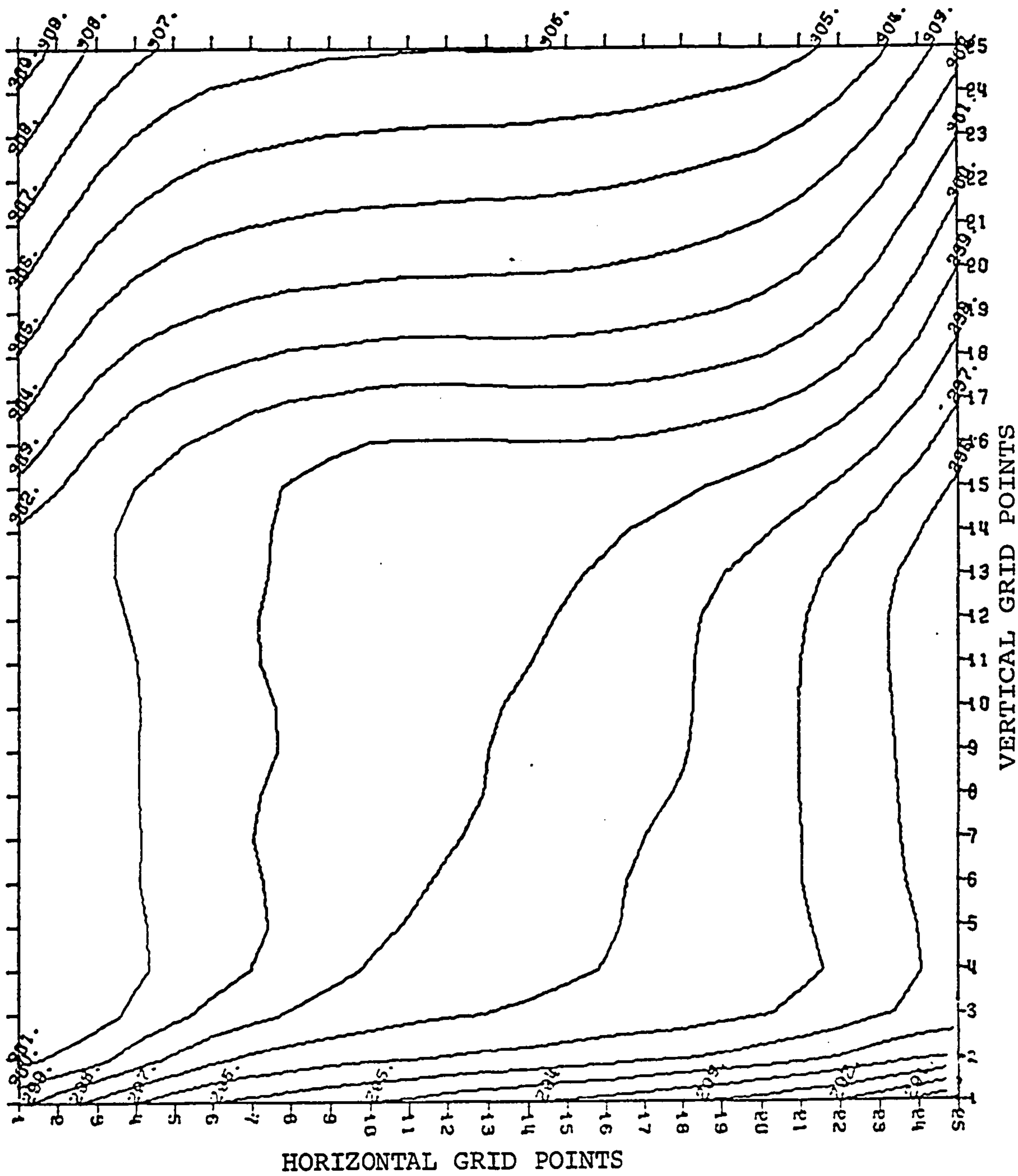

Fig. 4.18. Potential temperature ($^{\circ}$K) at 2400 LST, Case A_1.

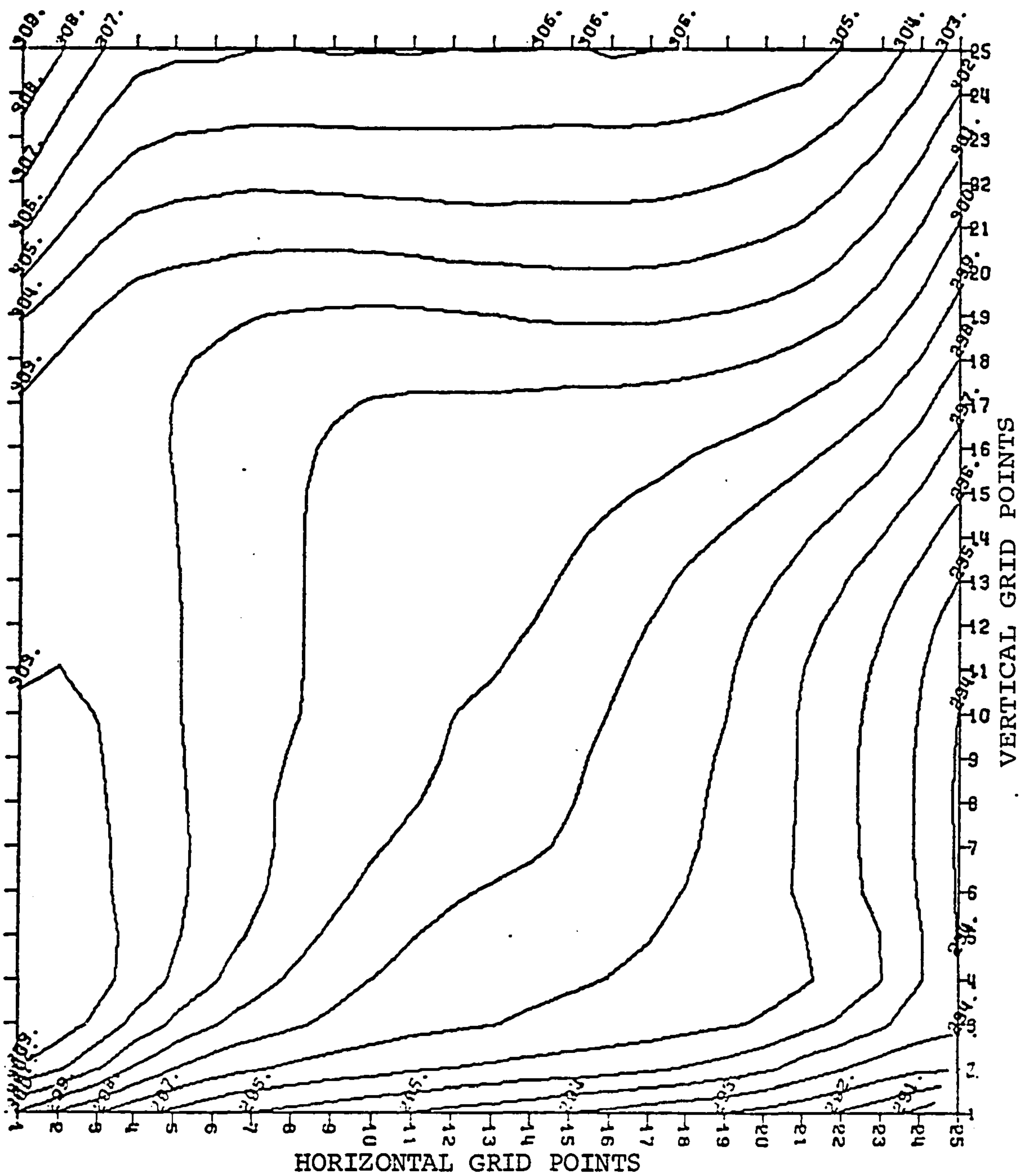

Fig. 4.19. Potential temperature (°K) at 2400 LST, Case H.

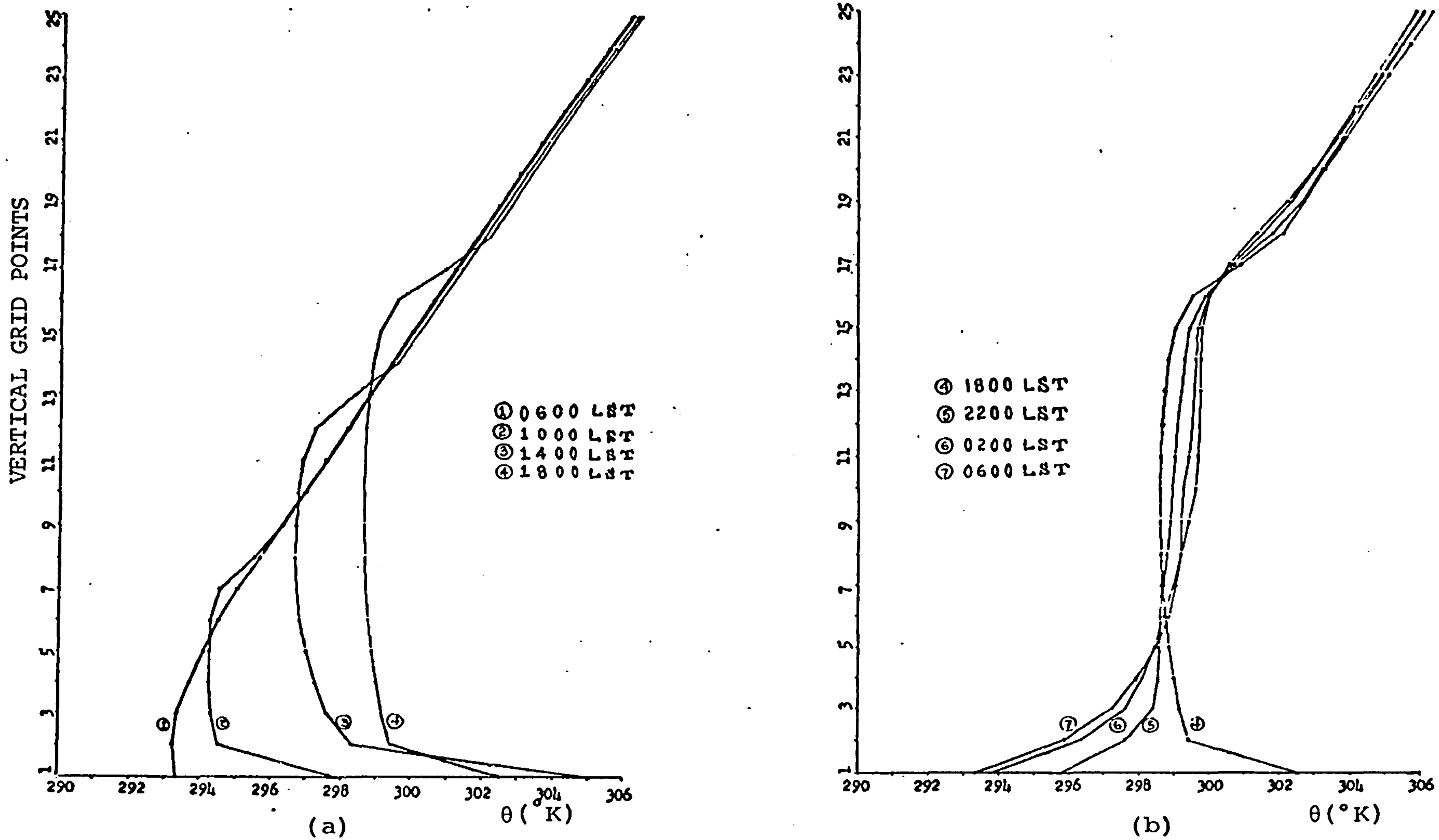

Fig. 4.20. Time variation of potential-temperature profiles at middle grid point, Case A_1.

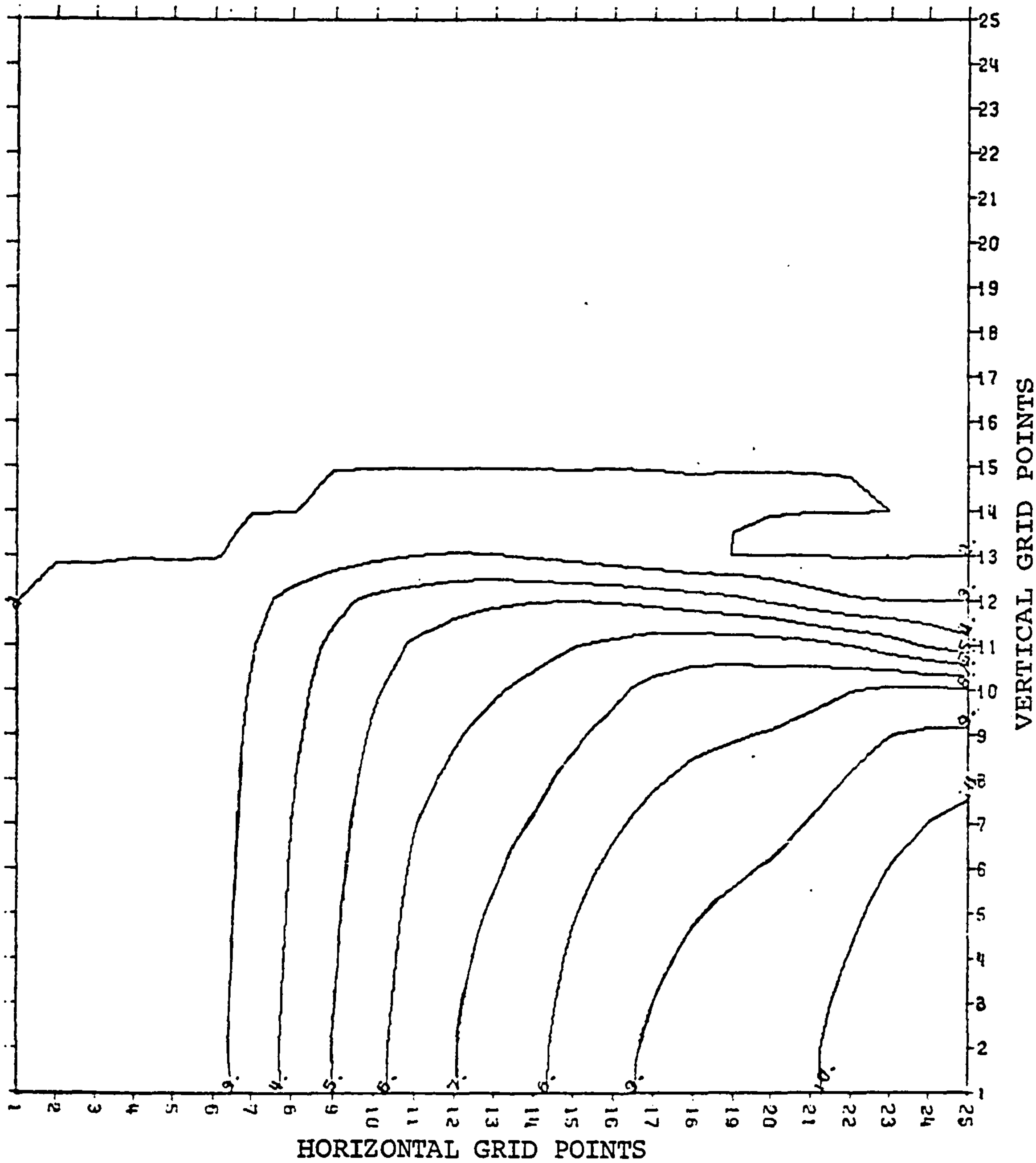

Fig. 4.21. Specific humidity (g kg^{-1}) at 1400 LST, Case A_2.

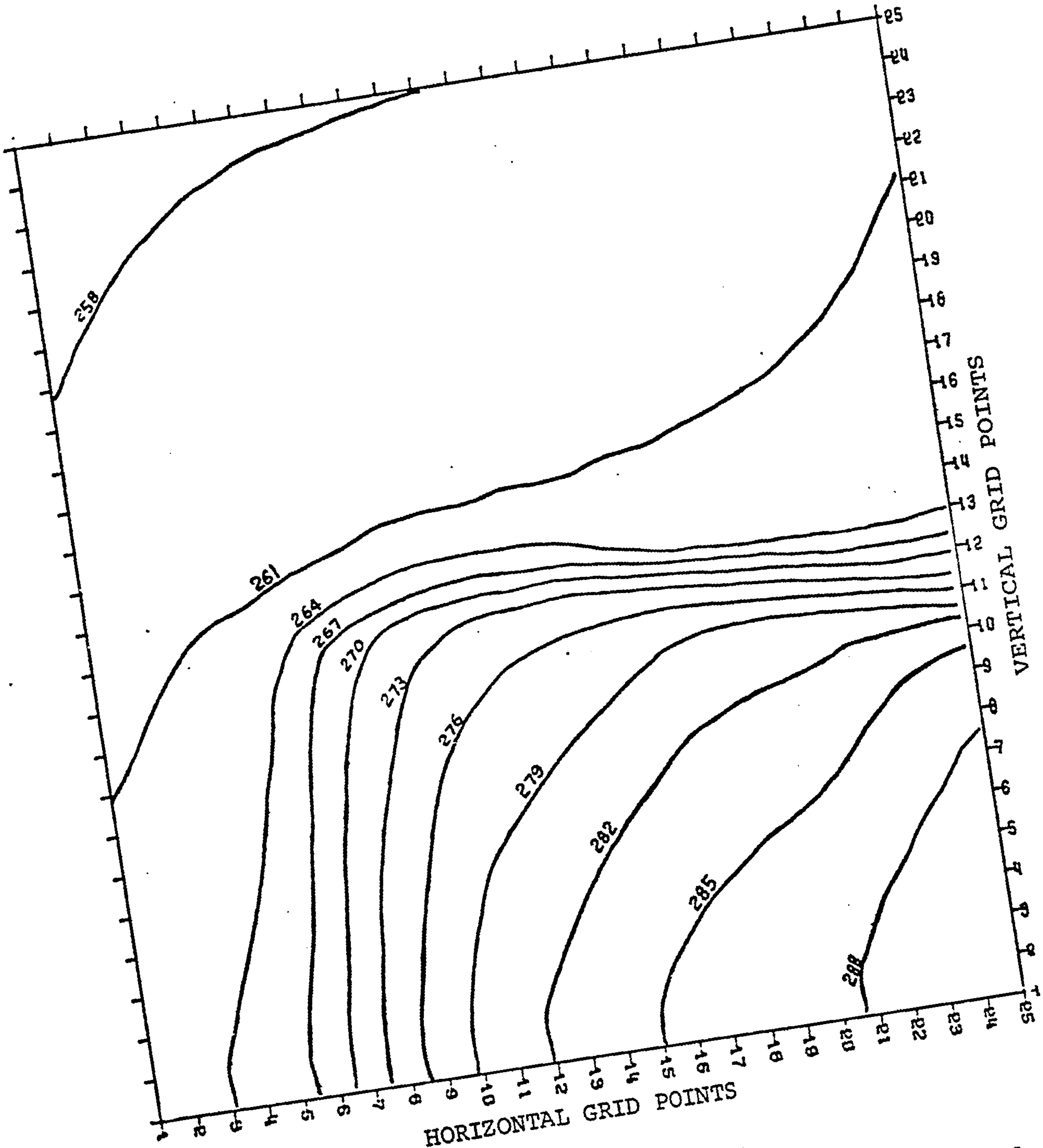

4.22

Fig. 4.22. Dew-point temperature (°K) at 1400 LST, Case A_2.

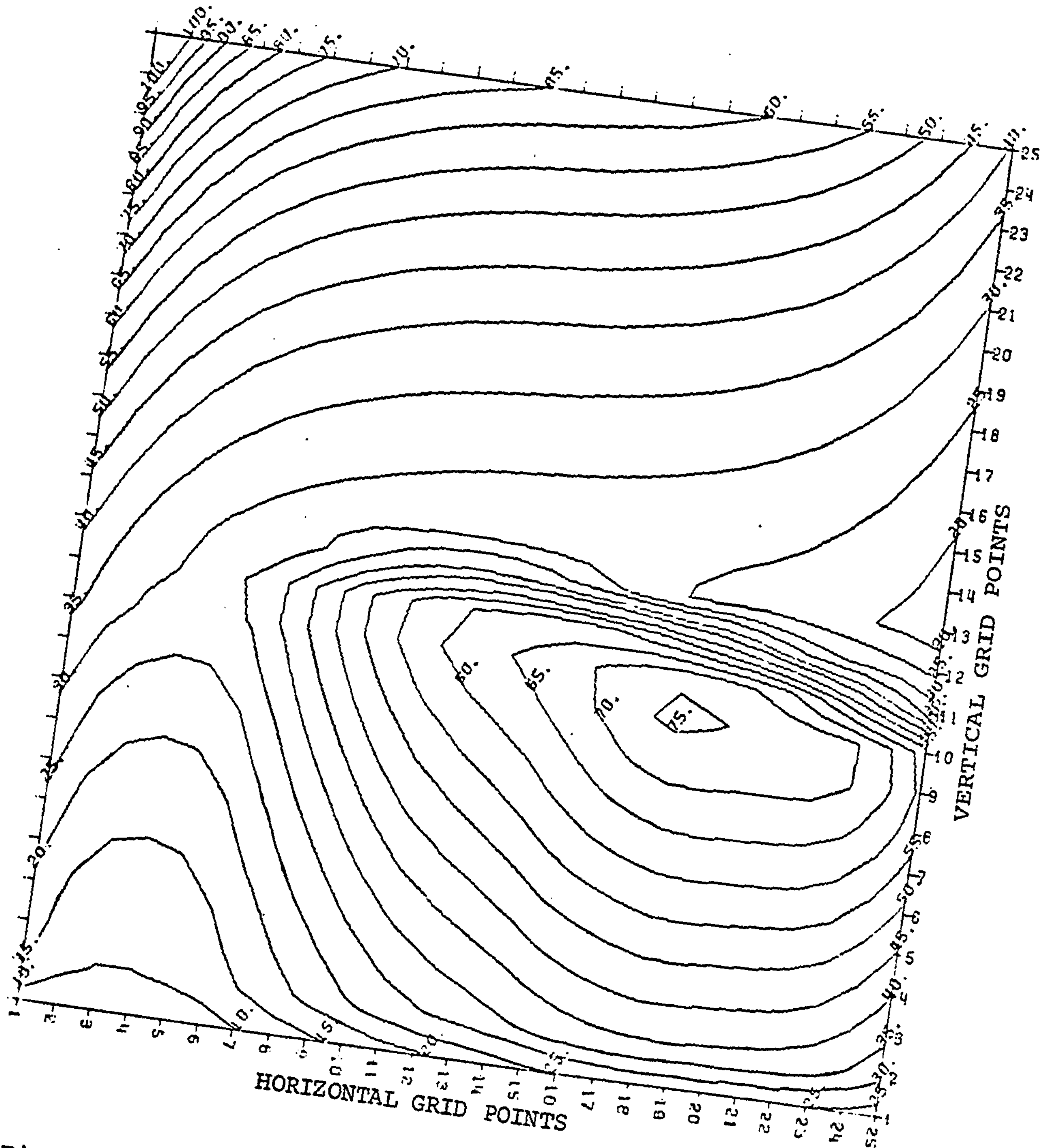

Fig. 4.23. Relative humidity (%) at 1400 LST, Case A_2.

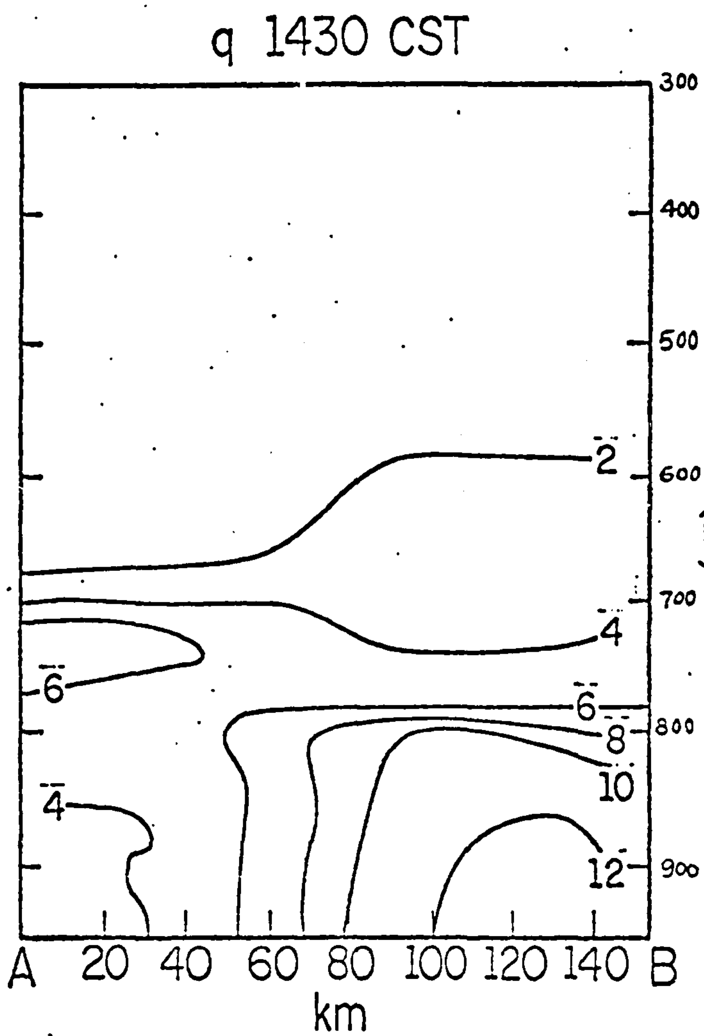

Fig. 4.24. Vertical cross-section for water vapor mixing ratio (g kg^{-1}) at 1430 LST (Ogura and Chen, 1977).

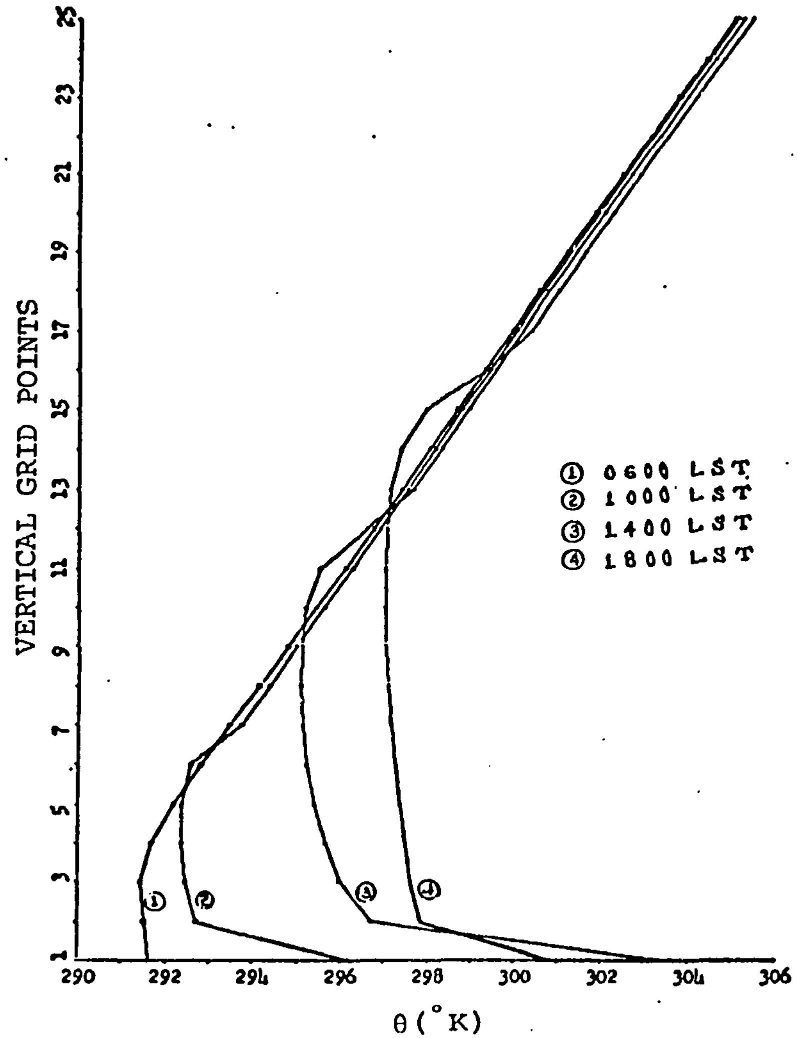

Fig. 4.25. Same as Fig. 4.20a except at grid point, i = 20.

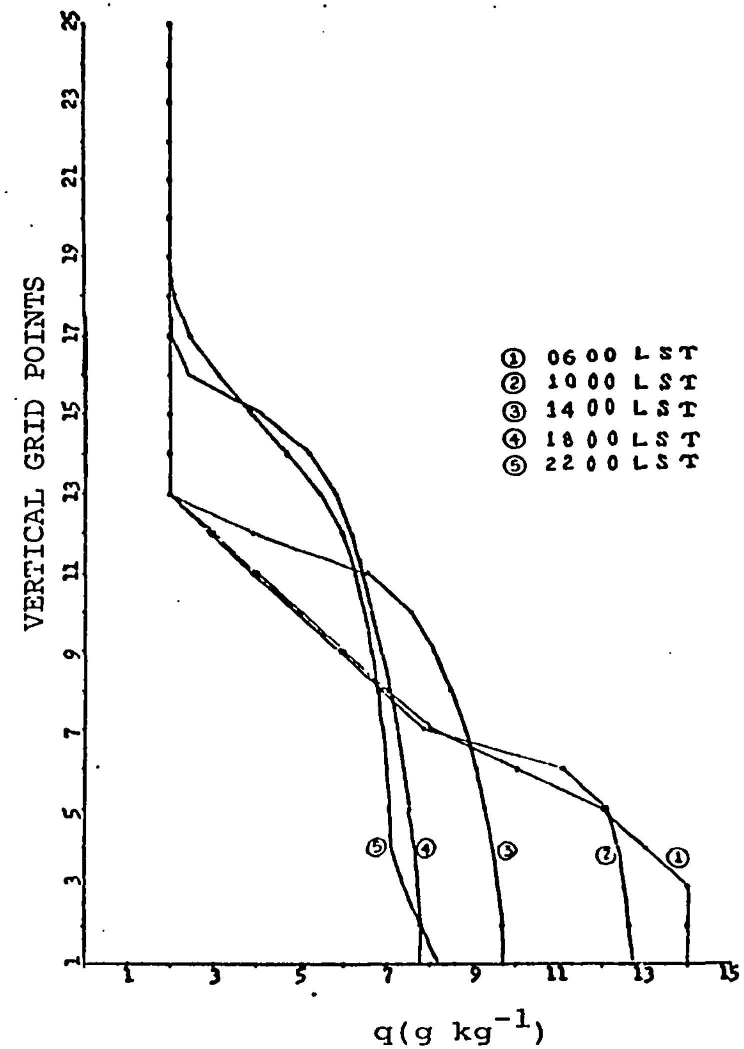

Fig. 4.26. Same as Fig. 4.25 except specific humidity.

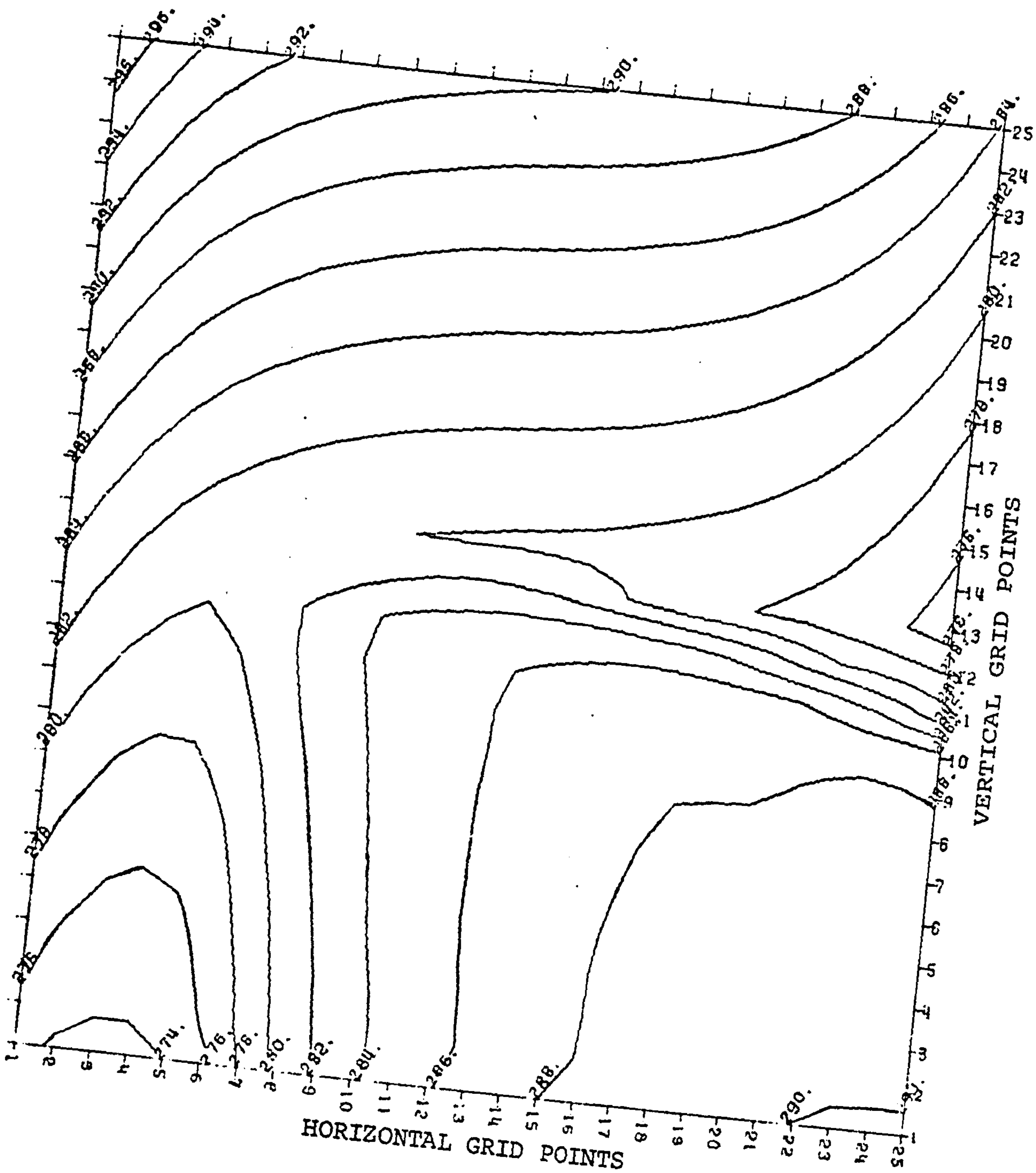

Fig. 4.27. Wet-bulb potential temperature (°K) at 1400 LST, Case A_2.

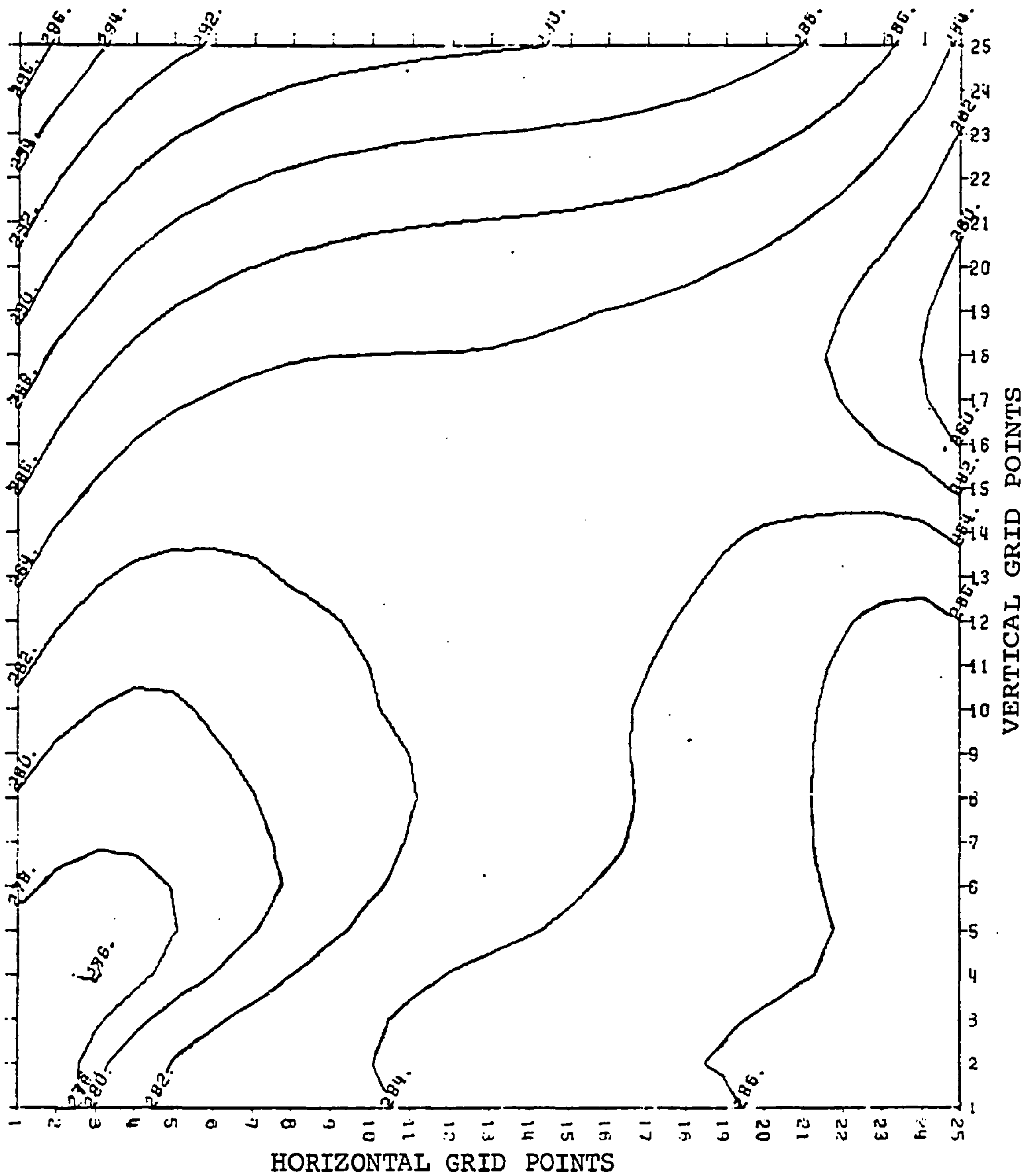

Fig. 4.28. Wet-bulb potential temperature (°K) at 0600 LST of the second day, Case A_2.

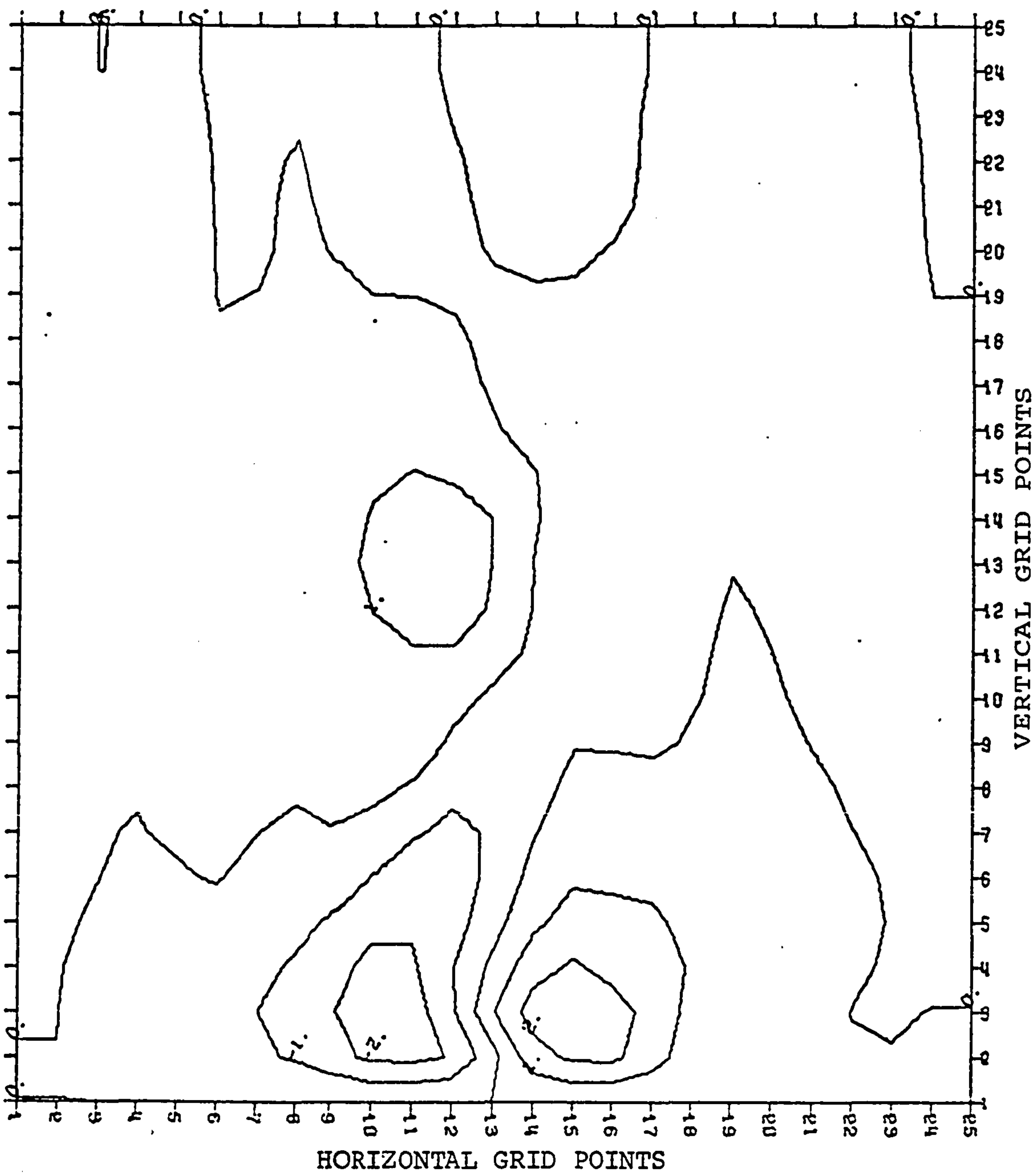

Fig. 4.29. Moisture divergence (10^{-4} g kg^{-1} sec^{-1}) at 2400 LST, Case A_1.

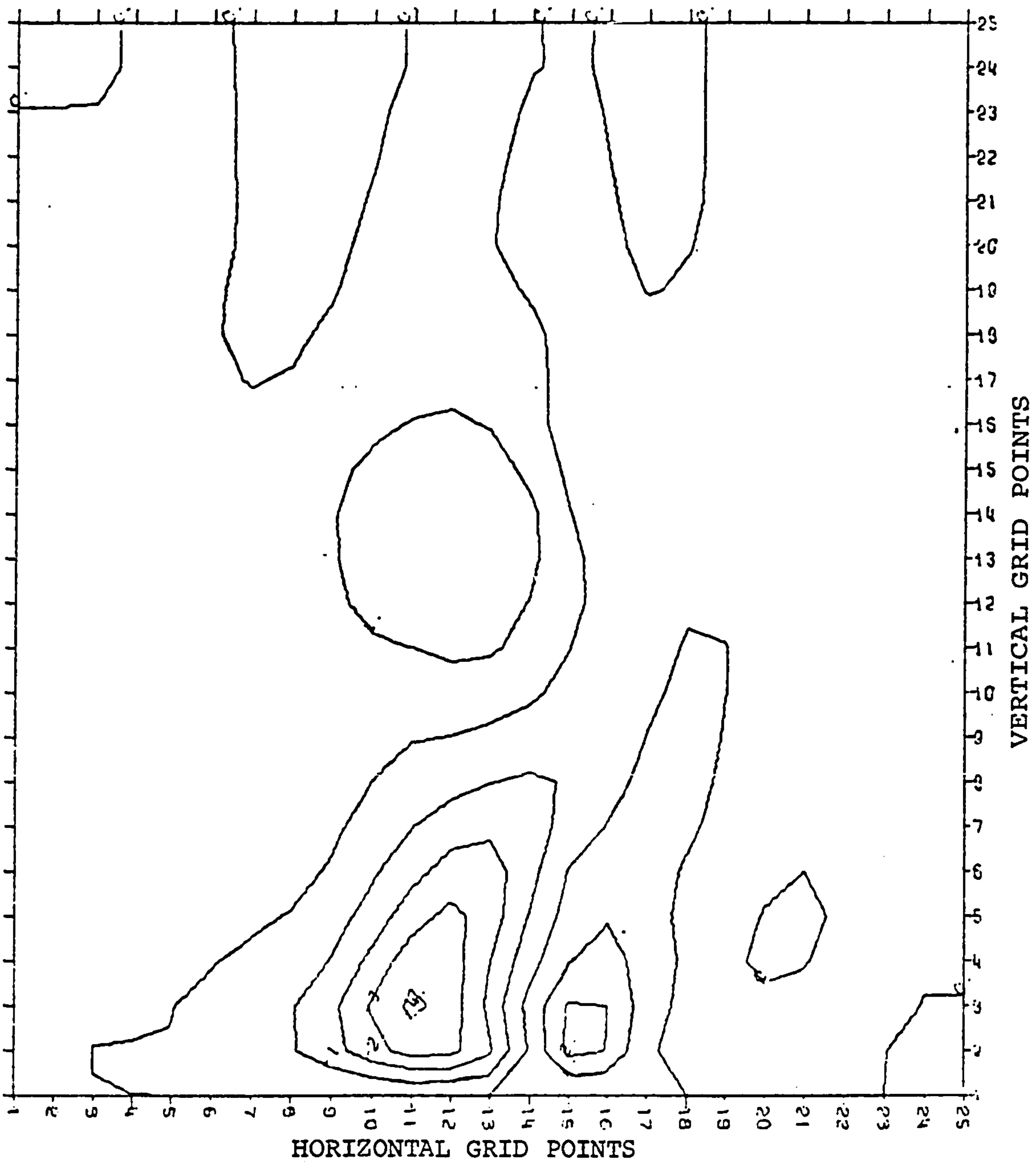

Fig. 4.30. Moisture divergence (10^{-4} g kg^{-1} sec^{-1}) at 2400 LST, Case I.

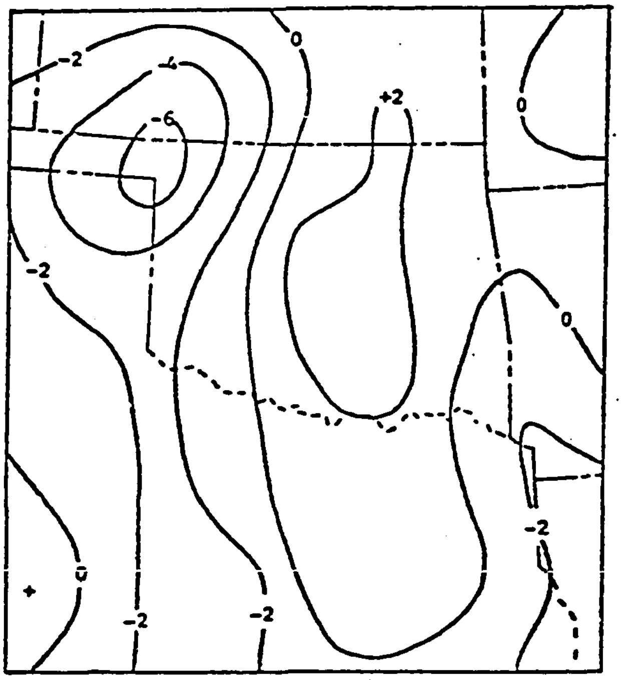

Fig. 4.31. Horizontal moisture divergence (10^{-4} g kg^{-1} sec^{-1}) for 2200 GMT 13 June 1972 (Hylton and Sasaki, 1973).

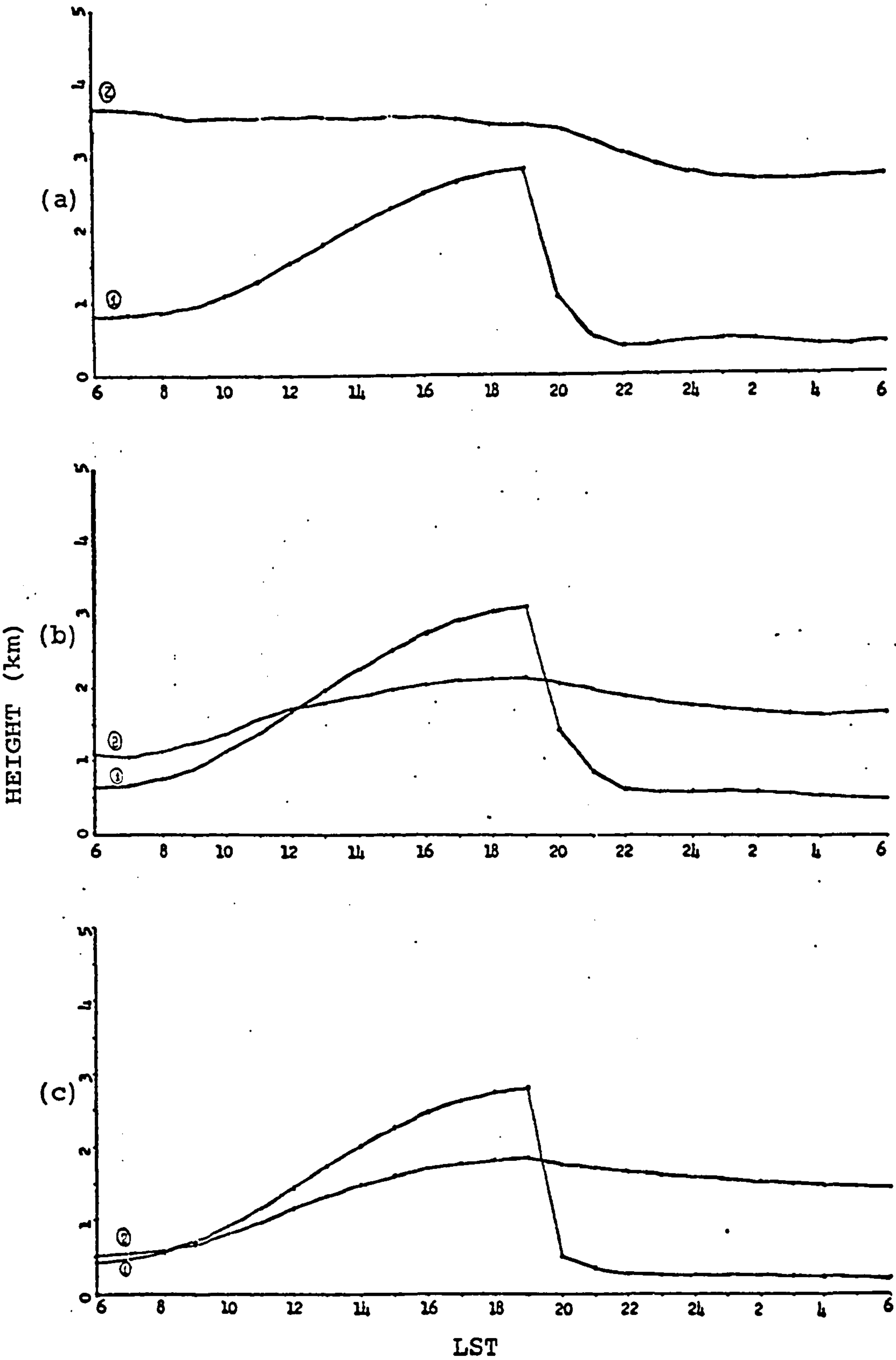

Fig. 4.32. Diurnal variation of (1) height of ABL, (2) height of LCL at grid point (a) i = 6, (b) i = 13, (c) i = 20.

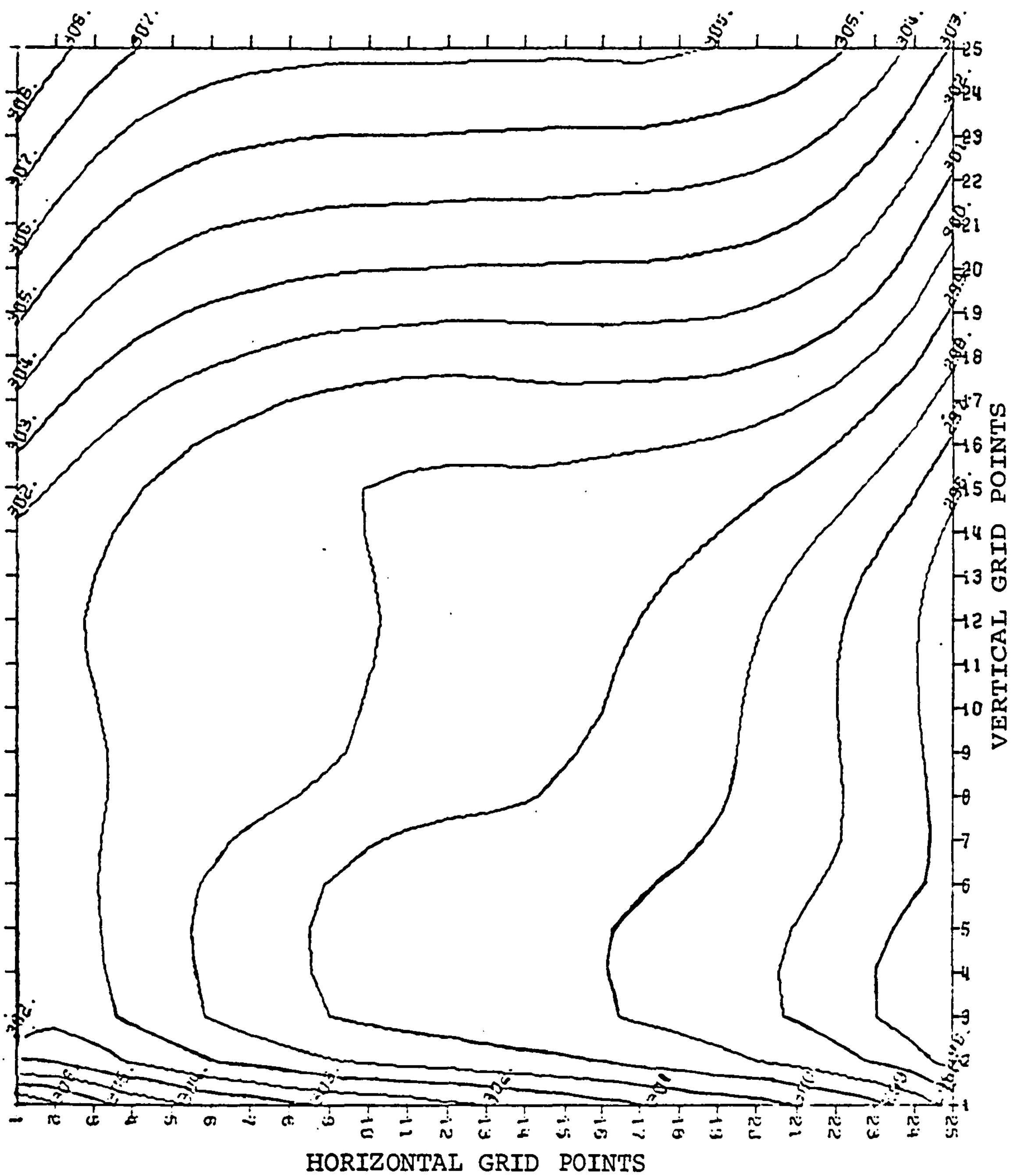

Fig. 4.33. Potential temperature (°K) at 1200 LST of the second-day simulation, Case A_1.

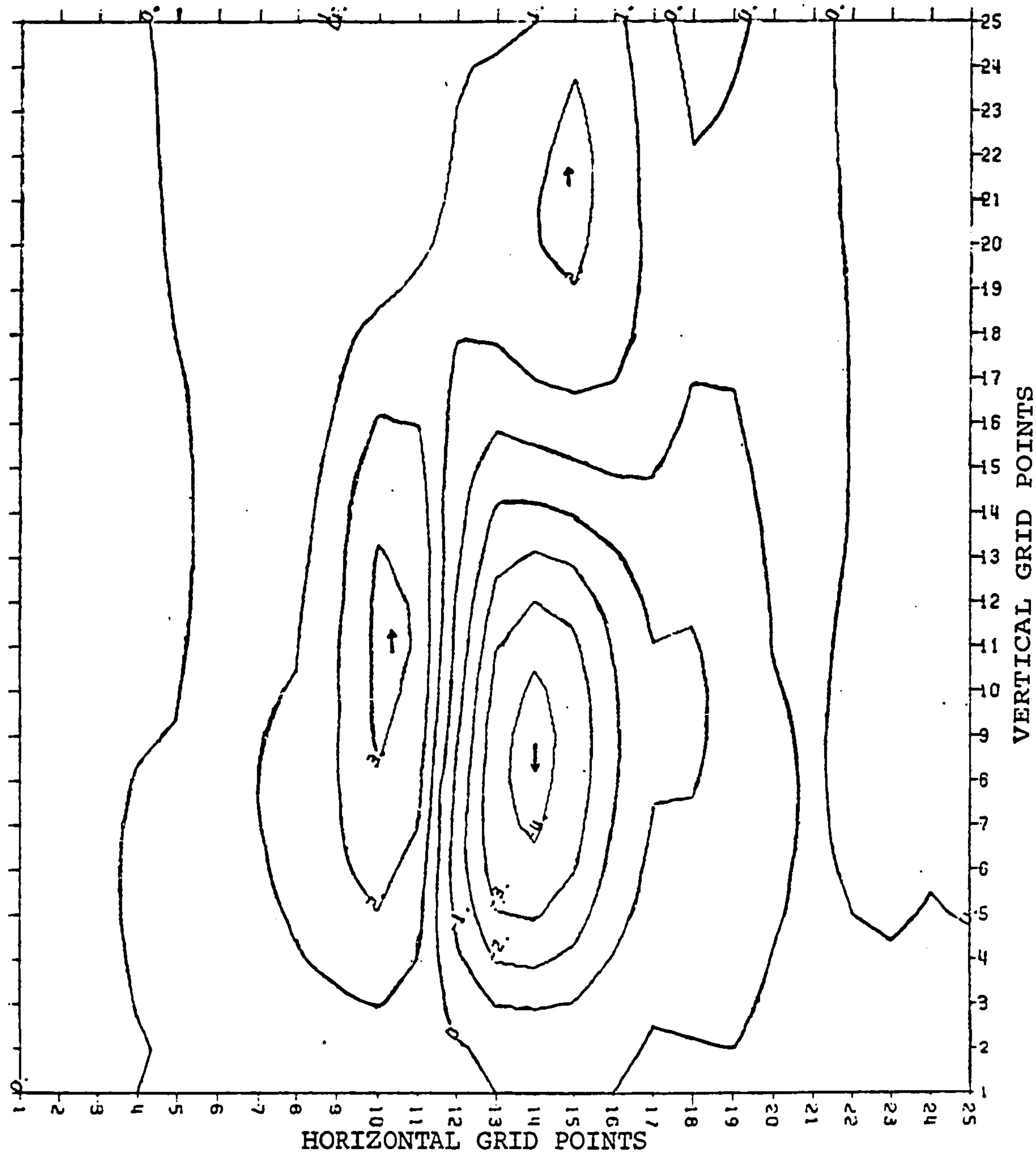

Fig. 4.34a. Vertical motion (cm sec^{-1}) at 2400 LST of the second day simulation, Case A_1.

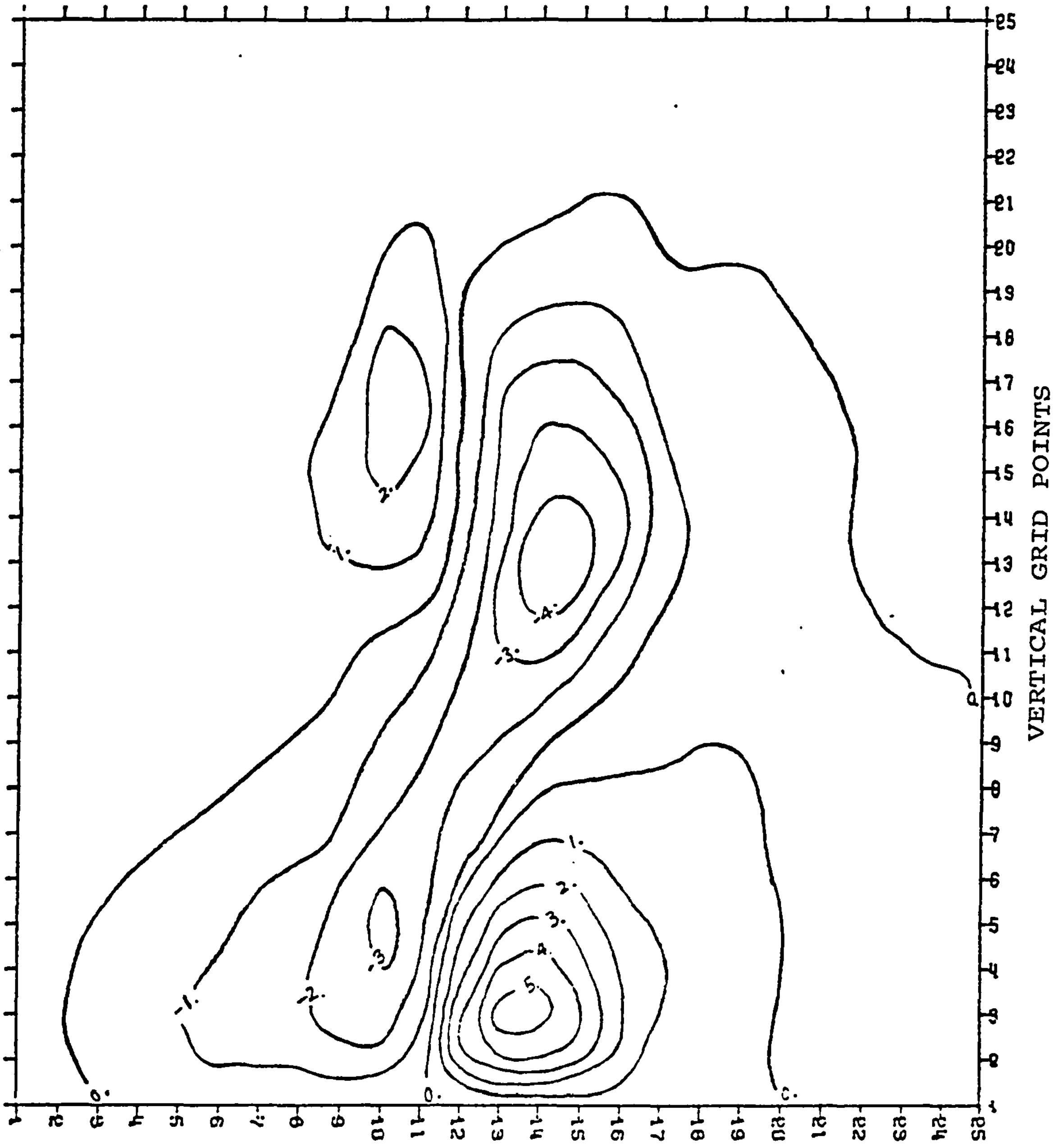

Fig. 4.34b. Divergence (10^{-5} sec^{-1}) at 2400 LST of the second-day simulation, Case A_1.

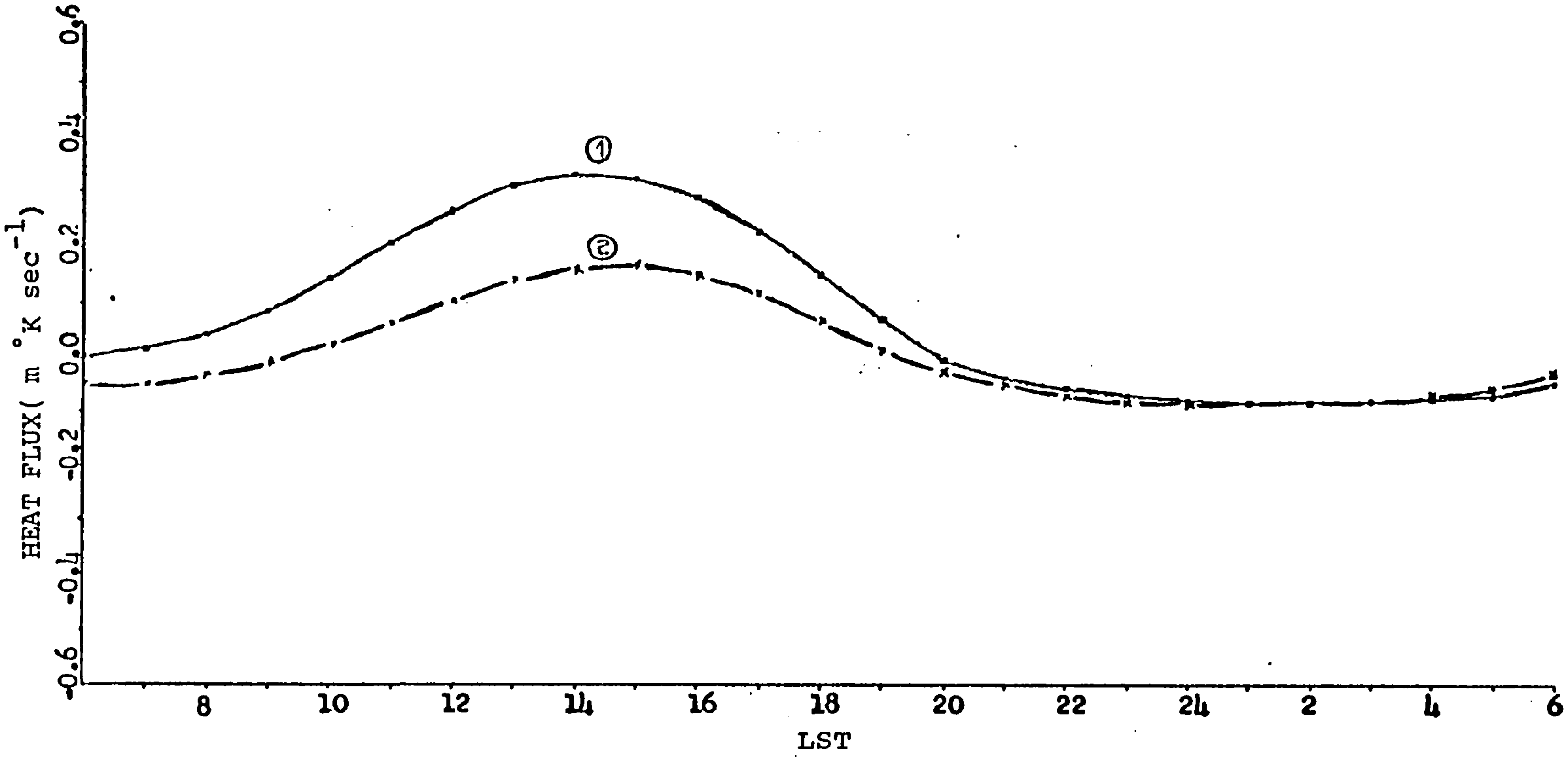

Fig. 4.35. Diurnal variation of surface heat flux at middle grid point; (1) first diurnal cycle, (2) second diurnal cycle, Case A_1.

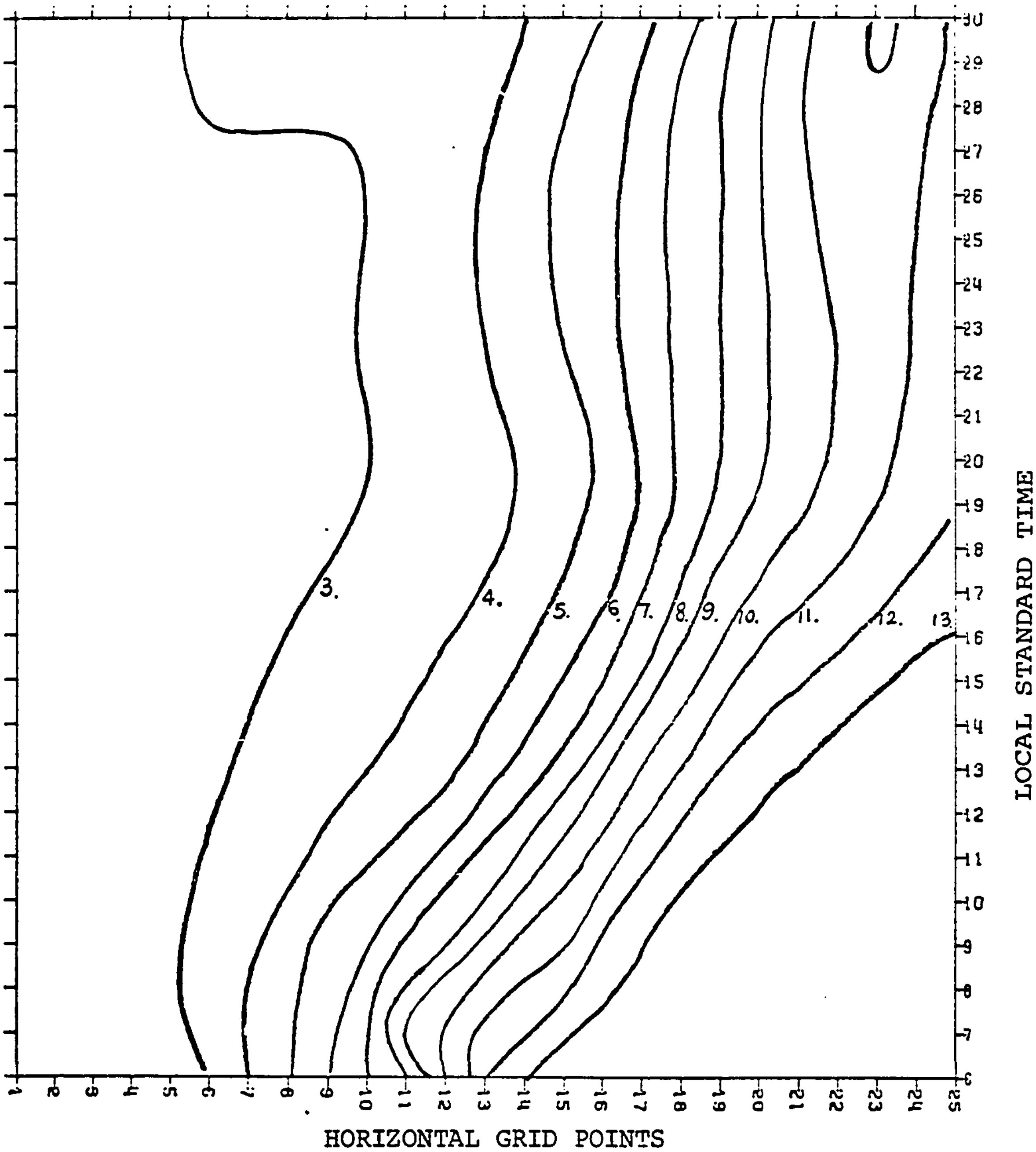

Fig. 4.36. Same as Fig. 3.1 except for Case J_1.

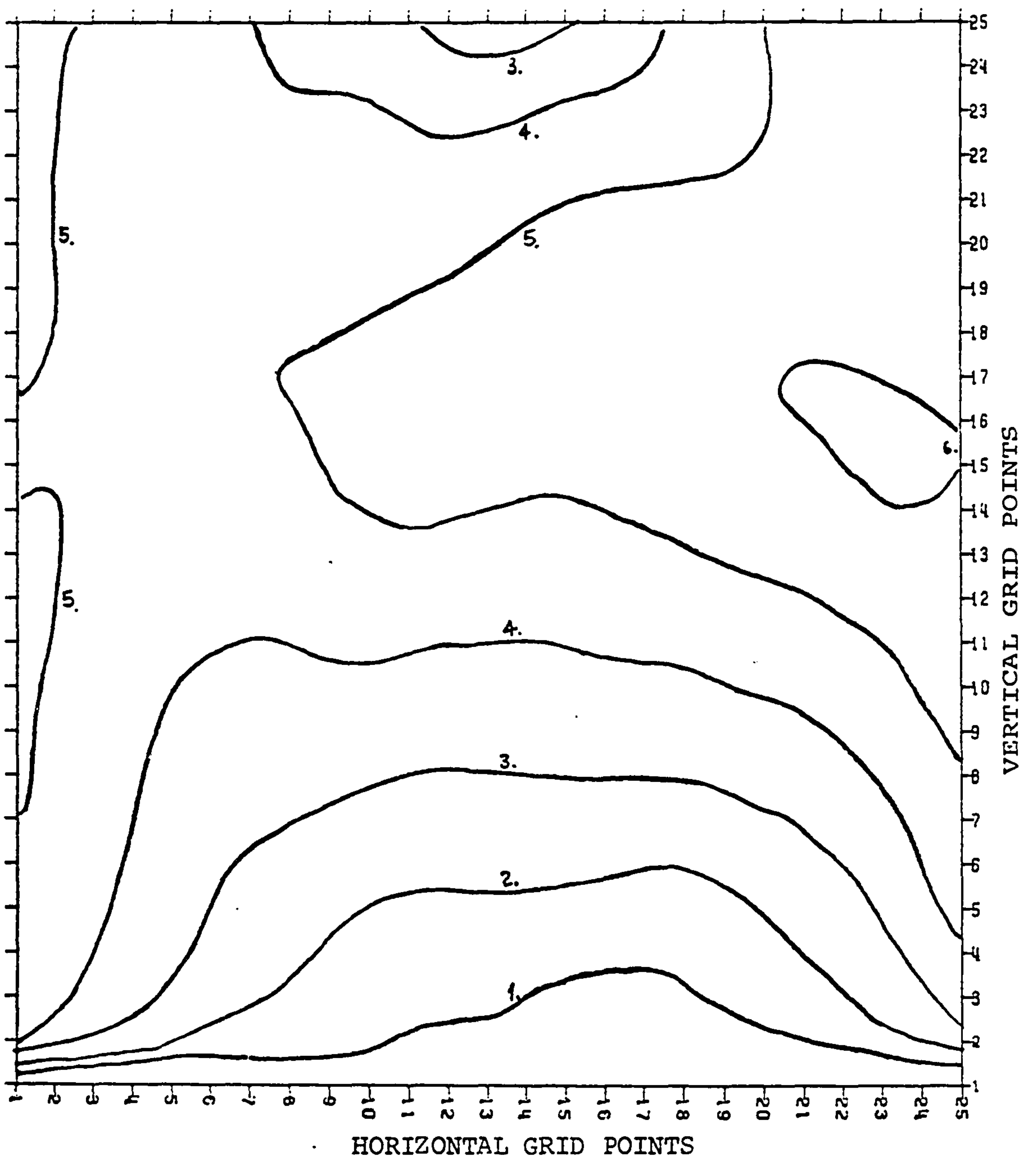

Fig. 4.37a. u-component wind at 1800 LST, Case J_1.

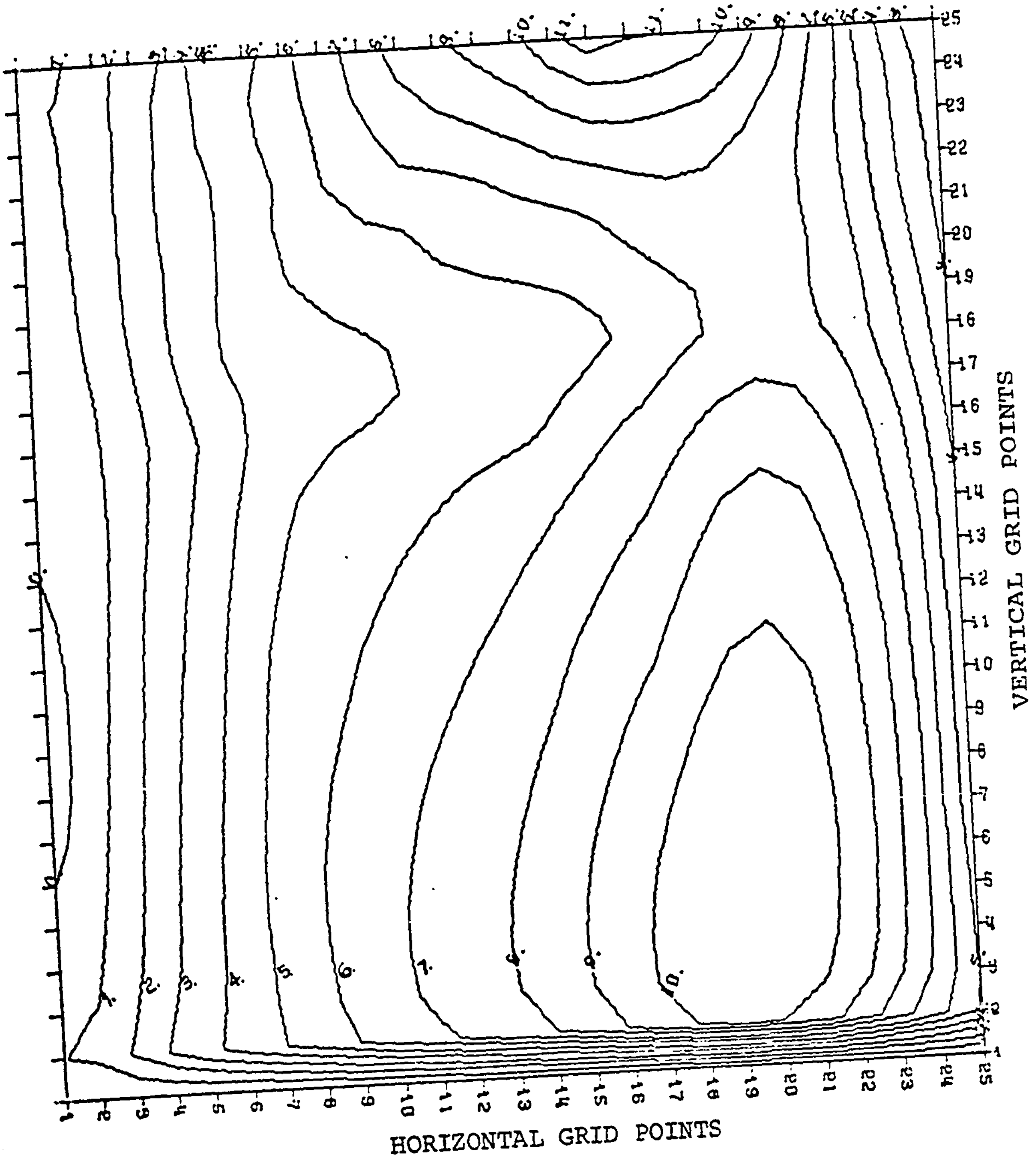

Fig. 4.37b. v-component wind at 1800 LST, Case J_1.

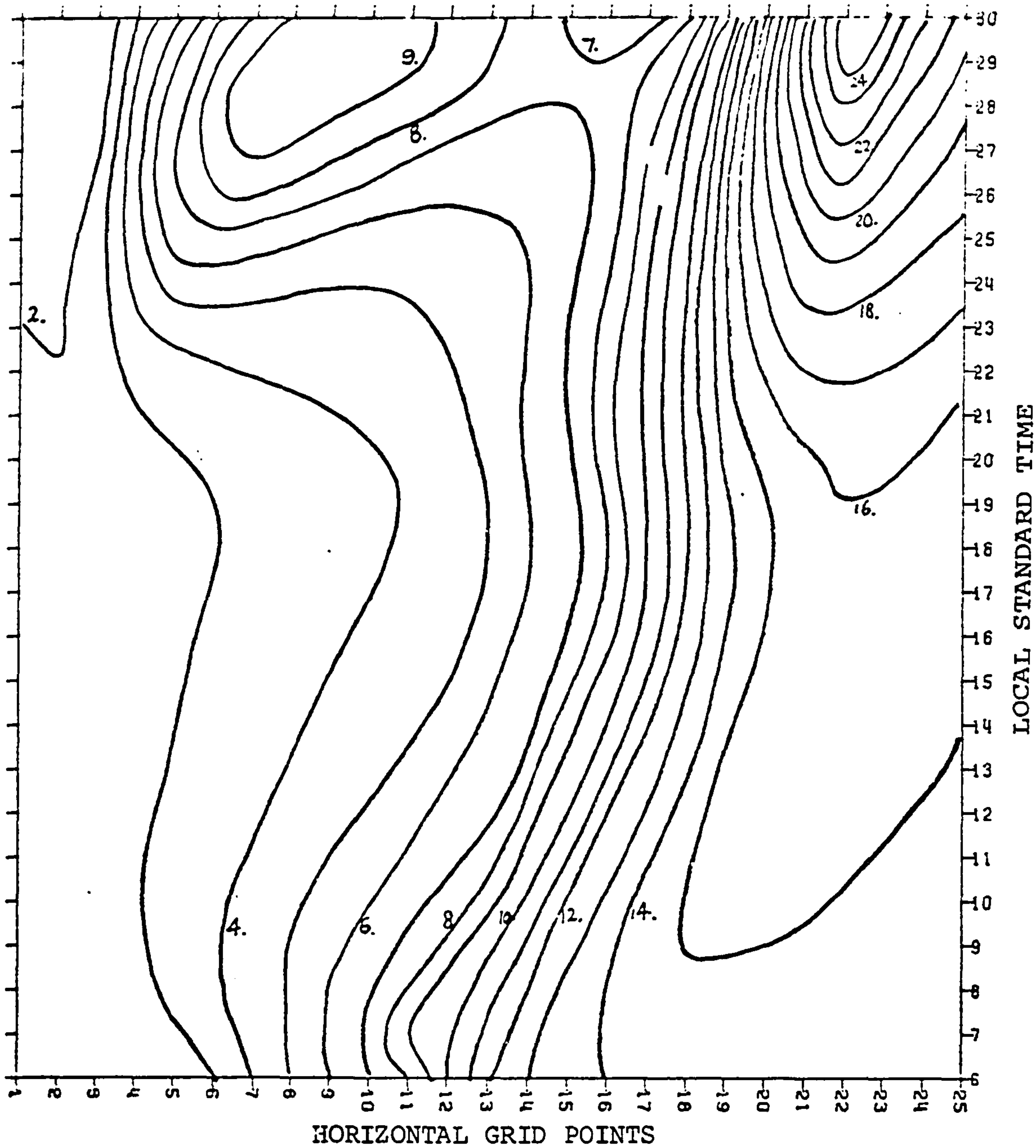

Fig. 4.38. Same as Fig. 3.1 except for Case J_2.

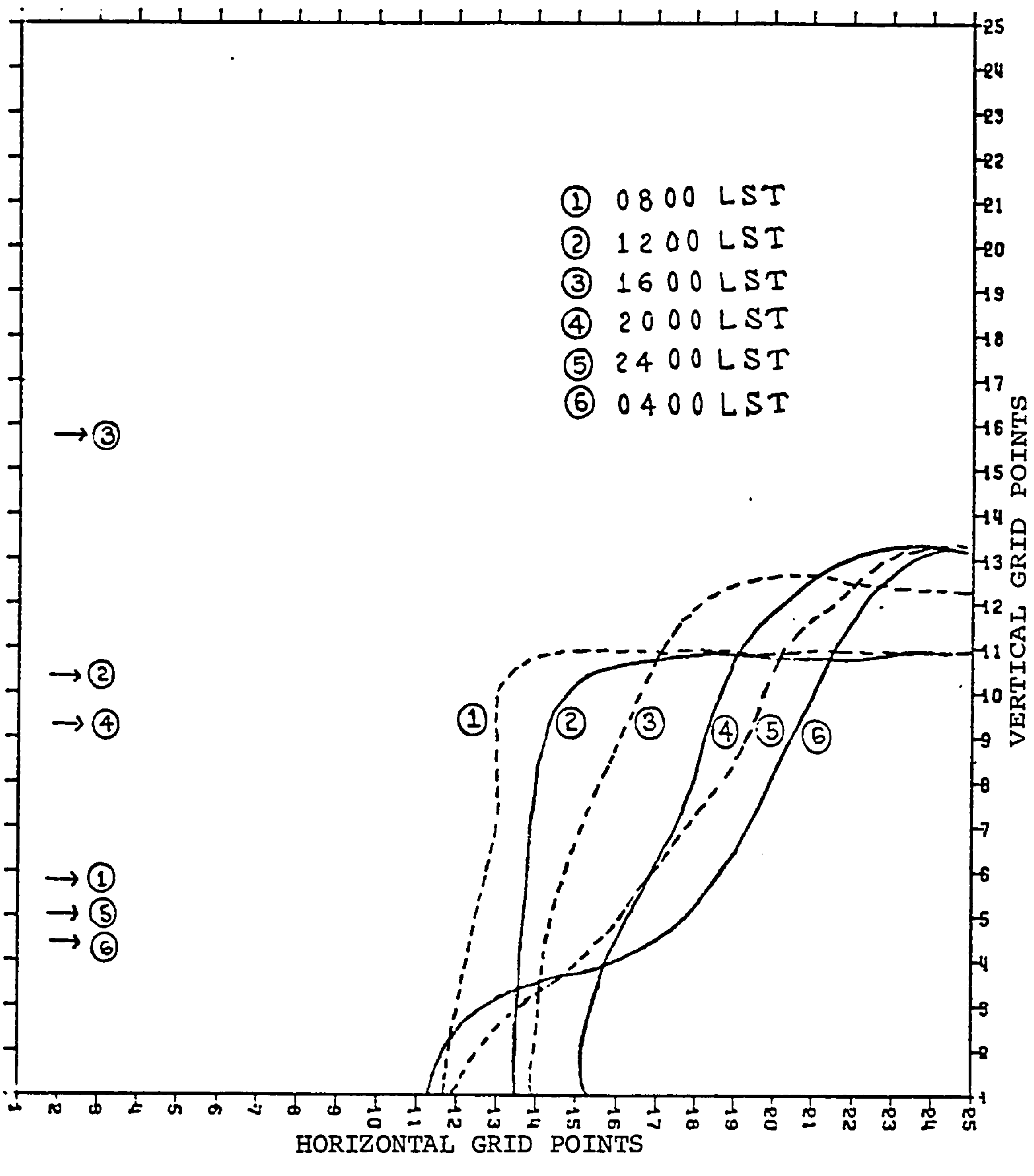

Fig. 5.1. The diurnal movement of the 10 g kg^{-1} isopleth for Case F. The corresponding heights of the inversion at the middle grid point are shown by arrows on the left of the figure.

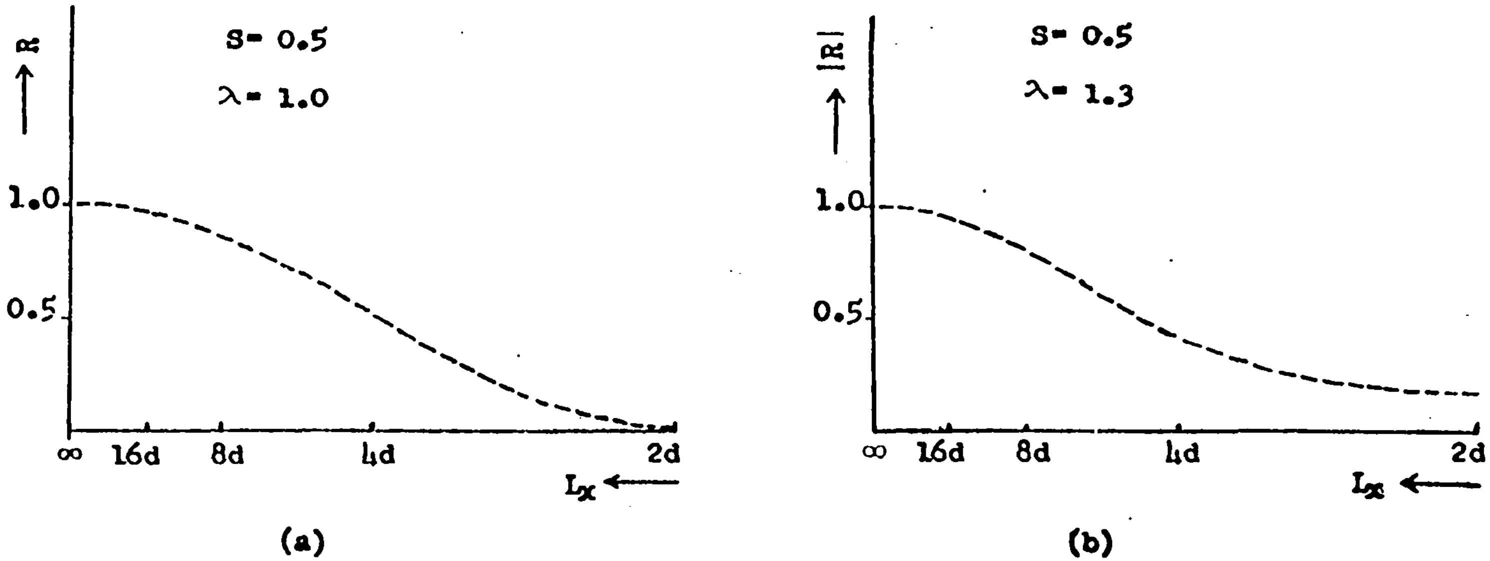

Fig. E.1. Local comparison of the response functions:
(a) for regular even-grid smoother (E.7) and
(b) for uneven operator (E.6). Also refer to the text.